Comparative Flight Performance Evaluation of the Flying-V and a Reference Aircraft

G. J. de Zoeten

TUDelft

Delft
University of
Technology
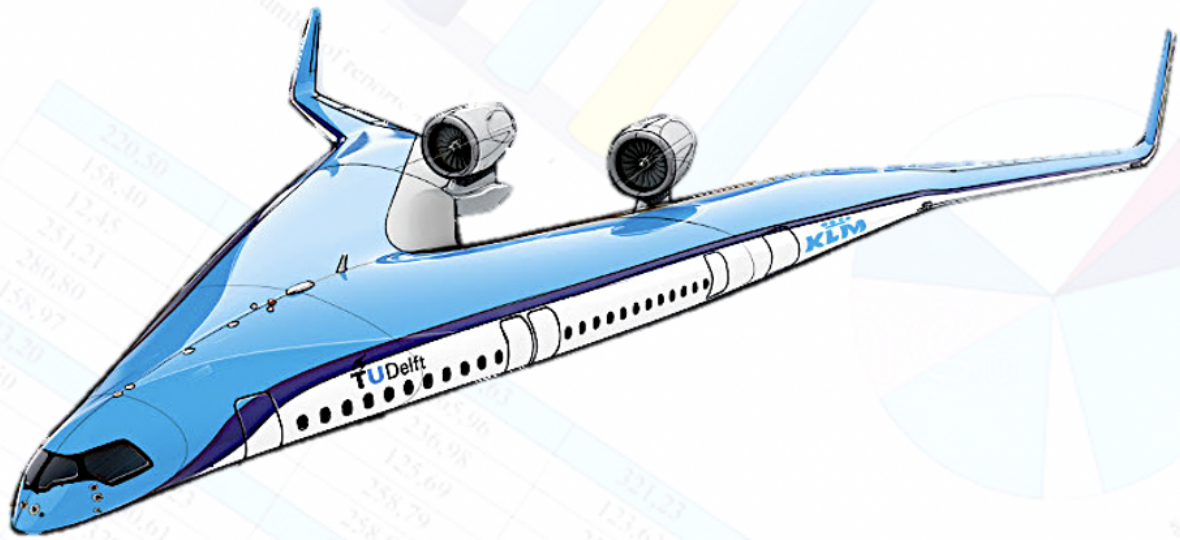
Comparative Flight Performance Evaluation of the Flying-V and a Reference Aircraft

by

G. J. de Zoeten

to obtain the degree of Master of Science
at the Delft University of Technology,
to be defended publicly on Thursday April 7, 2022 at 1:00 PM.

TUDelft
Delft
University of
Technology

PREFACE

Dear reader,

With great pleasure I present to you my MSc thesis, I hope you will enjoy reading it! With the completion of this thesis, my time as a student comes to and end. When I first set foot at the faculty of Applied Physics six and a half years ago, I did not think I would leave the university as a Master of Science in Aerospace Engineering (that is, if all goes well...). I remember being quite nervous about swapping the abstract concepts of quantum mechanics, solid state physics and relativity for a completely new discipline that I knew absolutely nothing about: aerospace engineering. This nervosity was not unwarranted, as I soon found out. My introduction to aerospace engineering was the first subject of the FPP track: Advanced Aircraft Design, taught by no other than my supervisor, Roelof Vos. Having no knowledge of aircraft or how they should be designed, I found myself struggling to keep up. Thankfully, I could nudge Yaïr whenever I did not know the meaning of a difficult or very simple technical term, such as the definition of the chord length. The fact that I made it to the end shows that I owe Yaïr a big thank you for getting me through the initial stages of this MSc. It also helped that there was someone else starting from zero with me: Costijn. Together we spent a great deal of time figuring out how we were going to get up to speed with the aerospace engineers. Although this was a struggle at first, it was also a very fulfilling experience thanks to the steep learning curve. I can honestly say I am glad that I made the switch to Aerospace Engineering, as I really enjoyed the diversity of the subjects of the FPP track and its exciting concepts.

The past year I have spent researching the topic of this thesis. When I was looking for a topic I did not know exactly what I wanted to do, but I did know that I wanted the Flying-V to be the subject. I want to thank Roelof for handing me this assignment and supervising my research. The biweekly discussions that we had were both serious and fun. A big thank you goes to my co-supervisor, Carmine. We started out as a PhD candidate and a MSc thesis student, and look at us now... Once again congratulations on your brand-new title, doctor. From what I have seen I would say you fully deserved it.

As anyone at the end of their MSc would say, it has not always been smooth sailing. I want to thank my parents, family and friends for their unwavering support, especially when times were tougher.

Looking back at my time as a student, I feel grateful. Now, it's time to move on to the next chapter!

G.J. de Zoeten
Rotterdam, April 2022

SUMMARY

The Flying-V is a novel aircraft configuration that has shown a promising fuel saving potential compared to a conventional aircraft. The V-shaped configuration of the Flying-V integrates the passenger cabin and cargo volume into the lifting surface and has fins to provide lateral and directional stability. Several studies have been conducted into various aspects of the Flying-V, including the aerodynamics, structure and handling qualities.

The objective of this research is to evaluate the flight performance characteristics of a Flying-V aircraft and compare results to a reference aircraft, by simulating takeoff, landing, climb and cruise using a flight mechanics model. More specifically, the performance characteristics of the Flying-V-1000 (FVK) and Airbus A350-1000 (A35K) are evaluated and compared. The subject of flight performance answers practical questions about what an aircraft is capable of. Using an in-house developed flight mechanics toolbox, various sub-models are integrated to create a flight mechanics model. The aerodynamic model is based on data from a vortex-lattice method developed by Airbus, enhanced with empirical zero-lift drag and wave drag models. Other sub-models that have been integrated include an inertia model, a propulsion model, a pilot model and a landing gear model.

On average, the FVK features a 25% shorter takeoff distance than the A35K. This difference is mainly due to the significantly smaller minimum unstick speed of the FVK, which is a consequence of the FVK's larger tailstrike attitude. For both aircraft, geometric tailstrike constraints determine the minimum unstick speed, rather than the elevator effectiveness. The shorter takeoff distance of the FVK also leads to an averaged 30% shorter Balanced Field Length (BFL). The relative difference between the BFL of both aircraft is larger than for the takeoff distance, because the FVK is able to brake more effectively than the A35K.

The landing distances and approach speeds of both aircraft are similar, although the total landing distance is distributed differently over the phases of the landing manoeuvre. Due to a combination of a higher touchdown attitude and smaller ground attitude, the derotation distance of the FVK is significantly larger than for the A35K, assuming equal derotation rates for both aircraft. The FVK is able to compensate its longer derotation distance with a shorter braking distance to achieve a similar total landing distance as the A35K. An analysis of the pilot's vision during the landing flare manoeuvre has shown that the FVK's obscured segment can be twice as large as for the A35K. For landings performed with poor visibility, this could be problematic for the FVK.

Due to its larger maximum L/D, the FVK has better climb performance characteristics than the A35K. With One Engine Inoperative, the FVK is able to meet the climb gradient requirements of CS25.125 for altitudes up to 8000 ft at Maximum Takeoff Mass. The absolute service ceilings of the FVK and A35K were found to be 13.4 km and 12.0 km, respectively.

Evaluation of the Specific Air Range (SAR) parameter shows that the FVK outperforms the A35K in terms of cruise efficiency. The maximum trimmed aerodynamic efficiency, transonic efficiency and Range Parameter (RP) were found to be respectively 17%, 21% and 21% higher for the FVK. The Mach numbers and lift coefficients where the RP maxima are located suggest an optimal cruise altitude of 12.0 km for the FVK and 11.3 km for the A35K.

CONTENTS

LIST OF FIGURES

LIST OF TABLES

NOMENCLATURE

Latin Symbols

a	Acceleration	(m/s^2)
A	Area	(m^2)
AR	Wing aspect ratio	(-)
b	Aircraft span	(m)
BPR	Engine bypass ratio	(-)
C_D	Drag coefficient	(-)
C_{D_0}	Zero-lift drag coefficient	(-)
$C_{D_{inv}}$	Inviscid drag coefficient	(-)
C_{D_w}	Wave drag coefficient	(-)
$C_{D_{wme}}$	Windmilling engine drag coefficient	(-)
C_f	Flat-plate skin friction coefficient	(-)
C_L	Lift coefficient	(-)
C_m	Pitching moment coefficient	(-)
C_n	Yawing moment coefficient	(-)
C_T	Thrust coefficient	(-)
C_X	X-force coefficient	(-)
C_Z	Z-force coefficient	(-)
d	Distance perpendicular to rotation axis	(m)
e	Error in prescribed value	
D	Drag	(N)
D_f	Fan diameter	(m)
D_i	Induced drag	(N)
D_{inlet}	Engine inlet diameter	(m)
e	Oswald factor	(-)
f	From factor	(-)
g	Gravitational acceleration	(m/s^2)
G	Gas generator function	(-)
G_0	Gas generator function at sea level	(-)
h	Altitude	(m)
h_s	Screen height	(m)
I	Moment of inertia	(kg m^2)
K_d	Derivative control gain	(-)
K_i	Integral control gain	(-)
K_P	Proportional control gain	(-)
L	Lift	(N)
$\mathscr{L}$	Rolling moment	(Nm)
$\mathscr{M}$	Pitching moment	(Nm)
M	Mach number	(-)
M_{crit}	Critical Mach number	(-)
M_{dd}	Drag divergence Mach number	(-)
M_{dd2d}	Two-dimensional drag divergence Mach number	(-)
M_{dd3d}	Three-dimensional drag divergence Mach number	(-)
M_{ref}	Reference (cruise) Mach number	(-)
m	Mass	(kg)
$\mathscr{N}$	Yawing moment	(Nm)
N	Normal force	(N)
N_{ng}	Normal force on nose gear	(N)
N_{mg}	Normal force on main gear	(N)

p	Roll rate	(rad/s)
P_{av}	Available power	(W)
P_{req}	Required power	(W)
q	Pitch rate	(rad/s)
r	Yaw rate	(rad/s)
RoC	Rate of Climb	(m/s)
Re_L	Reynolds number based on reference length L	(-)
s	Distance	(m)
S	Wing reference area	(m^2)
S_{wet}	Wetted area	(m^2)
t	Wing thickness	(m)
t	Time	(s)
T	Thrust	(N)
T_{SSL}	Static Sea Level thrust	(N)
u	Velocity in x-direction in body reference frame	(m/s)
v	Velocity in y-direction in body reference frame	(m/s)
V	Velocity	(m/s)
V_1	Decision speed	(m/s)
V_2	Takeoff safety speed	(m/s)
V_{App}	Approach speed	(m/s)
V_{cas}	Calibrated airspeed during climb	(m/s)
V_{EF}	Assumed Engine failure velocity	(m/s)
V_j	Jet velocity	(m/s)
V_{MU}	Minimum un-stick speed	(m/s)
V_R	Rotation speed	(m/s)
V_S	Stalling speed	(m/s)
V_{SR}	Reference stall speed	(m/s)
V_{SR0}	Stall speed in landing configuration	(m/s)
V_∞	Free-stream velocity	(m/s)
w	Velocity in z-direction in body reference frame	(m/s)
W	Weight	(N)
x_{cg}	X-coordinate of the center of gravity	(m)
X	Longitudinal force	(N)
Y	Side force	(N)
Z	Normal force	(N)

Greek Symbols

α	Angle of attack	(deg)
γ	Flight path angle	(deg)
δ_{cs}	Control surface deflection	(deg)
δ_{pitch}	Pitch control variable	(-)
δ_{roll}	Roll control variable	(-)
$\delta_{throttle}$	Throttle setting	(-)
δ_{yaw}	Yaw control variable	(-)
θ	Pitch attitude	(deg)
θ_{ground}	Ground resting pitch attitude	(deg)
θ_{TS}	Wing tip/tail strike pitch attitude	(deg)
η	Powerplant efficiency	(-)
Λ	Wing sweep angle	(deg)
ρ	Density	(kg/m^3)
μ_b	Coefficient of braking friction	(-)
μ_r	Coefficient of rolling friction	(-)
Π	Ambient pressure ratio	(-)
ϕ	Roll angle	(deg)
Ψ	Yaw angle	(deg)

Abbreviations

A35K	Airbus A350-1000
AoA	Angle of Attack
AoC	Angle of Climb
AR	Aspect Ratio
BPR	Bypass Ratio
BWB	Blended Wing Body
CFD	Computational Fluid Dynamics
CG	Centre of Gravity
CS	Control Surface
DND	Droop Nose Device
DoF	Degrees of Freedom
EASA	European Union Aviation Safety Agency
EGC	Excluding Ground Contact
EOM	Equations of Motion
FAA	Federal Aviation Administration
FBD	Free Body Diagram
FEM	Finite Element Method
FPR	Fan Pressure Ratio
FV	Flying-V
FVK	Flying-V-1000
FW	Flying Wing
IGE	In Ground Effect
ISA	International Standard Atmosphere
LG	Landing Gear
MAC	Mean Aerodynamic Chord
MGC	Mean Geometric Chord
MG	Main Gear
MLM	Maximum Landing Mass
MLW	Maximum Landing Weight
MOI	Moment of Inertia
MTOM	Maximum Take Off Mass
MTOW	Maximum Take Off Weight
NASA	National Aeronautics and Space Administration
NG	Nose Gear
OEI	One Engine Inoperative
OEM	Operational Empty Mass
OEW	Operational Empty Weight
OGE	Out of Ground Effect
OML	Outer Mold Line
OPR	Overall Pressure Ratio
RANS	Reynolds Averaged Navier Stokes
RoC	Rate of Climb
SFC	Specific Fuel Consumption
SM	Static Margin
SSL	Static Sea Level
TIT	Turbine Inlet Temperature
TSFC	Thrust Specific Fuel Consumption
VLM	Vortex Lattice Method
WT	Wind Tunnel
ZFW	Zero Fuel Weight

Subscripts

av	Available
CS	Control Surface
cg	Centre of Gravity
derot	Derotation
EF	Engine Failure
EGC	Excluding Ground Contact
GC	Ground Contact
inv	Inviscid
ng	nose gear
mg	main gear
MU	Minimum Unstick
ref	Reference
req	Required
SSL	Static Sea Level
TD	Touchdown
TS	Tailstrike
wme	Windmilling Engine

1

INTRODUCTION

Ever since Boeing engineers introduced the B47 bomber in 1947 with its slender fuselage, high aspect ratio swept-back wings, rear empennage and engines podded under the wing, similar aircraft configurations have frequently been used by engineers designing civil transport aircraft. Improvements in structural weight, aerodynamic efficiency and engine fuel efficiency have led to an overall efficiency improvement of 100 percent [1] with respect to the B47. However, the rate of progress has slowed over the course of time and the conventional aircraft configuration is approaching an asymptote in terms of overall efficiency [2]. With the demand for air travel doubling approximately every 15 years [3] and increasing constraints in terms of noise and pollution, engineers have started looking at unconventional aircraft configurations that are possibly more fuel efficient than the conventional configuration.

Unconventional tailless aircraft configurations have shown great promise in terms of aerodynamic efficiency [4]. Due to the integrated wing and fuselage, the friction drag is reduced due to a smaller wetted area [2]. Other benefits of the concept include a reduced interference drag and a beneficial spanwise lift distribution [5]. Flying wing aircraft could have a 15-20% larger range than a conventional tube-and-wing aircraft [6]. The first research into tailless aircraft dates back to the 1930s, when Lippisch and Horten researched the concept, and the 1940s, when Northrop started developing the YB-49 [7]. Although the concept has been researched for a long time, the aviation industry has been reluctant to develop an actual flying wing passenger aircraft. Reasons for this reluctance include large development costs due to limited available knowledge, passenger acceptance and stability and control issues [8]. Researcher efforts have mainly been focused on two types of tailless aircraft: flying wings (FW) [4, 7, 9–11], which feature straight leading and trailing edges (see Figure 1.1a), and Blended Wing Body (BWB) [5, 12–16] aircraft (see Figure 1.1b), which feature a wing that is smoothly blended with the centre-body.

(a) Northrop YB-49, a FW aircraft.
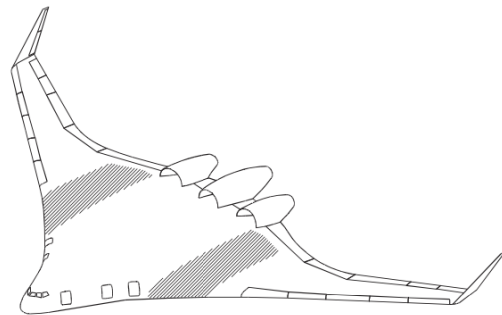
(b) Blended Wing Body (BWB) aircraft.

Figure 1.1: Examples of two types of tailless aircraft configurations: the Flying Wing (FW) and Blended Wing Body (BWB) [7].

1
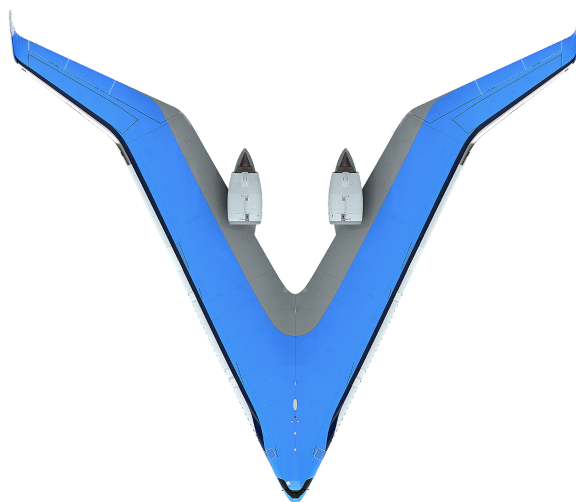
Figure 1.2: Top view of the Flying-V[1].

In 2015, Benad [17] conceived a new FW concept at the Technische Universität Berlin in collaboration with Airbus GmbH. This new concept was called the Flying-V, due to its planform shape, shown in Figure 1.2. The Flying-V features elevons at the trailing edge for longitudinal and lateral control and twin fins with rudders mounted at the wing tips for directional stability and control. The engines are positioned on top of the wing, which results in a noise reduction. Contrary to the usual configuration of the pressurised cabin in BWB and FW aircraft, the Flying-V features two cylindrical cabins allowing the wing volume to be used efficiently without a large structural weight penalty. Results obtained by Benad show an aerodynamic efficiency improvement of 10% and a 2% lower operational empty weight with respect to the Airbus A350-900, the reference tube-and-wing aircraft [17] for the initial Flying-V design. Since the concept was first envisioned by Benad, various researches have been conducted at the TU Delft to improve its design. A parametric model of the Flying-V was conceived, and the planform and wing profile sections were optimised for aerodynamic efficiency in cruise [2, 18]. A structural concept was developed [19], the effect of engine integration was investigated [20–23] and the influence of the ground effect was studied [24]. Also, various wind tunnel studies using a sub-scale model were conducted [25–32], an improved parametrisation for the Outer Mold Line was developed [33] and studies into the design of the landing gear [34] and cockpit [35] were performed. A detailed study into the structural concept of the Flying-V [36] and a study into the handling qualities [37] were performed in collaboration with Airbus.

Previous research efforts have mainly been focused on improving the existing Flying-V concept. However, the flight performance characteristics of the Flying-V have not been evaluated yet. The subject of flight performance answers practical questions about what an aircraft is capable of. Ultimately, flight performance characteristics tell the designer whether their design has been successful or not [38]. Therefore it is relevant to evaluate the performance characteristics of the Flying-V in its current state and compare them to a reference state-of-the art aircraft in order to learn about its strengths and areas that require improvement.

---

[1]Render by E. Wallet. https://www.tudelft.nl/lr/flying-v (Accessed March 12, 2022)

1.1. RESEARCH OBJECTIVE AND QUESTIONS

This research aims to study the flight performance characteristics of a Flying-V aircraft and compare the results with a reference aircraft. The main research objective is

> **to evaluate the flight performance characteristics of a Flying-V aircraft and compare results to a reference aircraft, by simulating takeoff, landing, climb and cruise using a flight mechanics model.**

Research question:

> **What are the flight performance characteristics of a Flying-V aircraft during the takeoff, landing, climb and cruise flight phases compared to a conventional aircraft?**

The main research question can be divided into several sub-questions for the different flight phases that are evaluated.

For the takeoff phase:

- How do the horizontal distances travelled by a Flying-V aircraft during the pre-rotation, rotation and airborne phase of the takeoff manoeuvre compare to a reference aircraft?

- How does the minimum unstick speed and optimal rotation speed of a Flying-V aircraft compare to a reference aircraft?

- How does the balanced field length of a Flying-V aircraft compare to a reference aircraft?

For the landing phase:

- How do the horizontal distances travelled by a Flying-V aircraft during the airborne, derotation and braking phase of the landing manoeuvre compare to a reference aircraft?

- How does pilot vision during the landing flare of a Flying-V aircraft compare to a reference aircraft?

For climbing flight:

- How does the service ceiling of a Flying-V aircraft compare to a reference aircraft?

- How do the fastest and steepest climb trajectories of a Flying-V aircraft compare to a reference aircraft?

- How does the One Engine Inoperative climb performance of a Flying-V aircraft compare to a reference aircraft?

For cruise flight:

- How does the specific air range of a Flying-V aircraft compare to a reference aircraft?

1.2. OUTLINE

In the remainder of this thesis, the research questions formulated above will be answered. In chapter 2, background information is presented, including a comparison of top-level aircraft specifications and flight performance definitions. In chapter 3 the methodology is presented. chapter 4 presents the verification and validation of the conceived flight mechanics model. Simulation results are presented and discussed in chapter 5. In chapter 6 conclusions are drawn and recommendations for future work are presented.

2

BACKGROUND

This chapter provides relevant background information for the research at hand. Specifications of the Flying-V and the reference aircraft are presented and notable differences are highlighted, followed by a brief introduction to the different aspects of the flight performance evaluation performed in this research.

2.1. FLYING-V AND REFERENCE AIRCRAFT SPECIFICATIONS
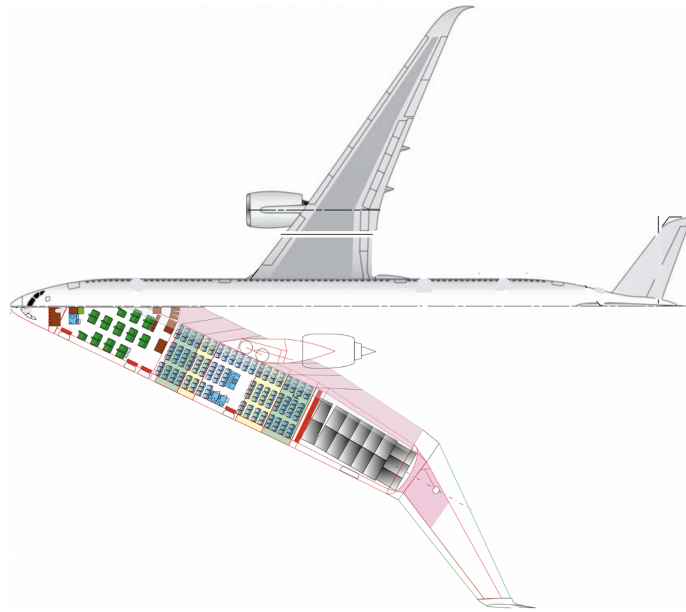
Figure 2.1: Planform comparison of the Flying-V-1000 and Airbus A350-1000. Figure adapted from Oosterom [39] and Airbus [40].

The present research compares the flight performance characteristics of the Flying-V-1000 to the Airbus A350-1000. The Flying-V-1000 is the largest aircraft of the Flying-V family designed by Oosterom [39], which has similar mission requirements as the Airbus A350-1000. For the remainder of this thesis, the Flying-V-1000 and Airbus A350-1000 will be referred to as the FVK and A35K, respectively. Due to the availability of data and the wide range of conducted research studies which all have their own scope, the aircraft specifications and data used in this research originate from different sources, tabulated in Table 2.1. The aerodynamic characteristics of both aircraft are obtained from datasets generated using Odilila [37], which is discussed in section 3.2. The range of centre of gravity (CG) positions is also determined from the aforementioned aerodynamic characteristics. The inertia tensors are adapted from the research conducted by Claeys [36] as presented in section 3.3. The planform geometries of both aircraft are compared in Figure 2.1 and are retrieved from the Flying-V family design [39] and Airbus [40]. The airfoil geometry at different wing sections of the FVK is based on the sub-scale wind tunnel

model used for various campaigns [26], while the A35K airfoils are based on assumptions made by Oosterom. The nacelle geometry of both aircraft is assumed to be the same and is retrieved from Airbus. Pylon dimensions of the FVK are approximated by Erdincler [32] and are readily available for the A35K. For the FVK landing gear, the positioning and length of the struts are based on the 5.5 configuration without outriggers designed by [34], while the wheel configuration is assumed to be the same as for the Airbus A350-900, which has a MTOM closer to the FVK than the A35K. The engine location of the FVK is based on the research of Pascual [20], which resulted in an optimal location for cruise performance.

Table 2.2 shows the top-level specifications of the FVK and A35K used for this comparison study. For the A35K specifications are retrieved from the Airbus A350 ACAP [40] document and the Trent XWB engine type-certificate sheet [41]. For the FVK passenger, payload and maximum takeoff mass (MTOM) values have been retrieved from the Flying-V family design study [39]. The maximum landing mass (MLM) and dry thrust of the FVK are calculated based on the assumption that the ratio between the MLM and MTOM and the thrust-to-weight ratio of the FVK and the A35K are equal. The FVK approach speed is calculated based on aerodynamic properties and airworthiness regulations assuming a MLM and is close to the A35K approach speed.

Geometric specifications of both aircraft are presented in Table 2.3. The FVK and A35K have the same reference span, but the FVK is shorter in the stream-wise direction, as shown in Figure 2.1. The FVK has a significantly larger wing reference area and therefore a smaller aspect ratio than the A35K. Also, the mean aerodynamic chord (MAC) of the FVK is approximately twice as large as for the A35K. The CG ranges of both aircraft are similar, although this range is located further forward of the main landing gear for the A35K than for the FVK. This can be expected to play a role during rotation on the runway. Due to its landing gear geometry, the FVK features a ground pitch attitude θ_{ground} of -3 degrees, while this is 0 degrees for the A35K. A striking difference between both aircraft is the 9.2 degrees in tailstrike pitch attitude θ_{TS}. Due to this geometric feature the FVK is able to rotate to a much larger pitch attitude on the runway during takeoff than the A35K. The average quarter-chord sweep angle $\overline{\Lambda}_{c/4}$ and wing thickness-to-chord ratio $(\overline{t/c})_w$ are geometric properties that govern wave drag in the transonic flight regime, as will be discussed in section 3.2.3. The FVK features a larger relative wing thickness and significantly larger wing sweep angle than the A35K. Another notable difference between the FVK and the A35K is the location of the engine. For the FVK, the engine is mounted on top of the wing, while the A35K features an under-the-wing engine. The A35K engine is positioned further outboard, which results in a larger yawing moment imbalance in One Engine Inoperative (OEI) situations.

Table 2.1: Aircraft geometry and data sources.

Item	Flying-V-1000 [20, 26, 32, 34, 36, 37, 39, 40]	Airbus A350-1000 [40, 41]
Aerodynamic data	Odilila	Odilila
Inertia tensor	Claeys	Claeys
Centre of Gravity range	Cappuyns	Cappuyns
Planform geometry	Oosterom	Airbus
Airfoil geometry	Palermo	Oosterom
Nacelles geometry	Airbus	Airbus
Pylons geometry	Erdincler	Airbus
Landing gear position	Bourget	Airbus
Landing gear struts	Bourget	Airbus
Landing gear wheels	Airbus	Airbus
Engine position	Pascual	Airbus

Table 2.2: Top-level aircraft specifications.

Item	Unit	Flying-V-1000 [26, 32, 34, 36, 37, 39, 40]	Airbus A350-1000 [37, 39–41]
Number of passengers	-	361	366
Payload mass	10^3 kg	67	67
MTOM	10^3 kg	259	316
MLM	10^3 kg	193	236
Dry thrust	kN	707	863
Thrust-to-weight ratio	-	0.278	0.278
Approach speed	m/s	74.6	75.6

Table 2.3: Geometric specifications.

Item	Unit	Flying-V-1000	Airbus A350-1000
Reference span	m	65	65
Aircraft length	m	57	74
Reference area	m^2	883	462
Aspect Ratio	-	4.8	9.1
Mean aerodynamic chord	m	18.7	9.5
x-coordinate forward CG limit	m	29.4	33.5
x-coordinate rearward CG limit	m	31.7	35.8
CG Range	m	2.34	2.37
x-coordinate nose landing gear	m	6.5	4.6
x-coordinate main landing gear	m	31.8	37.1
θ_{ground}	deg	-3	0
θ_{TS}	deg	19.2	10.0
$\overline{\Lambda_{c/4}}$	deg	55.8	29.6
$\overline{(t/c)_w}$		0.130	0.104
x-coordinate engine	m	37.4	25.8
y-coordinate engine	m	4.7	10.5
z-coordinate engine	m	0.8	-2.1

2.2. FLIGHT PERFORMANCE EVALUATION

As stated in the introduction, the subject of aircraft performance answers practical questions about what an aircraft is capable of and is 'customer friendly'. The customer is not interested in the individual disciplines of aerodynamics, structures or propulsion. Instead, a customer would like to know what runway length is required for the aircraft to take off, how fast it can fly, or how far. The flight performance of an aircraft also determines whether the aircraft complies with airworthiness requirements formulated by aviation safety agencies, such as the European Union Aviation Safety Agency (EASA) and the Federal Aviation Administration (FAA). If an aircraft fails to meet the safety standards specified by these regulatory bodies, the aircraft cannot be admitted into service. For the development of the Flying-V, the relevant airworthiness requirements are specified by the EASA in the Certification Specifications for Large Aeroplanes (CS-25) [42].

In this section, a number of relevant flight performance definitions are briefly discussed that serve to aid the reader in interpreting results presented in chapter 5. Flight performance evaluation of four different flight phases are discussed: takeoff, landing, climb and cruise.

2.2.1. TAKEOFF & LANDING PERFORMANCE

The take-off phase of flight starts at the moment the aircraft starts accelerating on the runway and ends when the lowest point of the aircraft surpasses the screen height. For a dry runway the screen height is defined as 35 ft in CS-25 [43]. The takeoff manoeuvre consists of a ground run and an airborne phase. The ground run consists of a pre-rotation phase and rotation phase, which is initiated at rotation speed V_R. This is an important reference point for the pilot, as the rotation speed can greatly influence the take-off distance and safety. The rotation phase ends when the aircraft is lifted off the ground at the liftoff speed V_{LOF}, which marks the start of the airborne phase. The airspeed at the screen height is the takeoff safety speed V_2. CS-25 defines that takeoff distance as 115% of the takeoff distance defined in Figure 2.2 as a safety factor to account for varying conditions.
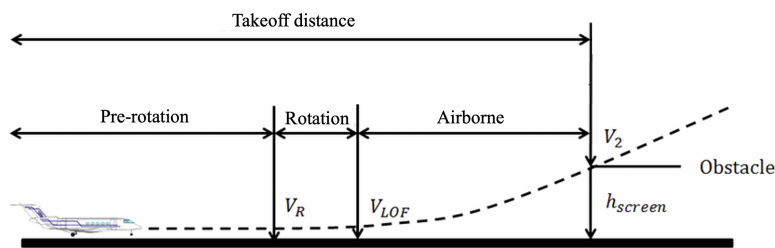
Figure 2.2: Definitions of the different phases of the takeoff manoeuvre and reference speeds. Figure adapted from [44].

In case of an engine failure, it may be decided to abort the takeoff, if the velocity at the instant that the decision is chosen is not greater than the decision speed V_1. This decision speed depends on many factors, such as the aircraft takeoff mass, CG position and the runway altitude and length. One way to define the decision speed V_1 is for the balanced field length (BFL). Definitions of the BFL are shown in Figure 2.3. The BFL is found when the accelerate-climb and accelerate-stop distances are equal to each other. This can be evaluated by simulating an engine failure at a speed V_{EF} and calculating the horizontal distances required to come to a full stop on the runway or continuing takeoff to the screen height. A certain pilot response time between engine failure and the decision speed V_1 should be accounted for. Note that this analysis does not impose a limit on the available runway length. Therefore, during a real takeoff scenario, V_1 may be smaller than the BFL V_1.
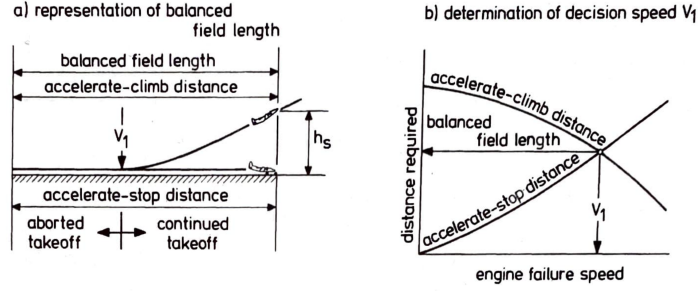
Figure 2.3: The balanced field length concept [45].

Landing performance evaluation makes use of similar phase definitions as the takeoff performance, in reversed order. The landing manoeuvre consists of an airborne phase, followed by derotation to the ground attitude and a braking phase. The landing manoeuvre starts when an aircraft descends below the screen height at the approach airspeed V_{app}. The screen height for landing is defined as 50 ft by CS-25 regulations. An important requirement to consider when determining the approach speed is imposed by CS25.125, which states that the approach speed must be at least 1.23 times the stall speed in landing configuration V_{SR0}:

$$V_{app} \geq 1.23 V_{SR0} \tag{2.1}$$

The landing field length is defined as the horizontal distance from screen height to standstill divided by a safety factor of 0.6 [45, 46]. Definitions of pilot vision are shown in Figure 2.4. In this research the obscured segment during landing will be investigated.
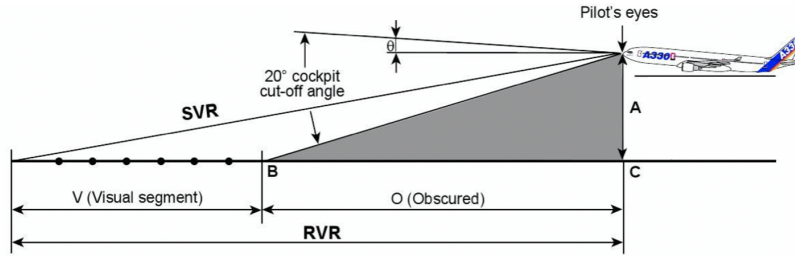
Figure 2.4: Pilot vision definitions. Figure modified from Airbus [47].

2.2.2. Climb Performance

To evaluate the climb performance two parameters will be investigated for different altitudes and airspeeds: the angle of climb (AoC) and the rate of climb (RoC). For steady climb the AoC, also referred to as γ, and RoC can be found using Equation 2.2 and Equation 2.3 [45]. Maximising the AoC results in the steepest climb trajectory, where the aircraft maximises the altitude gained per horizontal distance. Maximising the RoC results in the fastest climb trajectory, where the aircraft maximises the altitude gained per unit time.

$$\sin\gamma = \frac{T}{W} - \frac{1}{L/D} \tag{2.2}$$

$$\text{RoC} = V\sin\gamma \approx \frac{P_{av} - P_{req}}{W} V \tag{2.3}$$

In Equation 2.2, T is thrust, W is the aircraft weight, L is lift and D is drag. During this research only steady, unaccelerated climb has been considered. Assuming a small flight path angle, unaccelerated flight requires thrust equal to drag and lift equal to weight, $T = D$ and $L = W$. The AoC is maximised when excess thrust, the difference between available and required thrust, is maximised as shown in Figure 2.5a. For a given T/W, the AoC is maximised by maximising the aerodynamic efficiency L/D. The maximum RoC is found by maximising excess power, where power is defined as $P = TV$. Figure 2.5b shows the excess power for two special cases: constant power and constant thrust. The available and required power are denoted as P_{av} and P_{req}, respectively. It can be shown that under the aforementioned assumptions, the power required is minimal if C_L^3/C_D^2 is maximised, which maximises RoC for a given P_{av} [45]. Due to the factor V in the power equation, the maximum excess power under these assumptions is located at a higher airspeed than the maximum excess thrust, as long as a positive maximum AoC can be achieved. Therefore, it is expected that the fastest climb trajectory is located at a higher airspeed than the steepest climb trajectory until the aircraft reaches its maximum attainable altitude. The assumption of steady climb results in larger maximum AoC and RoC values than for accelerated climb, where part of the excess thrust/power is required to accelerate the aircraft.

(a) Excess thrust

(b) Excess power
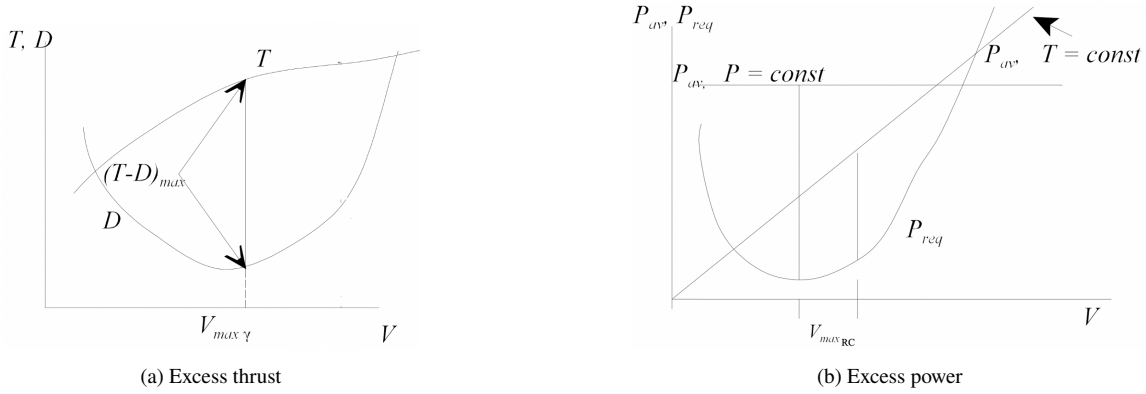
Figure 2.5: Excess thrust and power as a function of airspeed and maximum AoC and RoC conditions [45].

CS25.121 imposes requirements on the climb performance with One Engine Inoperative. For two-engined aircraft, the minimum steady OEI climb gradient that should be achieved at the takeoff safety speed V_2 with the landing gear retracted is 2.4% [43], which corresponds to an AoC of 1.37 degrees.

2.2.3. CRUISE PERFORMANCE

Civil aircraft are usually designed to have a high fuel efficiency during cruise, since the longest time is spent in cruise conditions. It is assumed that during cruise the aircraft flies horizontally at a constant airspeed. In this research the cruise performance is characterised by evaluating the Specific Air Range (SAR) parameter, which quantifies the range covered per unit of consumed fuel [48].

$$\text{SAR} = \frac{R_H}{W}\eta\frac{L}{D} \tag{2.4}$$

The parameter R_H is the range-equivalence of the fuel calorific value of fuel. For jet fuel, this value is taken to be 4400 km [48]. η is the powerplant efficiency, while W is the aircraft weight. It can be seen that the aerodynamic and powerplant efficiencies govern the cruise performance. If the efficiency of the powerplant is neglected, the lift-to-drag ratio can be used to estimate the cruise range. The powerplant efficiency can be written as in Equation 2.5 [49], where a_{SL} is the speed of sound at sea level, TSFC is the thrust specific fuel consumption, and θ is ratio between the ambient temperature and the ambient temperature at sea level.

$$\eta = \frac{a_{SL}}{R_H}\frac{M}{\text{TSFC}/\sqrt{\theta}} \tag{2.5}$$

If TSFC is assumed to be constant, the SAR is proportional to the transonic efficiency ML/D. Therefore the transonic efficiency can be viewed as a simplified performance parameter to estimate the combined efficiency of the aircraft and propulsive system. When the TSFC is not assumed to be constant, the SAR becomes proportional to the Range Parameter RP.

$$\text{RP} = \eta\frac{L}{D} \tag{2.6}$$

<div style="text-align: right">

3

</div>

METHODOLOGY

This chapter describes the methodology used in this research. First the architecture of the flight mechanics model is discussed, followed by a more detailed description of the different sub-models incorporated in the flight mechanics model. After the introduction to the flight mechanics model the procedures to perform different manoeuvres are elaborated upon.

3.1. FLIGHT MECHANICS MODEL

The Performance, Handling Qualities, Load Analysis Toolbox (PHALANX), developed at Delft University of Technology, is used to integrate disciplinary sub-models into a flight mechanics model. This toolbox has already been implemented in several other research applications to unconventional aircraft configurations [50, 51], including studies on the propulsive empennage concept [52], and the trim and transient response of a staggered box-wing aircraft [53, 54]. The purpose of a flight mechanics model is to determine the time evolution of relevant parameters - the dynamics - through solving a set of equations of motion (EOM) at each time instant. PHALANX provides a framework for simulation of flight with 6 Degrees of Freedom (DoF), which can be reduced to 3 DoFs for longitudinal motion. It is assumed that the Earth is flat, non-rotating, exerts a constant gravitational acceleration and has a still air atmosphere that adheres to the International Standard Atmosphere (ISA) [55]. A block scheme representation of a flight mechanics model created with PHALANX is shown in Figure 3.1. The pilot block provides inputs to the control system, which translates the pilot actions to control surface deflections and a throttle setting. In this research, ideal control surface actuators are assumed that instantly deflect the control surfaces as prescribed by the control system. The engine spool up/down time limits the rate at change of the thrust setting. The body, aerodynamic and vehicle-carried North-East-Down (NED) reference frames, will respectively be referred to as the b-frame, a-frame and v-frame and are shown in Figure 3.2. External forces and moments contributions of aircraft components are summed in the b-frame and used to propagate the aircraft state through the classic rigid body dynamic equations presented in Equation 3.1. With respect to the x-, y- and z-axes of b-frame, the respective airspeed components are u, v and w, while external forces excluding gravity are denoted X, Y and Z. $\mathcal{L}$, $\mathcal{M}$ and $\mathcal{N}$ are the external moments about the centre of gravity (CG), and p, q and r are the angular rates of roll, pitch and yaw. The forces and moments are a function of the angle of attack α, angle of sideslip β, flight Mach number M, angular rates of roll, pitch and yaw, and control settings δ. S is the wing reference area, m the aircraft mass and q_∞ the free-stream dynamic pressure. Note that the moment coefficients are all normalised with respect to the reference chord c. To represent the gravitational forces in the body reference frame, the roll angle ϕ and pitch angle θ are accounted for. The moments of inertia tensor I is given in Equation 3.2.

$$
\begin{aligned}
\left\{\begin{array}{c} \dot{u} \\ \dot{v} \\ \dot{w} \end{array}\right\} + \left\{\begin{array}{c} p \\ q \\ r \end{array}\right\} \times \left\{\begin{array}{c} u \\ v \\ w \end{array}\right\} &= \frac{q_\infty S}{m}\left\{\begin{array}{c} C_X(\alpha,\beta,M,p,q,r,\delta) \\ C_Y(\alpha,\beta,M,p,q,r,\delta)\} \\ C_Z(\alpha,\beta,M,p,q,r,\delta) \end{array}\right\} + g\left\{\begin{array}{c} -\sin\theta \\ \cos\theta\sin\varphi \\ \cos\theta\cos\varphi \end{array}\right\} \\
I\left\{\begin{array}{c} \dot{p} \\ \dot{q} \\ \dot{r} \end{array}\right\} + \left\{\begin{array}{c} p \\ q \\ r \end{array}\right\} \times I\left\{\begin{array}{c} p \\ q \\ r \end{array}\right\} &= q_\infty S c\left\{\begin{array}{c} C_{\mathcal{L}}(\alpha,\beta,M,p,q,r,\delta) \\ C_{\mathcal{M}}(\alpha,\beta,M,p,q,r,\delta) \\ C_{\mathcal{N}}(\alpha,\beta,M,p,q,r,\delta) \end{array}\right\}
\end{aligned}
\tag{3.1}
$$

$$
I = \begin{bmatrix} I_{xx} & -I_{xy} & -I_{xz} \\ -I_{xy} & I_{yy} & -I_{yz} \\ -I_{xz} & -I_{yz} & I_{zz} \end{bmatrix}
\tag{3.2}
$$
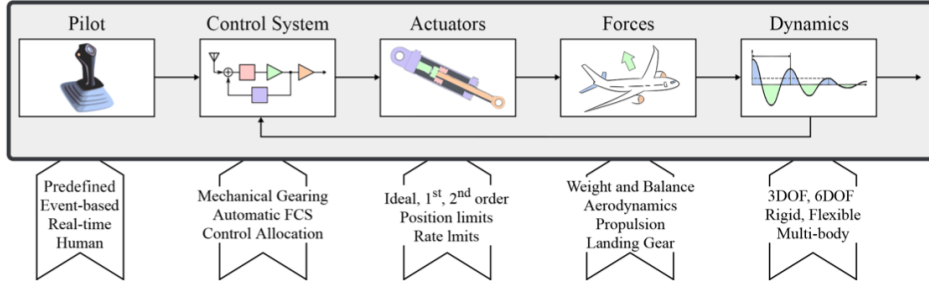
Figure 3.1: PHALANX flight mechanics model overview [56].

(a) Body, wind and aerodynamic reference frames

(b) Body and vehicle-carried NED reference frames
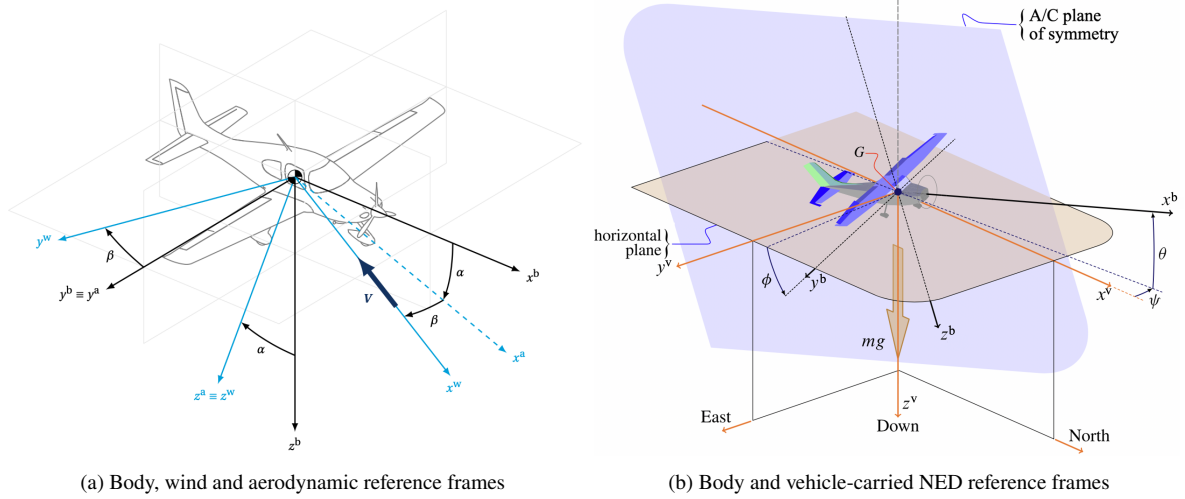
Figure 3.2: Definitions of the body (b), wind (w), aerodynamic (a) and vehicle-carried (v) North-East-Down (NED) reference frames and relative rotation angles [56].

Equation 3.1 shows that the aircraft dynamics are governed by the sum of external forces and moments acting on the aircraft and its mass and inertia properties. The external forces that are considered in this research can be categorised as aerodynamic, propulsive, gravitational and ground contact forces. Aerodynamic forces include contributions from the airframe, control surfaces and the landing gear, which is described in section 3.2. Drag calculations include contributions from zero-lift drag, lift induced drag and wave drag. The estimation of the inertia tensor is discussed in section 3.3. The propulsive model includes a thrust lapse model to correct for altitude and flight speed and is elaborated upon in section 3.4. Ground contact forces are exerted by the landing gear when the wheels make contact with the runway. section 3.5 elaborates on the methodology to determine the contribution of the ground contact forces to the external forces and moments acting on the aircraft.

The EOMs are defined in the aircraft body reference frame, but forces are not necessarily originally defined in the aircraft body reference frame. For instance, aerodynamic drag is assumed to act along the negative wind x-axis, x^w. The gravitational force always acts towards the centre of the Earth, parallel to z^v. Transformation matrices are used to transfer forces from one reference frame to another. The transformation matrices to transform forces from the v-frame to the b-frame - Γ_{bv} - and from the w-frame to the b-frame - Γ_{bw} - are given in Equation 3.3 and Equation 3.4. A general expression to transfer forces from reference frame A to reference frame B is given in Equation 3.5.

$$\Gamma_{bv} = \begin{bmatrix} \cos\psi\cos\theta & \sin\psi\cos\theta & -\sin\theta \\ \cos\psi\sin\theta\sin\phi - \sin\psi\cos\phi & \sin\psi\sin\theta\sin\phi + \cos\psi\cos\phi & \cos\theta\sin\phi \\ \cos\psi\sin\theta\cos\phi + \sin\psi\sin\phi & \sin\psi\sin\theta\cos\phi - \cos\psi\sin\phi & \cos\theta\cos\phi \end{bmatrix} \tag{3.3}$$

$$\Gamma_{bw} = \begin{bmatrix} \cos\alpha\cos\beta & -\cos\alpha\sin\beta & -\sin\alpha \\ \sin\beta & \cos\beta & 0 \\ \sin\alpha\cos\beta & -\sin\alpha\sin\beta & \cos\alpha \end{bmatrix} \tag{3.4}$$

$$F^B = \Gamma_{BA}F^A \tag{3.5}$$

PHALANX has a built-in trimming function based on a prescribed altitude h, airspeed V, sideslip angle β and Euler angular rates p, q and r. The trimming algorithm minimises linear and angular accelerations in the body reference frame and the error in the prescribed sideslip angle ϵ_β. The Euler angles and control settings $\delta = (\delta_{roll}, \delta_{pitch}, \delta_{yaw}, \delta_{throttle})$ that minimise the objective function in Equation 3.6 are found with an iterative, gradient-descent optimisation algorithm. Each δ represents a pilot input, where δ_{roll} represents moving the stick in the lateral direction (positive right), δ_{roll} represents a longitudinal stick deflection (positive forward), δ_{yaw} is a pedal input to control the rudder(s) (right positive) and $\delta_{throttle}$ is the throttle setting. Thrust reversers are not considered in this research.

$$\min f(\phi, \theta, \psi, \delta) = || \left(\dot{u}, \dot{v}, \dot{w}, \dot{p}, \dot{q}, \dot{r}, \epsilon_\beta \right) || \tag{3.6}$$

The trim problem formulation depends on the DoFs of the equations of motion. Choosing 2D EOMs eliminates δ_{roll}, δ_{yaw} and the Euler angles ϕ and ψ from the trim problem. Prescribing values for other control variables further constrains the trimming problem. Either a thrust setting $\delta_{throttle}$ or a flight path angle γ must be always be prescribed.

3.2. Aerodynamics

This section elaborates on the aerodynamic sub-model used in the present research. Figure 3.3 shows the untrimmed aerodynamic efficiency and lift curves of the FVK and A35K in take-off, landing and cruise configuration. with landing gear retracted. Aerodynamic forces consist of lift and drag, where drag can be subdivided into many different categories. In this research, drag is divided into lift induced drag, zero-lift drag and wave drag contributions.
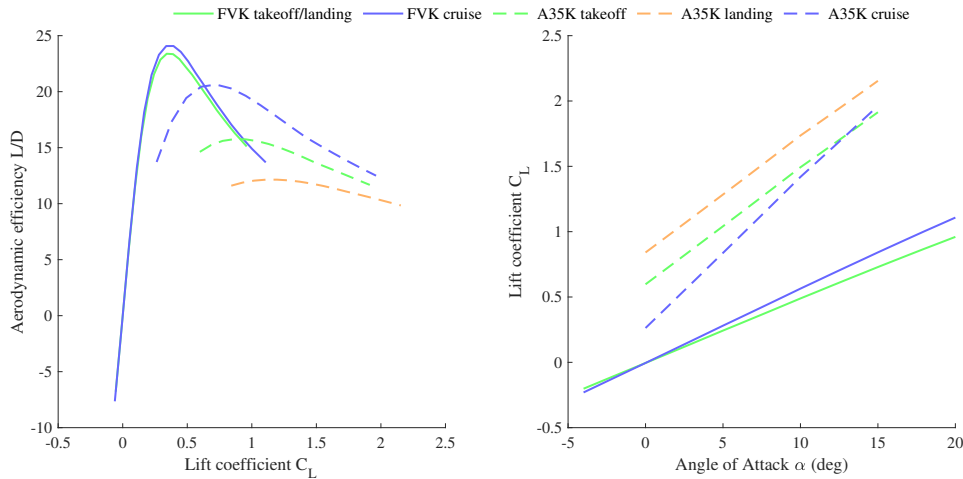
Figure 3.3: Aerodynamic polars of the Flying-V-1000 and Airbus A350-1000 in takeoff, landing and cruise conditions.

3.2.1. Lift & Lift Induced Drag

A database of aerodynamic forces and moments on the aircraft is generated using Odilila, a Vortex Lattice Method (VLM) developed and verified by Airbus [37]. VLMs assume an incompressible, inviscid and irrotational flow field and are therefore inherently limited. Thickness and viscosity effects are omitted in VLM calculations. Nevertheless, VLMs are often used in the preliminary and conceptual design phase due to its low computational cost and ability to calculate lift curve slopes, induced drag and stability derivatives. In this case, this VLM has been chosen because it has been extensively validated and provides force and moment coefficients for many different angles of attack (AoA), Mach numbers, Euler angular rates and control surface deflections. Verification of the predictive qualities of Odilila for lift curve slopes and induced drag has been performed in previous research [36, 37] and can be found in Appendix E. The aerodynamic database includes forces and moments in the aircraft body reference frame for AoAs ranging from -5 to 20 degrees for the FVK and 0 to 17 degrees for the A35K. Asymptotic Mach numbers range from 0.2 to 0.85. For the same range of AoAs and Mach numbers, contributions due to non-zero angles of sideslip (AoS), Euler angular rates and control surface deflections are calculated by Odilila under the assumption that the superposition principle holds. This means that these contributions are completely decoupled and linear. Equation 3.7 shows a general formulation of the forces and moments outputted by Odilila, denoted by F. F_0 is a function of the AoA and flight Mach number and represents the contribution of

the airframe alone at zero AoS and angular rates ω_b. Note that control surface deflections are denoted by δ_{cs}.

$$F(\alpha, M, \beta, \Omega_b, \delta_{cs}) = F_0(\alpha, M) + \frac{\partial F(\alpha, M)}{\partial \beta} \beta + \frac{\partial F(\alpha, M)}{\partial \omega_b} \omega_b + \frac{\partial F(\alpha, M)}{\partial \delta_{cs}} \delta_{cs} \tag{3.7}$$

The wing planform of the Flying-V and reference aircraft used to generate aerodynamic datasets in Odilila resemble the FVK as designed by Oosterom [39] and the Airbus A350-900, from now on referred to as A359, respectively. A planform comparison is shown in Figure 3.4a. The Odilila analyses have been performed during a previous study [37] and therefore the geometries of the Odilila models of the Flying-V and the reference aircraft were determined before the present research was carried out. Hence, it was not possible to generate a new Odilila model for the A35K. This is not problematic, because the A359 data can be corrected to obtain a database for the A35K.

(a) Planform comparison   (b) Control surfaces defined in Odilila
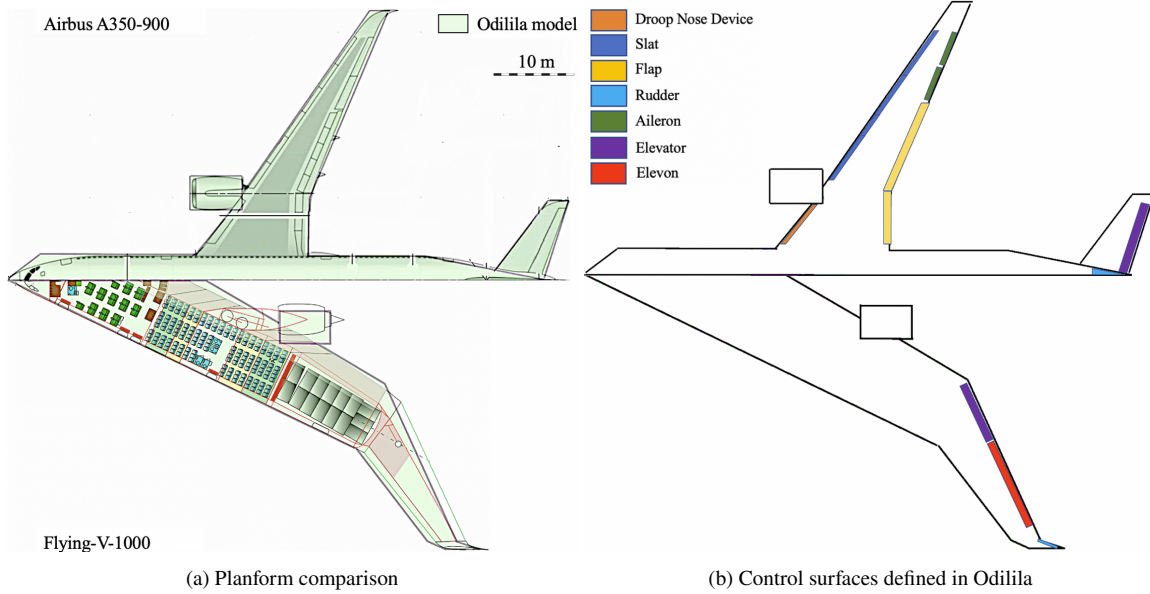
Figure 3.4: Planform comparison of the Odilila models with the Airbus A350-900 and Flying-V-1000 and control surface definitions.

The Odilila reference aircraft model and A359 have very similar planforms. The most notable differences are the absence of a winglet on the Odilila model and a slightly less tapered outer wing. For the Flying-V, the Odilila model features an inboard wing with a larger chord length and smaller span than the FVK, while the total wing span is the same. The outboard wing segment is smaller and has slightly more sweepback for the FVK than the Odilila model. Therefore it could be that the aerodynamic centre of the FVK would be positioned more rearward than for the Odilila model, but this is highly uncertain and the potential difference is expected to be small. Another notable difference is the positioning of the engine, which is placed more inboard on the FVK compared to the Odilila model. The latter is not expected to make a large impact, as the engine nacelles are not expected to generate much lift. The A359 and A35K have very similar aerodynamic characteristics, as both have the same main wing and empennage. The A35K has a slightly larger winglet than the A359. The most notable difference between the A359 and A35K is the extended fuselage, which is not a lifting surface. It is deemed acceptable to adapt the A359 database generated by Odilila to obtain a database for the A35K. The main difference that has been corrected for is the longer moment arm of the empennage with respect to the CG. This difference is shown in Figure 3.5. The moment reference point of the A35K database is shifted aft by 3.81m with respect to the A359, while the empennage moment arm is increased by 6.98m.

Control surfaces

The Flying-V and reference aircraft models are equipped with a number of control surfaces, shown in Figure 3.4b. Both aircraft feature trailing edge devices for roll and pitch control and rudder(s) for yaw control. The outboard control surface of the main wing of the Flying-V is categorised as an elevon due to its dual function in both pitch and roll control, while the inboard control surface is categorised as an elevator as it is only used for pitch control. The reference aircraft also features slats, flaps and a droop nose device (DND). Six different combinations of flap, slat and DND deflections are included in the aerodynamic database of the reference aircraft, which are
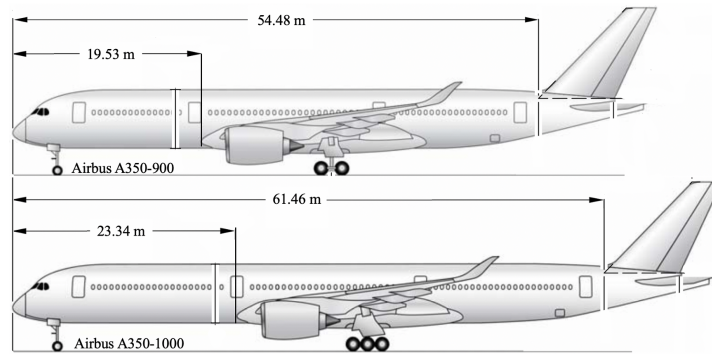
Figure 3.5: Airbus A350-900 and Airbus A350-1000 sideview comparison. Figures modified from Airbus [40].

tabulated in Table 3.1. It can be seen that a fixed symmetric aileron deflection is also part of the configuration specifications. This table also shows the high lift device configurations of the A359 during takeoff and landing, as specified in the Flight Deck and Systems Briefing for pilots [57]. It has been decided to use Odilila configuration 5 for takeoff simulations and configuration 6 for landing simulations, as these have the closest resemblance to the A359 configurations. Odilila configuration 1 is used to simulate climb and cruise flight. Flap, slat and DND deflections are not part of the δ_{cs} term in Equation 3.7, but are included in the F_0 contribution. The Flying-V in its current state does not incorporate additional high lift devices. The elevons, elevator and rudder are controlled by pilot inputs and are assumed to have a deflection saturation limit of 30 degrees. The reference aircraft uses the ailerons, elevator and rudder for roll, pitch and yaw control respectively. The Flying-V uses both the elevon and elevator (with equal deflection angles) for pitch control, while the elevon and rudder are used for roll and yaw control respectively.

Table 3.1: Odilila reference aircraft model high lift device configurations compared with A359 landing and takeoff configurations as specified in the Flight Deck and Systems Briefing for Pilots [57].

Configuration	DND (deg)	Slats (deg)	Flaps (deg)		Symmetric ailerons (deg)	
			Inboard	Outboard	Inboard	Outboard
Odilila 1	0	0	0	0	0	0
Odilila 2	18	18	0	0	0	0
Odilila 3	18	18	10	10	5	5
Odilila 4	23	23	15	15	5	5
Odilila 5	23	23	20	20	5	5
Odilila 6	27	27	40	40	5	5
A359 Takeoff	16.7	18	26	26	-	-
A359 Landing	25	27	37.5	37.5	-	-

For each control surface - except the high lift devices - Odilila provides values for the change in the aerodynamic forces and moments due to a ±1 degree control surface deflection. A linear relation between control surface deflection and the resulting forces and moments is assumed. For this research it is mostly interesting to look at the control surface contributions to lift, drag and the pitching moment as, apart from climbing with OEI, the aircraft motion is limited to longitudinal motion. For the Flying-V Odilila predicts that the lift, drag and pitching moment contributions of both rudders cancel each other out completely, as the rudders are deflected asymmetrically with respect to the aircraft symmetry plane and the aerodynamic coefficients are exactly mirrored for positive and negative control surface deflections. Apparently, Odilila draws the conclusion that the resulting sideforce or altered lift distributions of the wings do not result in a net lift or drag force. Asymmetric deflection of the Flying-V outboard elevons for roll control yields the same result as rudder deflection. For the Odilila reference aircraft similar results are obtained for rudder and aileron deflections, as the net lift and pitching moment contributions are zero. A drag contribution of 0.1 drag count per degree deflection is generated by each of these control surfaces for the reference aircraft. These contributions are so small that they have almost no influence on the simulations. It seems that for the calculation of drag due to control surface deflection, Odilila focuses on the change in lift that is generated and the resulting change in lift induced drag. Hence, only the Flying-V main wing trailing edge devices and the reference aircraft elevator have meaningful contributions to the total lift, drag and pitching

moment.

Figure 3.6 shows the influence of the the FVK elevator and elevon, and A35K elevator on the lift, drag and pitching moment. The middle of the allowed CG position range has been used as the moment reference point. For all three control surfaces, deflections with opposite signs yield lift, drag and pitching moment contributions of opposite sign. Therefore, the change in these aerodynamic properties can be characterised by the derivative with respect to control surface deflection. The derivatives of lift, drag and pitching moment with respect to control surface deflection are denoted L_δ, D_δ and $\mathcal{M}_\delta$, respectively. As both aircraft have reference areas and reference chord lengths that are quite different, as presented in Table 2.3, it has been chosen to normalise lift, drag, and pitching moment with respect to the free-stream dynamic pressure to draw a meaningful comparison. Since the FVK uses both the elevator and elevon simultaneously for pitch control, these contributions should be added together and compared to the A35K elevator. For the same pilot pitch command, it can be concluded that the FVK generates more additional lift and drag than the A35K, while also generating a larger pitching moment about the CG.
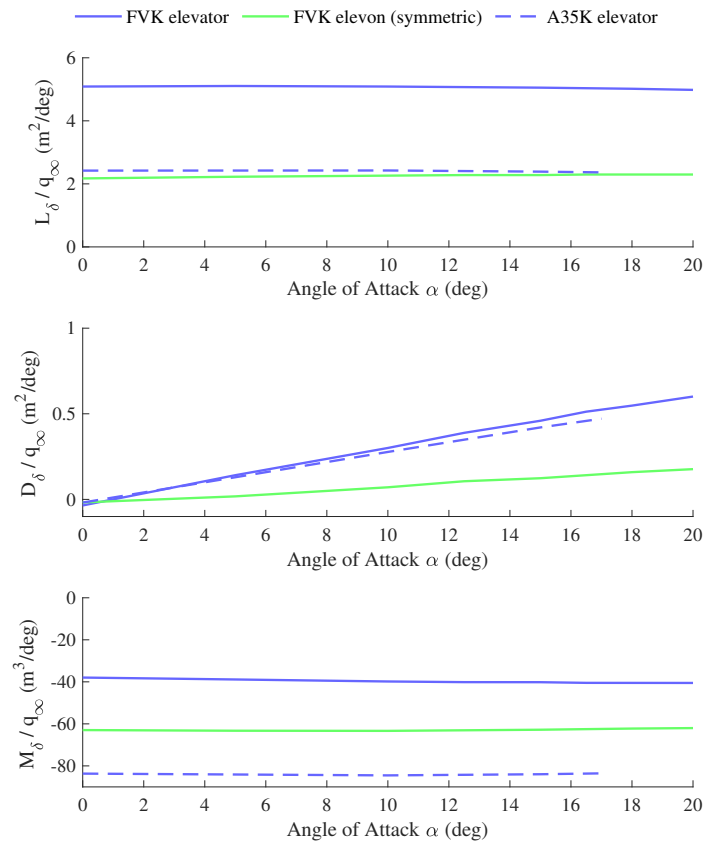
Figure 3.6: Derivatives of the lift area (top), drag area (middle) and pitching moment divided by dynamic pressure (bottom) with respect to control surface deflection as a function of AoA.

GROUND SPOILERS

During braking on the runway many aircraft use ground spoilers to enhance the braking performance. A deflected spoiler generates additional aerodynamic drag, but also acts as a lift-dumping device which increases the load on the main gear wheels. The maximum braking force that can be applied without skidding increases as the load on the main gear wheels increases. Therefore using ground spoilers can potentially reduce the required braking distance to standstill on the runway. Recently a study into various ground spoilers on the Flying-V and their effectiveness has been completed [32] which has shown that ground spoilers can be effectively implemented on the Flying-V. In the present research, ground spoilers have been implemented for the FVK as well as the A35K. The spoiler effectiveness has been modelled as a change in lift coefficient, based on the results of Erdincler [32], shown in Figure 3.7. The figure shows the change in lift and drag coefficient comparison as a function of spoiler deflection at a given braking attitude. Note that the braking attitude in this previous research is -2.5 degrees, as this is the smallest attitude that was considered. In the present research the ground attitude is -3 degrees, in agreement with a study into the Flying-V landing gear [34]. Although this small discrepancy is noted, it is deemed

acceptable to use the values shown in Figure 3.7 for the present research. For the A35K the spoiler performance has been based on data from the Boeing 747 [58] at ground attitude for flap deflections of 0 and 30 degrees. Depending on the selected flap settings (combinations can be found in Table 3.1) the corresponding ΔC_L is found by assuming a linear variation with flap deflection angle. The non-dimensional projection height of the spoiler is assumed to be 0.1. As the lift coefficient is normalised with the wing reference area it is deemed acceptable to use the B747 coefficient values that are shown in Figure 3.7 for the A35K. The change in lift coefficient as modelled in the present research is shown in Table 3.2. The drag change due to spoiler deflection is neglected, as the Flying-V and B747 show very different trends and could possibly hand the Flying-V an unfair advantage when comparing braking performance.

Table 3.2: Flying-V-1000 ($S = 883$ m^2) and A350-1000 ($S = 462$ m^2) modelled spoiler effectiveness. Flap deflection in degrees.

	Flying-V-1000	Airbus A350-1000
ΔC_L	-0.16	-0.13 -0.34 ($\delta_{\text{flap}}/30$)
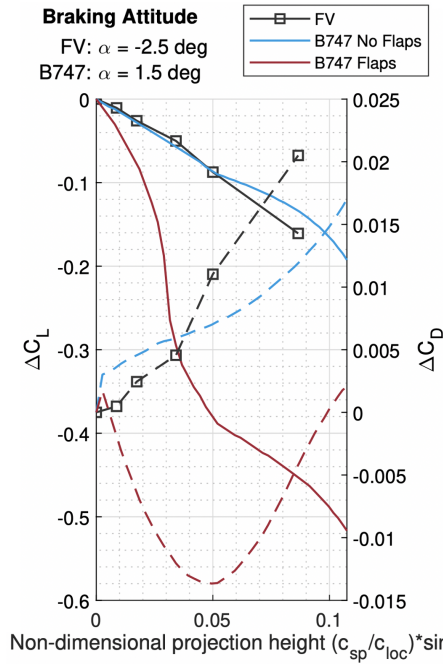
Figure 3.7: Spoiler performance of the Flying-V and Boeing 747. Solid line is ΔC_L, dashed line is ΔC_D [32].

3.2.2. ZERO-LIFT DRAG

To account for thickness, viscosity and interference effects, the aerodynamic database from Odilila is enhanced with a zero-lift drag module based on empirical relations deduced by Raymer [59] and Torenbeek [60]. A complete overview of the used relations and input parameters for the zero-lift drag calculations can be found in Appendix A. Contributions of the wings, fuselage, nacelles, pylons, landing gear, flaps and drag due to leakage and protuberances are summed to calculate the total zero-lift drag.

$$C_{D_0} = C_{D_{0\text{wings}}} + C_{D_{0\text{fus}}} + C_{D_{0\text{nac}}} + C_{D_{0\text{pyl}}} + C_{D_{0\text{LG}}} + C_{D_{0\text{leak}}} + C_{D_{0\text{flap}}} \tag{3.8}$$

For the wings, fuselage, nacelles and pylons the zero-lift drag coefficient is calculated using the flat plate skin-friction coefficient C_f, a form factor f to account for wave drag, an interference factor Q and the wetted area of the component S_{wet}. For each component the zero-lift drag contribution can be calculated using Equation 3.9, where subscript c denotes the respective component.

$$C_{D_{0c}} = C_{f_c} \cdot f_c \cdot Q_c \frac{S_{\text{wet}_c}}{S} \tag{3.9}$$

It is assumed that the flow is turbulent due to the large Reynolds numbers during operation. The flat plate skin-friction coefficient for turbulent flow is given by Equation 3.10 [59].

$$C_f = \frac{0.455}{(\log_{10} Re)^{2.58} (1 + 0.144 M^2)^{0.65}} \tag{3.10}$$

The skin friction coefficient is a function of the Reynolds number Re, which depends on the characteristic length scale of each component. Hence, the skin friction coefficient has to be calculated for each component separately. Equations for the form factor and wetted area of each component are presented in the sections below. The interference factor Q has been taken from Raymer [59], where a mid-range value is chosen in the cases where a range of valid values was presented. A summary of the parameters in Equation 3.9 for each aircraft component is displayed in Table A.1 and Table A.2 for the FVK and the A35K, respectively. The estimated zero-lift drag coefficients of each component during takeoff, landing and cruise are presented in Table 5.1. It is assumed that the zero-lift drag force does not contribute to the aerodynamic moments about the aircraft CG as it is assumed that the moment arm of the different components is small. Moreover, the additional pitching moment contributions have been found to be insignificant during previous research [32]. Only for landing gear zero-lift drag, which gives rise to separate moment contributions due to drag of struts and wheels (presented in Table A.6), a moment contribution is calculated due to its relatively large magnitude and moment arm. Nevertheless, this contribution is still relatively insignificant.

In the event on an engine failure, the drag due to asymmetric rudder deflection is accounted for and additional drag due to a blocked rotor or windmilling engine is also modelled using the Equation 3.11 [60].

$$C_{D_{\text{wme}}} = \frac{0.0785 D_{\text{inlet}}^2 + \frac{2}{(1+0.16 M^2)} \frac{\pi}{4} D_{\text{inlet}}^2 \frac{V_n}{V} \left(1 - \frac{V_n}{V}\right)}{S} \tag{3.11}$$

D_{inlet} is the engine inlet diameter, M is the free-stream Mach number and V_n/V is the ratio of mean nozzle exit velocity to the free stream velocity. This last figure is typically 0.12 for a high bypass ratio engine [60]. The inlet diameter is taken to be 3.17m [40] and the windmilling drag force is assumed to act along the negative x-axis in the wind reference frame. To calculate the moments due to windmilling drag the drag force is assumed to be exerted at the engine location listed in Table 2.3.

3.2.3. Transonic Wave Drag

At high subsonic Mach numbers, compressibility effects become increasingly more pronounced as supersonic velocities are reached locally ending in shock waves, causing wave drag to increase [61]. To account for this effect, a simple wave drag model is implemented. The so-called delta method is an empirical model based on experimental data of 19 subsonic and supersonic military aircraft and 15 advanced or supercritical airfoils [62]. For the experimental data that the research was based upon, this drag estimation method was valid for Mach numbers up to 2.0. A comparison study of different wave drag prediction methods has shown that the Delta method was the most effective method available at the time [61]. The three-dimensional drag divergence number is estimated based on the two-dimensional drag divergence number, which is then corrected for quarter-chord sweep and aspect ratio.

$$M_{\text{dd3d}} = M_{\text{dd2d}} + \Delta M_{\Lambda_{c/4}} + \Delta M_{\text{AR}} \tag{3.12}$$

Measures to increase M_{dd3d} include increasing the sweep angle, reducing the aspect ratio of the wing and reducing the thickness-to-chord ratio. As the FVK has a large reference area, it can fly at a significantly smaller lift coefficient than the A35K. According to the Delta method this leads to a more favourable M_{dd3d} due to a smaller M_{dd2d}. The average leading edge sweep angle and thickness-to-chord ratio used for the wave drag computations are presented in Table 2.3. The wave drag estimation method is further explained in Appendix B. The three-dimensional drag divergence number and its components for both aircraft are shown in Table 5.2. Although the Delta method data includes a wide range of aircraft with sweep angles up to 60 degrees and aspect ratios as low as 4.7, it must be noted that none of the investigated aircraft was a flying wing. Therefore it is not known whether this method could also be accurately applied to this unconventional aircraft configuration. The fuselage wave drag has also been accounted for, although its contribution is small. For more information regarding fuselage wave drag the reader is referred to Appendix B.

3.2.4. Ground Effect

During takeoff and landing, the proximity of the ground significantly influences the flow field compared to unbounded flow. The formation of tip vortices is obstructed by the ground, preventing the tip vortices from

developing as strongly as they would in unbounded flow, reducing the downwash on the wing, which reduces induced drag and increases lift. The magnitude of this so-called ground effect increases as the altitude-to-span ratio decreases, which for the particular case of the Flying-V has been investigated [24]. The change in lift coefficient and drag coefficient as a function of AoA at different height-to-span ratios h/b with respect to unbounded flow conditions is given in Figure 3.8. In this definition, the height is measured at the trailing edge of the main wing tip. It must be noted that there are several factors that suggest that the influence of the ground effect would be
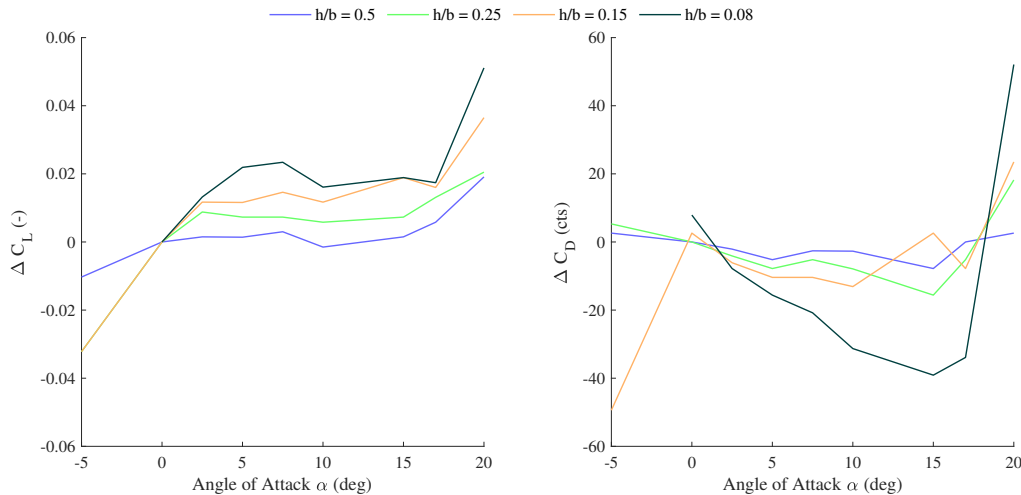
Figure 3.8: Influence of ground effect on the lift and drag coefficient as a function of AoA and ride height [24].

overestimated using the results presented in Figure 3.8. First of all, the results have been obtained using CFD simulations and are the steady state solutions from a converged flow field. In a dynamic situation the flow field would need some time to adapt and therefore the effect would be smaller. If the aircraft pitch attitude becomes large while on the runway, which would happen towards the end of the rotation phase of the takeoff run, the ride height would decrease to a fraction of the smallest tested value. Therefore the ride height would be much smaller than any value investigated and it must be noted that in such conditions the uncertainty in the magnitude of the ground effect would be quite large. Moreover, the data of the drag coefficient change due to the ground effect at negative AoA seems to contain an outlier at -5 degrees. As a result, the drag coefficient at the ground attitude of -3 degrees could be underestimated. These factors should be taken into account when interpreting the results from ground effect influence studies.

3.2.5. Limitations
Odilila is a Vortex Lattice Method, hence viscous effects are not accounted for. Therefore Odilila is unable to predict stalling characteristics or non-linear behaviour. In the largest part of the flight envelope, linear behaviour is expected. However, for a highly swept wing like Flying-V, vortex lift can be expected at high angles of attack. Wind tunnel experiments [25] have shown an increase in lift curve slope between 12.5 and 20 degrees AoA due to this phenomenon. Figure 3.3 shows that the lift curve slope of the Flying-V computed by Odilila is linear over the entire AoA range, showing that vortex lift is not included. Wind tunnel experiments [26] have shown that the Flying-V shows pitch-up tendencies at approximately 20 degrees AoA. For this research it is therefore assumed that it is undesirable to allow AoA values larger than 20 degrees for the FVK. For the A35K this limit is assumed to be an AoA of 15 degrees. Figure 3.3 also hints at the limitations of Odilila, as the lift curve slopes of the A35K in takeoff and landing configuration are less steep than in clean configuration. This is unexpected, as the deployment of high lift devices actually increases the effective wing area, while the reference area stays the same. Therefore it would be expected that the slope of the lift curve would increase as high lift devices are deployed, but the opposite happens. This shows that the modelling accuracy of high lift devices in Odilila is limited. The Odilila model of the reference aircraft resembles the A359, while this research compares the FVK to the A35K. However, as the lifting surfaces of both aircraft are basically identical and corrections have been applied to the aerodynamic moments and zero-lift drag, this difference is expected to have a negligible influence. Both the zero-lift drag and wave drag models are empirical models, making their accuracy dependent on the underlying experimental data. For an unconventional aircraft configuration like the Flying-V this means that the predictive qualities of these empirical models are uncertain, as none of the sampled aircraft are flying wings.

3.3. WEIGHT, INERTIA AND CENTRE OF GRAVITY

The weights and moment of inertia (MOI) tensors of the Flying-V and the reference aircraft are estimated based on a combination of previously performed researches and publicly available information. The MTOM and MLM of the A35K are publicly available [40], while the MTOM of the FVK is based on the Flying-V family design study [39] and its MLM-to-MTOM ratio is assumed to be equal to the A35K. The corresponding values are presented in Table 2.2. The starting point for the estimation of the MOI tensor I is a structural analysis of the FVK and A359 , which used Finite Element Method (FEM) calculations to structurally size both aircraft for a given MTOM [36]. The mass of non-structural items was estimated using empirical relations. From the resulting mass distributions MOI tensors were calculated for MTOM and operating empty mass (EOM). In this research a linear variation of MOI is assumed if the aircraft mass is chosen to be a different value than the MTOM or EOM. For consistency, the MTOM and EOM values that are used for this linear scaling are the values obtained by the structural sizing study, as they correspond to the mass distributions yielding the estimated MOI tensors. For the FVK, the estimated MOI of the structural sizing study are adopted, because the assumed MTOM and the value used in this study are the same and the wing planforms of both models are very similar. The MOI tensor of the A35K is estimated based on the A359 values found by the structural sizing study. The adaptation is mainly based on the extended fuselage of the A35K. In Appendix C the adaptation method is presented, including a justification. The resulting moments of inertia around the principal body axes used in the present research are presented in Table 5.3. These moments of inertia have been calculated with respect to a reference position, which is 55% MAC for the FVK and 30.5% MAC for the A35K [37]. Therefore, when a different center of gravity location is used than these reference points, an additional inertia term has to be added according to Huygens-Steiner theorem, using Equation 3.13. This additional term will be referred to as the Steiner term. In Equation 3.13, I_{ref} is the moment of inertia with respect to a reference point, which corresponds to the values in Table 5.3. The newly calculated MOI including Steiner term is denoted as I, m is the total mass of the aircraft and d is the distance between the inertia reference point and the centre of gravity, perpendicular to the rotation axis.

$$I = I_{ref} + md^2 \qquad (3.13)$$

Due to assumed symmetry of the mass distribution about the x-axis, the terms I_{xy} and I_{yz} and I_{xz} from Equation 3.2 are zero.

Previous research using the same Odilila model [37] investigated the range of CG locations that can be chosen for the Flying-V. For the FVK the most forward CG location was found by determining the most forward CG location that allows a pull up manoeuvre with a load factor of 1.3g to be performed during approach. The most rearward CG location was determined by finding the point where the static margin is 2.5%. For the A35K the CG limits are taken from the A350 ACAP [40]. The CG range adopted in this research for both aircraft can be found in Table 2.3.

3.4. PROPULSION

Both the reference aircraft and the Flying-V employ a high-bypass ratio (BPR) engine, similar to the Rolls Royce Trent XWB [40]. It is assumed that both aircraft have the same thrust-to-weight ratio and a BPR of 10. The engine location is defined at the centre of the fan and is the assumed application point of the thrust force, which is assumed to only have a component parallel to the body reference frame x-axis. The assumed engine location of the Flying-V has been taken from previous research into the optimal engine location [20, 21] and is presented in Table 2.3.

A thrust lapse model derived empirically by Bartel and Young [63] based on engine data of four two-shaft turbofan engines is used to predict the available thrust for different altitudes and flight Mach numbers. The engines considered in the Bartel-Young model have bypass ratios ranging from 3 to 9 and overall pressure ratios (OPR) ranging from 18 to 36. Although the engines used in the present research have a BPR and OPR of approximately 10 and 50, respectively, it is assumed that the Bartel-Young model predicts thrust lapse reasonably well for these engines as well, as the model allows for corrections based on the BPR. Existing empirical equations were updated by Bartel and Young to better fit the turbofan engines that existed at that moment. The Bartel-Young model consists of a takeoff, climbing and cruise thrust model, and was found to predict the available thrust within 1% accuracy during takeoff up to Mach 0.4, and within 4% accuracy during climb. For this study, the models for thrust during take-off and climb have been used, which are discussed in more detail in section 3.4.1 and section 3.4.2 respectively.

In Figure 3.9a the maximum available thrust as function of altitude and Mach number predicted by the takeoff and climb thrust models are compared. It can be seen that at sea level, the thrust of these two models match at

$M \approx 0.37$, while at an altitude of 1 km the cross-over point is at $M \approx 0.45$. It has been chosen to use the takeoff model for Mach numbers up to 0.4 and below altitudes of 1 km. The maximum available thrust predicted by this merged model as a fraction of the Static Sea Level (SSL) thrust is shown in Figure 3.9b.

(a) Takeoff and climb thrust model comparison

(b) Merged thrust lapse model
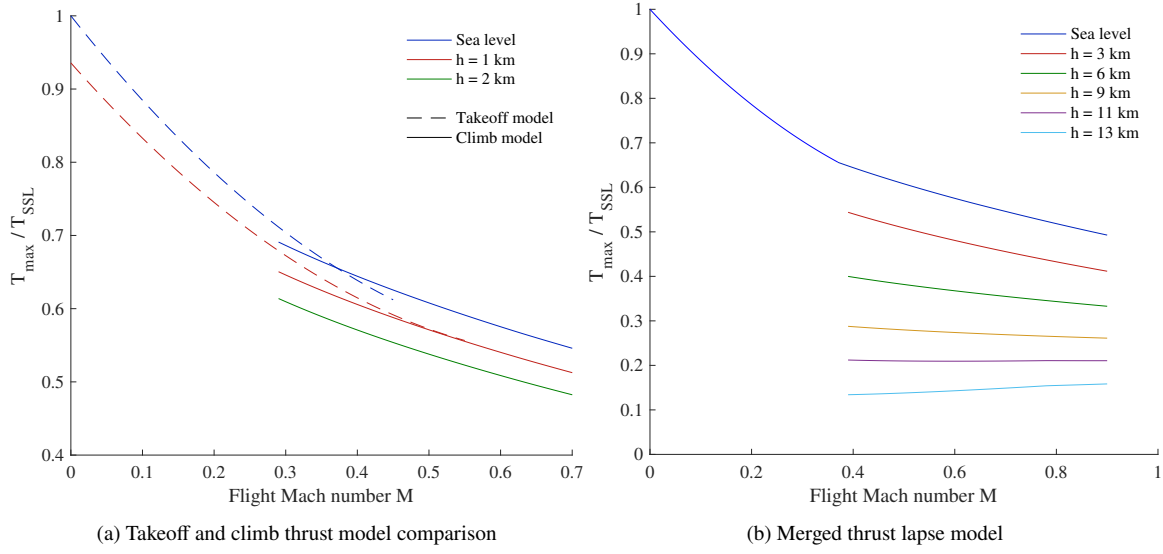
Figure 3.9: Ratio between maximum available thrust T_{max} and static Sea Level thrust T_{SSL} as a function of Mach number and altitude, for a 10 BPR turbofan engine.

3.4.1. TAKEOFF THRUST

Bartel and Young adjusted an empirical relation derived by Torenbeek [60] to incorporate altitude and flight Mach number effects and to fit the available engine data, resulting in Equation 3.14. G_0 is the gas generator function at sea level, which can be estimated using Figure D.2. T_{SSL} is the static sea level thrust. The empirical coefficients c_1, c_2 and c_3 account for the difference in ambient pressure [63]. The ratio between ambient pressure, which is assumed to adhere to ISA standards, and sea level ambient pressure is denoted Π.

$$\frac{T}{T_{SSL}} = c_1 - \frac{0.377(1+\text{BPR})}{\sqrt{(1+0.82\text{BPR})G_0}} c_2 M + (0.23 + 0.19\sqrt{\text{BPR}})c_3 M^2 \tag{3.14}$$

$$\begin{pmatrix} c_1 \\ c_2 \\ c_3 \end{pmatrix} = \begin{pmatrix} 0 & -0.4327 & 1.3855 & 0.0472 \\ 0.1377 & -0.4374 & 1.3003 & 0 \\ 0.9106 & -1.7736 & 1.8697 & 0 \end{pmatrix} \begin{pmatrix} \Pi^3 \\ \Pi^2 \\ \Pi \\ 1 \end{pmatrix} \tag{3.15}$$

Using Equation 3.14 the thrust of the four reference turbofan engines could be estimated within a 1% error interval up to Mach 0.4, significantly improving Torenbeek's model, which was accurate up to Mach 0.2 [63].

3.4.2. CLIMB THRUST

To estimate the thrust for different altitudes and flight Mach numbers during climb, the climb phase has been divided into three segments by Bartel and Young, shown in Table 3.3. For the climbing thrust model, a reference thrust value at 30,000 ft is required, which is estimated using an equation and engine performance curves provided by Scholz [64], which are shown in Figure D.3. From these curves, the ratio between the maximum continuous thrust $T_{max\ cont}$ and maximum available thrust T_{max} has been estimated to be ≈ 0.85. This value is in good agreement with the specifications of $T_{max\ cont}/T_{max}$ at sea level for the engines of the A359 and A35K, the Trent XWB-84 and -97 [41].

For a flight Mach number of $M \approx 0.8$, the maximum continuous thrust in cruise, can be approximated using Equation 3.16 [64] for varying cruise altitude h_{cr} and bypass ratio BPR. Combining this equation with the estimated $T_{max\ cont}/T_{max}$, the reference thrust value at 30,000 ft required for the climb thrust model is found to be $T_{30} \approx 0.264 T_{SSL}$.

$$T_{max\ cont} = T_{SSL}\left((0.0013 \cdot \text{BPR} - 0.0397)\frac{h_{cr}}{\text{km}} - 0.0248 \cdot \text{BPR} + 0.7125\right) \tag{3.16}$$

Table 3.3: Climb segment definition used by Bartel and Young [63].

Segment	Altitude	Flight speed
1	0-10,000 ft	200-300 kts
2	10,000-30,000 ft	250-350 kts
3	30,000-40,000 ft	Mach 0.67-0.91

SEGMENT 1

In segment 1 thrust varies almost linearly with altitude for a constant calibrated airspeed V_{cas}. Therefore, the available thrust in this segment can be calculated with the linear function given in Equation 3.17. $V_{cas,ref}$ is the reference calibrated airspeed, corresponding to M_{ref} at 30,000 ft. The reference Mach number M_{ref} is the cruise Mach number of the aircraft, which is 0.85 in this study for both aircraft. The subscripts 10 and 30 refer to values at 10,000ft and 30,000ft respectively, while the ambient pressure is denoted by p. The available thrust at 10,000ft, T_{10} is determined using Equation 3.18.

$$\frac{T}{T_{30}} = n_1 \left(\frac{p_{10}}{p_{30}}\right) + \left[\left(\frac{T_{10}}{T_{30}}\right) - n_1 \left(\frac{p_{10}}{p_{30}}\right)\right] \tag{3.17}$$

The empirical factor n_1 takes the climb rate and calibrated airspeed into account. The values for n_1 for fast climb are tabulated in Table 3.4.

Table 3.4: Empirical factor n_1 for different calibrated airspeeds [63].

$V_{cas}/V_{cas,ref}$	n_1
0.67	0.40
0.75	0.39
0.83	0.38
0.92	0.37
1.00	0.36

SEGMENT 2

In the second climb segment the available thrust is calculated using Equation 3.18.

$$\frac{T}{T_{30}} = \left(\frac{V_{cas}}{V_{cas,ref}}\right)^{-0.1} \Pi^{-0.355\left(\frac{V_{cas}}{V_{cas,ref}}\right)+n_2} \tag{3.18}$$

The exponent n_2 relates to the variation of turbine inlet temperature (TIT) of the engine with altitude for different climb rates. The values for n_2 for slow, moderate and fast climbing are 0.89, 0.93 and 0.97 respectively. Since the aim is to determine the maximum available thrust, the fast climbing value $n_2 = 0.97$ is used in this study.

SEGMENT 3

The available thrust during the third climb segment is calculated using Equation 3.19.

$$\frac{T}{T_{30}} = n_3 \ln(\Pi) + \left(\frac{M}{M_{ref}}\right)^{-0.11} \tag{3.19}$$

The empirical factor n_3 accounts for variation of thrust with flight Mach number, as shown in Table 3.5.

Table 3.5: Empirical factor n_3 as a function of flight Mach number [63].

M/M_{ref}	n_3
0.85	0.73
0.92	0.69
1.00	0.66
1.08	0.63
1.15	0.60

3.4.3. FUEL CONSUMPTION

The specific fuel consumption as a function of altitude and flight speed is estimated using Equation 3.20 [63]. In this equation θ is the ambient temperature ratio with respect to sea level temperature. The reference TSFC, temperature ratio and Mach number are the respective values in cruise conditions. For the reference TSFC a value of 13.5 g/kNs [1] is assumed, which corresponds to the A35K engine during cruise. The exponent n is an engine-specific value, which was determined to be 0.42 using Figure D.1 [63].

$$\text{TSFC} = \text{TSFC}_{\text{ref}} \sqrt{\frac{\theta}{\theta_{\text{ref}}}} \left(\frac{M}{M_{\text{ref}}} \right)^n \tag{3.20}$$

3.4.4. LIMITATIONS

The model by Bartel and Young describes the performance of two-shaft turbofan engines with a BPR of up to 9 and OPR up to 36. State-of-the art engines like Rolls Royce XWB -84 and -97 (which are installed on the Airbus A350-900 and -1000 respectively) usually have a three-shaft architecture. Furthermore, the BPR of both Trent engines are approximately 10 and have an OPR of approximately 50. The predictive qualities of the model for three-shaft turbofan engines and the effect of higher BPR and OPR values are not known. It is possible that overfitting of the data negatively impacts predictions outside the sampled range. However, since the model predicts thrust ratios for engines up to BPR 9 well and its equations are dependent on the BPR, it is deemed acceptable to use this model due to the limited availability of alternatives.

3.5. GROUND CONTACT

When the landing gear wheels make contact with the runway, a normal force perpendicular to the runway and a friction force parallel to the runway are exerted on the aircraft by the wheels. This section elaborates on the assumptions and logic that these contributions are based upon. The dynamics of the landing gear have been simplified, assuming a rigid landing gear. Also, the aircraft motion will be restricted to longitudinal motion with 3 DoFs. To calculate the ground contact forces and their resulting moments, the sum of all other external forces in the aircraft symmetry plane and their pitching moment contributions should be known. These external forces and moments will be referred to as the external forces and moments excluding ground contact (EGC), denoted as F_{EGC} and $\mathcal{M}_{\text{EGC}}$. For the EGC forces and pitching moment the different contributions are shown in Equation 3.21 and Equation 3.22, which include aerodynamic, propulsive and gravitational contributions. Note that the gravitational force does not cause a pitching moment about the CG. The EGC forces can be decomposed in an X and Z component. It is assumed that the y-axes of the b-frame and v-frame are aligned (see Figure 3.2). A free body diagram (FBD) of the longitudinal forces and moments during ground contact is shown in Figure 3.10. The subscripts ng and mg are used for the nose gear and landing gear, superscript v indicates forces and coordinates in the v-frame. Note that x and z denote coordinates with respect to the CG, while X and Z denote forces parallel to the x- and z axes of the indicated reference frame.

$$\sum F_{\text{EGC}} = F_{\text{aero}} + F_{\text{prop}} + F_{\text{g}} \tag{3.21}$$

$$\sum \mathcal{M}_{\text{EGC}} = \mathcal{M}_{\text{aero}} + \mathcal{M}_{\text{prop}} \tag{3.22}$$
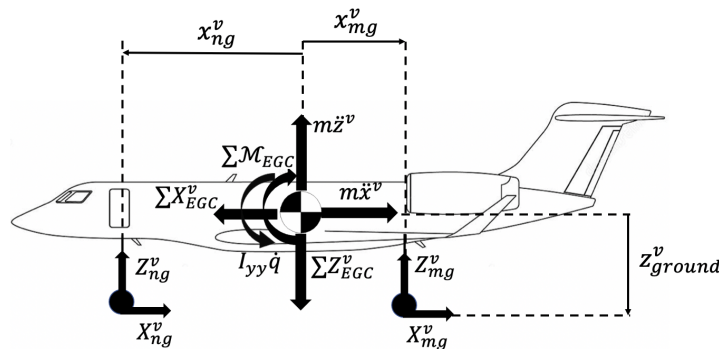
Figure 3.10: Free body diagram of longitudinal forces and moments during ground contact, including relevant moment arms.

Based on the FBD in Figure 3.10, a set of equations of motion that govern the longitudinal motion can be derived, using the CG as moment reference point. Note that the signs of the variables in Equation 3.23 - Equation 3.25 are consistent with the orientation of the v-frame axes, not the direction drawn in the FBD. This means that a positive x-coordinate indicates a position forward of the CG, a positive z-coordinate indicates a position below the CG, and positive X and Z forces point forward and downward, respectively. Ground contact forces are modelled to establish a vertical force equilibrium in the v-frame. The landing gear can only exert a Z^v force along the negative z^v axis, perpendicular to the runway. Therefore the signs of Z_{ng}^v and Z_{mg}^v can never be positive, as this would indicate a force pulling the aircraft towards the runway. Following the same reasoning, the signs of X_{ng}^v and X_{mg}^v can never be positive unless the engine would power the wheels.

$$X_{ng}^v + X_{mg}^v + \sum X_{EGC}^v = m\ddot{x}^v \tag{3.23}$$

$$Z_{ng}^v + Z_{mg}^v + \sum Z_{EGC}^v = m\ddot{z}^v \tag{3.24}$$

$$\left(X_{ng}^v + X_{mg}^v\right) z_{ground}^v + \sum \mathscr{M}_{EGC}^v = I_{yy}\dot{q} \tag{3.25}$$
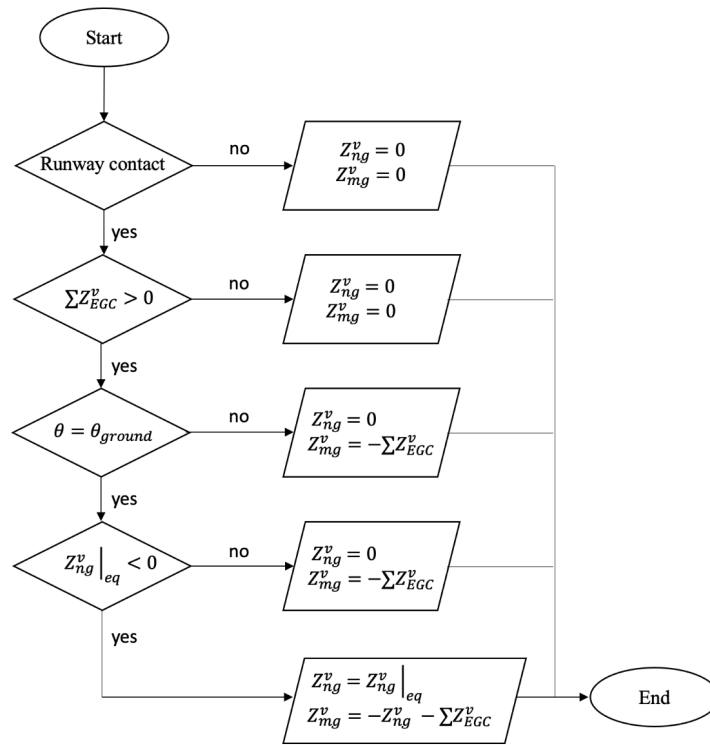
Figure 3.11: Gear load calculation strategy.

For the ground contact forces, the following assumptions are made.

- If $\sum Z_{EGC}^v$ is positive, then the normal forces of the nose and main gear will counteract $\sum Z_{EGC}^v$.

- If $Z_{EGC}^v \leq 0$, then $Z_{ng}^v = Z_{mg}^v = 0$.

- If θ is larger than θ_{ground}, no nose wheel contact force exists: $Z_{ng}^v = 0$.

- If the nose gear load required for static equilibrium, $Z_{ng}^v|_{eq}$, points into the runway, then $Z_{ng}^v = 0$.

- The runway friction force is proportional to the normal force and a constant friction coefficient μ.

- During ground contact, the landing gear wheels are able to counteract excess rolling moments, yawing moments and sideforces.

These assumptions are summarised in the flowchart in Figure 3.11, which is used to determine the loads on the nose gear and main gear. The friction forces of the nose and landing gear can be expressed in terms of their respective normal forces and friction coefficients.

$$X_{ng}^v = \mu_{ng} Z_{ng}^v \tag{3.26}$$

$$X_{mg}^v = \mu_{mg} Z_{mg}^v \tag{3.27}$$

Substitution of Equation 3.26 and Equation 3.27 into Equation 3.25 in combination with Equation 3.24 yields a system of two equations with two unknowns Z_{ng}^v and Z_{mg}^v that can be solved to determine the the required nose gear load for static equilibrium.

Having calculated both the main gear and nose gear loads, the pitching moment contribution due to ground contact forces (subscript GC) is calculated using Equation 3.28. The X- and Z-force contributions in v-frame are calculated using Equation 3.29 and Equation 3.30, respectively. These forces are transferred to the b-frame using the transformation matrix given in Equation 3.3.

$$\Delta \mathcal{M}_{GC} = -Z_{ng}^v (x_{ng}^v - \mu_{ng} z_{ground}^v) - Z_{mg}^v (x_{mg}^v - \mu_{mg} z_{ground}^v) \tag{3.28}$$

$$\Delta X_{GC}^v = Z_{ng}^v \mu_{ng} + Z_{mg}^v \mu_{mg} \tag{3.29}$$

$$\Delta Z_{GC}^v = Z_{ng}^v + Z_{mg}^v \tag{3.30}$$

Braking with the landing gear brakes is done by adjusting the friction coefficient of the main gear wheels μ_{mg}. The rolling friction coefficient is assumed to be 0.02 for a dry concrete runway [45]. When the brakes are applied, it is assumed that the braking coefficient μ_b is constant. For a dry runway, a braking coefficient of 0.4 is assumed. For wet runways and icy runways, the braking coefficient is assumed to be 0.3 and 0.1 respectively [32].

3.5.1. LIMITATIONS

Landing gear dynamics have a higher order of complexity than modelled in this research. Simplifications include the rigid tyres and shock dampers and the use of constant rolling and braking coefficients. The braking coefficient is actually a function of many factors, such as the tyre friction coefficient and available brake torque. Tyre temperature, tyre pressure and contact area, among other factors, also influence the braking coefficient. Therefore, determining the braking coefficient is a complex process that should be modelled in more detail. For the scope of this research it is deemed acceptable to use an average constant value, especially because the same approach is used for both aircraft. Therefore their braking performance can still be compared, but these limitations should be kept in mind when interpreting results.

3.6. PILOT AND FLIGHT CONTROL SYSTEM

The aircraft is controlled by modelling a pilot that provides control variable values that are converted to control surface deflections and a thrust setting by the Flight Control System (FCS). Control variables that the pilot can influence include δ_{roll}, δ_{pitch}, δ_{yaw} and $\delta_{throttle}$. These control variables correspond to stick and pedal inputs and the thrust setting and can assume values between -1 and 1. A positive roll, pitch or yaw control value corresponds to a positive moment around the respective body reference frame axes, as defined in Figure 3.2. For the throttle setting -1 is idle thrust, while 1 means full thrust. No thrust reversal is modelled.

Depending on the performed manoeuvre, the pilot attempts to provide control inputs that enable the aircraft to perform the manoeuvre as desired. This is done by incorporating different controllers that aim to minimise the error in prescribed variable values. In general, each controller has the same closed feedback loop architecture as shown in Figure 3.12. For each control loop, a target value is set for a specific parameter. This target value is compared to the current value and the error $e(t)$ is fed into a PID controller. PID controllers consist of three parts: a **P**roportional gain K_p, an **I**ntegral gain K_i and a **D**erivative gain K_d. These gains are multiplied by the current error, time-integrated error and current time derivative of the error, respectively. The output of the PID controller $u(t)$ is calculated by summing the proportional, integral and derivative contributions as shown in Equation 3.31.

$$u(t) = K_p e(t) + K_i \int_0^t e(\tau) \mathrm{d}\tau + K_d \frac{\mathrm{d}e(t)}{\mathrm{d}t} \tag{3.31}$$

In order to obtain the desired system behaviour, the control gains of the PID controller have to be tuned until the response is stable. The proportionality gain K_d can be increased to decrease the rise time of the system, allowing

the system to reach the target value more quickly. However, overshoot also increases if K_p is increased, which may be undesirable. The integral gain K_i can be used to decrease the steady state error. The derivative gain is used to dampen oscillations.
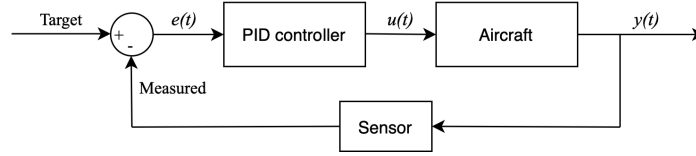
Figure 3.12: General architecture of closed feedback control loop.

Two human elements involving reaction time have been implemented in the pilot model. Also, a spool up/down time for the engines has been implemented. These values have been obtained from previous research and are shown in Table 3.6 [65]. It is assumed that spooling the engine up or down is linear with time.

Table 3.6: Time delays incorporated in FCS.

Description	Value in (s)
Brake deployment delay after engine failure	2.9
Spoiler deployment delay after engine failure	4.3
Engine cut delay after engine failure	3.3
Engine spool up/down time	5.0

How controllers like in Figure 3.12 are used to perform different manoeuvres is described in more detail in section 3.7.

3.7. Manoeuvres

This section elaborates on the procedures that are followed to perform the different manoeuvres investigated in this research. An overview of the different controllers used per manoeuvre is shown in Table 3.7. The controller is activated when all specified conditions are satisfied. The controller then tries to set the target parameter to the specified value by adjusting the specified control variable accordingly. In the following sections each manoeuvre will be discussed in more detail.

Table 3.7: Controller specifications for different manoeuvres.

Manoeuvre	Condition	Condition 2	Control variable	Target parameter	Value
Continued Takeoff	$V \geq V_R$	$\alpha + \Delta t \dot\alpha < \alpha_{ref}$	δ_{pitch}	q	q_{ref}
		$\alpha + \Delta t \dot\alpha \geq \alpha_{ref}$		α	α_{ref}
	OEI	$\theta > \theta_{ground}$	δ_{yaw}	$\sum \mathcal{N}_{EGC}$	0
Aborted Takeoff	$t \geq t_{EF} + \Delta t_{delaybrake}$		δ_{pitch}	N_{ng}/W	0.08
				θ	θ_{ground}
Landing	> 1m above runway		δ_{pitch}	γ	$\gamma_{ref, TD}$
	≤ 1m above runway			q	0
	Touchdown	$\theta > \theta_{ground}$	δ_{pitch}	q	q_{derot}
	Touchdown	$\theta = \theta_{ground}$	δ_{pitch}	N_{ng}/W	0.08
				θ	θ_{ground}

3.7.1. Continued Takeoff

Background information on takeoff definitions can be found in section 2.2.1. During takeoff the aircraft accelerates down the runway from standstill at maximum available thrust, initiates rotation at a speed V_R, lifts off at a speed V_{LOF} and climbs until the lowest point of the aircraft surpasses the screen height h_{screen}. As shown in Table 3.7 two controllers have been implemented for a takeoff with all engines operative. During the first part of the rotation phase, a reference pitch rate is targeted, until the sum of the pitch attitude and pitch rate multiplied by a time Δt surpasses the reference angle of attack. This Δt has been chosen to be 1 second to reduce the probability of overshooting the target AoA as this could result in a wing tip/tail strike. The value of 1 second was deemed

reasonable as it is not possible to immediately reduce the pitch rate to zero due to the existence of inertial forces. It has been chosen to target an AoA instead of a pitch attitude because on the runway the AoA and pitch attitude are equal to each other, while during the airborne phase and non-zero flight path angle the AoA is smaller than pitch attitude. For a quicker climb it is therefore chosen to maintain the target AoA, as targeting a pitch attitude would result in a lower AoA for positive climb gradients. As preliminary results have shown that higher reference AoAs shorten the takeoff distance significantly, the reference AoA is chosen to be close to the wing tip/tail strike attitude θ_{TS}. A margin of 0.5 deg has been taken into account: $\alpha_{ref} = \theta_{TS} - 0.5$ deg. The respective values of θ_{TS} can be found in Table 2.3.

In the event of a continued OEI takeoff, a third controller is activated as soon as the nose wheel loses contact with the ground. By applying a pedal input the pilot will attempt to neutralise the yawing moment due to thrust imbalance. The target is to reduce the yawing moment excluding ground contact forces $\sum \mathcal{N}_{EGC}$ to zero.

For the takeoff manoeuvre 2D equations of motion have been used, restricting the aircraft translational motion to the forward and upward directions and preventing the aircraft from rolling and yawing. This choice was made because flying steadily with OEI requires a nonzero sideslip and banking angle which is difficult to control with the simple PID controllers used in this research due to the coupled nature of yawing and rolling moments as a result of asymmetric control surface deflections. However, because the x- and z-components of the rudder forces are taken into account in the 2D EOMs, additional drag due to rudder deflection is still accounted for. It can be expected that the predicted takeoff distances for OEI will be slightly underestimated, as the airborne phase does not include sideslipping flight or a banking angle.

3.7.2. Aborted Takeoff

In the event of an aborted takeoff, the aircraft brakes to standstill on the runway. As described in section 3.6 human response times have been incorporated in the pilot model, which are presented in Table 3.6. As soon as the pilot applies the brakes at $t = t_{EF} + \Delta t_{delaybrake}$, the friction coefficient of the main gear is set to the braking coefficient μ_b. Also, two controllers are activated, shown in Table 3.7. The first controller aims to maximise downforce from the wing to maximise the main gear wheel load, while keeping at least 8% of the aircraft on the nose wheel to allow the pilots to steer the aircraft [32]. In Table 3.7 N_{ng} denotes the normal force on the nose gear wheel. The second controller is a back-up system in case the pitch attitude of the aircraft starts to deviate from the ground resting attitude θ_{ground}. At $t_{EF} + \Delta t_{delayengcut}$ the thrust setting is reduced to idle, while accounting for the spool-down time of the engine. Thrust is modelled to linearly reduce to zero over the course of the spool-down time after the thrust setting is set to idle. At $t_{EF} + \Delta t_{delayspoiler}$ the ground spoilers, described in Figure 3.2.1 are deflected, dumping lift, increasing the main gear load and increasing braking capabilities. The aircraft continues to decelerate down the runway until it comes to a full stop.

3.7.3. Landing

Definitions and regulations of the landing manoeuvre are described in 2.2.1. The landing manoeuvre commences when the lowest part of the aircraft reaches the screen height upon descent, which is specified in section 2.2.1. It is assumed that the aircraft arrives at the screen height following a standard glideslope with a flight path angle of -3 degrees. Using the lift polars from Figure 3.3, the maximum AoA from subsection 3.2.5, the maximum landing weight from Table 2.2 and the air density at sea level, the stall reference speed in landing configuration and corresponding approach speed were calculated.

In order to prevent excessive loads on the landing gear during touchdown, a flaring manoeuvre is performed to reduce the descent rate of the aircraft. If no flaring would be performed, touchdown would occur at a rate of approximately 12 ft/s. In order to place this figure in perspective it should be realised that according to CS25 the maximum descent rate at MLW is 10 ft/s, while the maximum descent rate at MTOW is 6 ft/s [43]. Generally, 6 ft/s is considered to be a firm touchdown, but nothing out of the ordinary. Therefore in this research, a descent rate of 6 ft/s is targeted at touchdown. At the calculated approach speeds, this corresponds to $\gamma_{TD} \approx -1.4$ degrees. The pilot should increase the flight path angle by approximately 1.6 degrees during the flaring manoeuvre by pulling up the nose. Table 3.7 shows that while the aircraft is more than 1m above the runway, the pilot attempts to increase the flight path angle to the reference touchdown value. In order to achieve this, the nose is raised to increase lift. To prevent the aircraft from over-rotating the nose-up rotation is stopped when the aircraft descends below 1m above the runway. Meanwhile, during the flaring manoeuvre, thrust is reduced to idle while taking the spool-down time into account. After touching down, derotation is initiated. Preferably this should be done quickly, as braking can only start once the nose wheel is on the runway. During derotation, a target pitch rate of -3 degrees per second is maintained. Once derotation is complete and the nose wheel touches the runway, braking is initiated by deflecting the ground spoilers, setting the main gear friction coefficient to μ_b and activating the

same controller used to brake during an aborted takeoff. As explained above this controller maximises downforce while keeping at least 8% of the aircraft weight on the nose wheel. Like for the takeoff manoeuvre, landing is simulated using 2D equations of motion as only symmetric motion is considered.

3.7.4. Flight

To investigate the performance characteristics during the flight phase, the 3D equations of motion are used to trim the aircraft in different flight conditions. One Engine Inoperative, sideslipping and banked flight are also considered. The landing gear is assumed to be retracted and therefore the force and moment contributions from the landing gear are zero. The aircraft is trimmed using the procedure described in section 3.1, minimising the objective function of Equation 3.6 at different altitudes, air speeds, weights and center of gravity positions.

4

VERIFICATION AND VALIDATION

Trusting the results of flight mechanics simulations is always a leap of faith,
since complete validation is basically impossible.
– C. Varriale [56]

The flight mechanics model used in this research consists of different sub-models, each with its own model uncertainties. The quote above fittingly summarises the verification and validation process of flight mechanics simulations. Nevertheless, this chapter describes the attempt to verify and validate the flight mechanics model and its integrated parts as well as possible.

4.1. SUBMODEL VERIFICATION

Verification is a quality control process that evaluates whether a system complies with imposed conditions and specifications [66]. Verifying the correct working of the different sub-models increases confidence in the accuracy of the flight mechanics model. In this section, verification of the aerodynamic, inertia and propulsion models will be briefly discussed, followed by a verification that the flight mechanics model is able to simulate the intended manoeuvres correctly.

4.1.1. AERODYNAMICS

The aerodynamic data used in this research is generated by Odilila, a VLM developed and verified by Airbus. Verification of the predictive qualities of Odilila for lift curve slopes and induced drag has been performed in previous research [36, 37] and can be found in Appendix E. The zero-lift drag calculations and wave drag estimates are based on empirical relations and are therefore inherently validated for the sampled data range. Although none of the sampled aircraft are flying wings, the aspect ratio and sweep angle of the FVK fall within the sample ranges.

4.1.2. INERTIA

The moments of inertia used in this research were adapted from values obtained in previous research [37], which carried out a verification of the used method. This was done by comparing the computed moments of inertia around the body principal axes, I_{xx}, I_{yy} and I_{zz} with values found in literature for other aircraft. It was found that a quadratic relation exists between the moments of inertia around each axis and a characteristic length. I_{xx} was found to scale with the wing span squared, I_{yy} with the aircraft length squared, and I_{zz} with the sum of squares of aircraft length and height. The latter two relations are displayed in Figure C.1. The computed I_{yy} and I_{zz} were found to match these quadratic relations well and are therefore considered verified. I_{xx} was found to be under-predicted. However, since in this research mostly symmetric motion is studied during takeoff and landing, an aberration in the I_{xx} value is of little significance to the outcomes of this research. The only situation where I_{xx} is important is when the aircraft is trimmed in OEI to investigate the OEI climbing performance. Since the aircraft in trimmed condition is not supposed to oscillate, it is assumed that the trim state can still be found with a slightly inaccurate I_{xx}.

4.1.3. Propulsion

The Bartel-Young thrust lapse model [63] is based on empirical data and has shown to predict thrust within 1% of the available data for Mach numbers smaller than 0.4 and within 4% during climb. The takeoff and climb thrust models have been merged using the assumption that the maximum continuous thrust is 85% of the maximum available thrust, based on engine performance curves [64]. The correctness of this figure is confirmed by the available engine data of the Rolls Royce Trent XWB -84 and -97 engines, which are installed on the Airbus A350 -900 and -1000 respectively. For these engines the maximum continuous thrust is 84.8% and 85.5% of the maximum available thrust [41]. Although the BPR and OPR of the FVK and A35K engines are greater than for the sampled engines, the model accounts for BPR variations. Although it is possible that the engine data is over-fitted, the opposite may also be true and the availability of alternatives that do not require extensive modelling is limited.

4.2. Flight Mechanics Model Verification

In order to verify the flight mechanics model, a number of manoeuvres will be presented in this section to show that they are performed as described in section 3.7.

4.2.1. Takeoff

In this section, three different takeoff manoeuvres are verified: a nominal takeoff, a takeoff with one engine inoperative, and an aborted takeoff. Figure 4.1 shows the angle of attack, pitch rate and flight path angle during a takeoff of the FVK. The angle of attack starts at -3 degrees, which is the ground attitude. After rotation is initiated, the pitch rate quickly assumes the target value of 5 deg/s. When the AoA gets close to the target AoA, the pitch rate is decreased in order to prevent overshoot. After liftoff, when the flight path angle is larger than zero, the target AoA is still maintained until the takeoff manoeuvre is completed at the screen height.
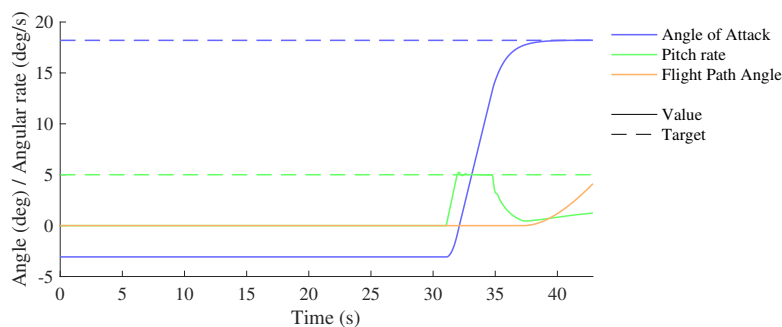
Figure 4.1: Time history of AoA, pitch rate and flight path angle during a FVK takeoff.

Figure 4.2 shows the yawing moment excluding ground contact (EGC) forces and the yaw control parameter (rudder input) during a OEI takeoff simulation. In this case, the right-side engine has failed, which causes a positive yawing moment imbalance. This simulation starts at the moment that rotation is initiated and therefore the nose gear wheel loses contact with the ground. The pilot attempts to balance the yawing moment using the rudders to ensure that balance is restored at liftoff. Figure 4.2 shows that the pilot gradually increases the rudder-left input, which decreases the yawing moment excluding ground contact forces to zero.

Figure 4.3 shows the nose gear load, thrust and deceleration during an aborted takeoff. The simulation starts at the instant that an engine failure occurs. During braking, it is attempted to keep at least 8% of the aircraft weight on the nose wheel to allow the pilots to steer. This target is shown by the dashed line in the top figure. It can be seen that the target is closely followed except for two peaks in the nose gear load, which are caused by applying the brakes and deflecting spoilers, respectively. Also, the nose gear load increases after a certain point in time as the dynamic pressure decreases and the balance shifts towards the balance at standstill. As explained in section 3.6, three human response delays and a spool-down time are implemented, which can be seen in Figure 4.3. 2.9 seconds after engine failure occurs, the brakes are applied. This is shown by the peak in nose gear load in the top graph and an increase in deceleration in the bottom graph. 4.3 seconds after engine failure, the pilot also deflects the spoilers to increase the load on the main gear wheels. This also momentarily increases the nose gear load, which causes the second peak in the top graph. The deceleration rate also increases as the spoilers are deflected, as shown in the bottom graph. 3.3 seconds after engine failure, the pilot reduces the thrust setting to idle. However, due to the 5.0 second spool-down time, thrust does not immediately decrease to zero. Instead,

the thrust decrease is modelled as a linear decrease, as shown in the middle graph. All procedures as defined in section 3.7 are executed as desired. Therefore the flight mechanics model is deemed verified to perform a nominal takeoff, OEI takeoff and aborted takeoff manoeuvre.
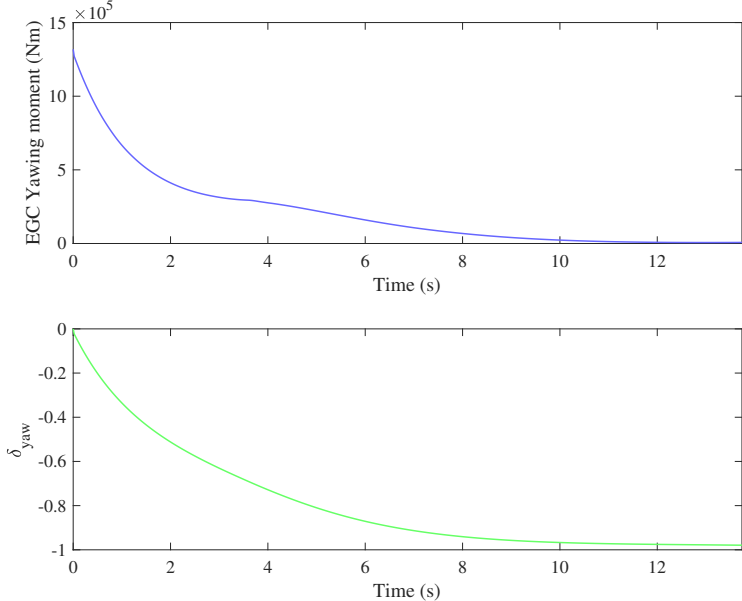
Figure 4.2: Time history of the yawing moment excluding ground contact forces and rudder input during takeoff with OEI.
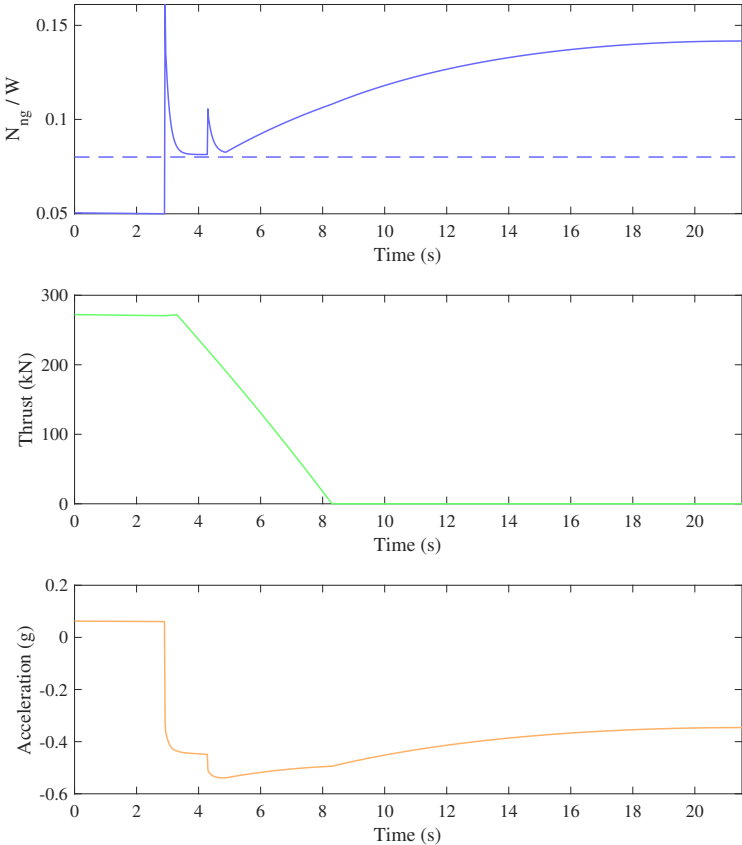
Figure 4.3: Time history of the nose gear load, thrust and deceleration during an aborted takeoff.

4.2.2. LANDING

During the landing flare the nose is pulled up to decrease the aircraft descent rate to, 6 ft/s. In Figure 4.4, this value is represented by a target flight path angle. It can be seen that at touchdown, the flight path angle instantly decreases from the target touchdown value to zero. To prevent the aircraft from over-rotating on the runway, the pitch rate is decreased to zero just before touchdown. After touchdown, a target derotation rate of -3 deg/s is maintained until the nose wheel touches the ground. After derotation the aircraft continues down the runway at the ground pitch attitude, which is -3 degrees in the case of the Flying-V.

Figure 4.5 shows the nose gear load, altitude and deceleration of the aircraft. By comparing Figure 4.4 and Figure 4.5 the touchdown instant can be confirmed with the altitude chart. It can be seen that the nose gear load is zero until derotation is complete. Braking is immediately initiated as soon as the nose gear makes contact with the ground. Contrary to the case of an aborted takeoff, no pilot response delays are implemented as the pilots have time to anticipate the nose gear contact. Hence, both spoiler deflection and wheel brake deployment occurs at the same time instant, which is shown in the deceleration curve.

All procedures as defined in section 3.7 are executed as desired. Therefore the flight mechanics model is deemed verified to perform landing manoeuvres correctly.
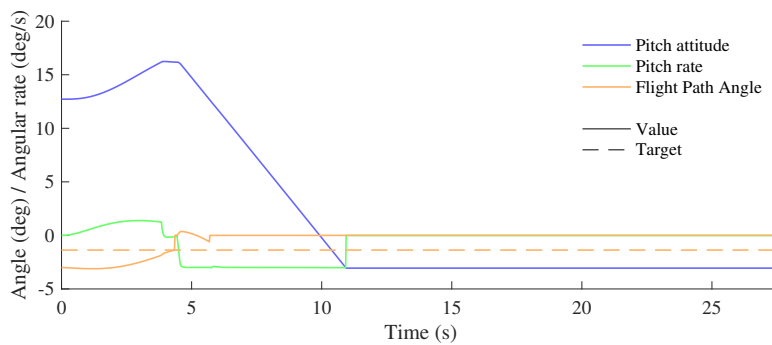
Figure 4.4: Time history of pitch attitude, pitch rate and flight path angle during landing.
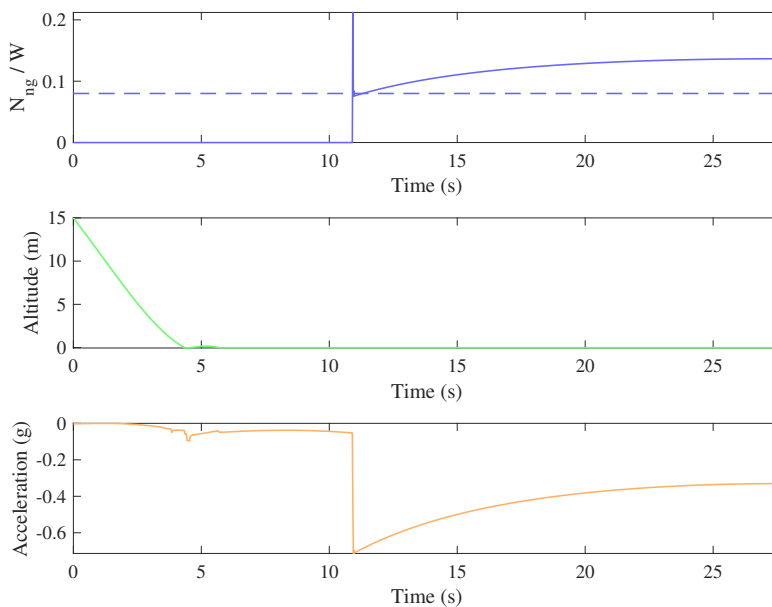
Figure 4.5: Time history of the nose gear load, altitude and deceleration during landing.

4.2.3. ONE ENGINE INOPERATIVE CLIMB

To verify the trimming function, the Flying-V-1000 is trimmed at maximum thrust with the right-side engine inoperative at MTOM, an altitude of 100 m and a velocity of 100 m/s. In this situation the thrust imbalance results in a positive yawing moment imbalance. The resulting trim state properties are shown in Table 4.1. Note

that the control variables δ_{roll}, δ_{pitch} and δ_{yaw} can range from -1 to 1. It can be seen that the the trim function has eliminated sideslip by slightly banking towards the operative engine and applying a roll-left and rudder-left command. All these actions are expected based on pilot handbook instructions for One Engine Inoperative flight [67]. Hence, the trimming algorithm is assumed to perform as intended.

Table 4.1: Trimmed aircraft parameters with right-side engine inoperative.

Parameter	Value	Unit
Sideslip angle	0	deg
Bank angle	-1.13	deg
Heading angle	-0.22	deg
δ_{roll}	-0.07	-
δ_{pitch}	-0.39	-
δ_{yaw}	-0.45	-

4.3. VALIDATION

Validation is a quality assurance process of establishing evidence that confirms that a system accomplished its intended use requirements [66]. Limited means are available to validate the correct working of the flight mechanics model. Three figures will be compared to publicly available data of the Airbus A350-1000 to validate the flight mechanics model: the absolute service ceiling, takeoff runway length, and landing field length.

4.3.1. SERVICE CEILING

From A35K type certification documents [68] the maximum operating altitude of the A35K can be found to be 41,450 ft, or 12.6 km. From EASA CS25 regulations [43], it is not entirely clear which weight and CG position are supposed to be chosen to determine the maximum operating altitude. Hence, the MTOM and most foward CG position are used to determine the absolute service ceiling of the A35K. With these inputs, the A35K was found to be able to sustain trimmed level flight at maximum available thrust up to 12.0 km, which is close to the absolute service ceiling defined in the type-certificate sheet.

4.3.2. LANDING FIELD LENGTH

The other source of validation information is the Airbus A350 Aircraft Characteristics Airport and Maintenance Planning (ACAP) [40] document. Two charts provide an indication of the runway length during takeoff and the landing field length at different aircraft weights. According to Federal Aviation Regulations, the landing field length is calculated by dividing the measured landing distance by a factor 0.6 for safety measures. In this research landing manoeuvres have been performed at MLW at sea level. According to the provided chart, the A335K has a landing field length of approximately 2113m at sea level and MLW. In this research, the landing field lengths found for the same conditions were ranging from 2112 m to 2153 m, depending on the CG location, which is close to the value provided by Airbus.

4.3.3. TAKEOFF RUNWAY LENGTH

The last validation figure is the runway length during takeoff. It is assumed Airbus used the same takeoff runway length definition distance as the definition specified in CS25, which is equal to 115% of the measured takeoff distance from standstill to the screen height. A comparison between the runway length defined by Airbus and the obtained results of this research is shown in Figure 4.6. As can be seen, the runway length is accurately predicted for the tested aircraft mass values at sea level and 2000 ft. At 4000 ft the calculated runway length starts to deviate from the Airbus data. Also, the Airbus data shows a kink in the takeoff runway length at 4000 ft for a mass equal to 92% of the MTOM, which was not expected. Since it is uncertain how exactly the Airbus values have been obtained, the match between results obtained by the present research and Airbus values is deemed satisfactory.
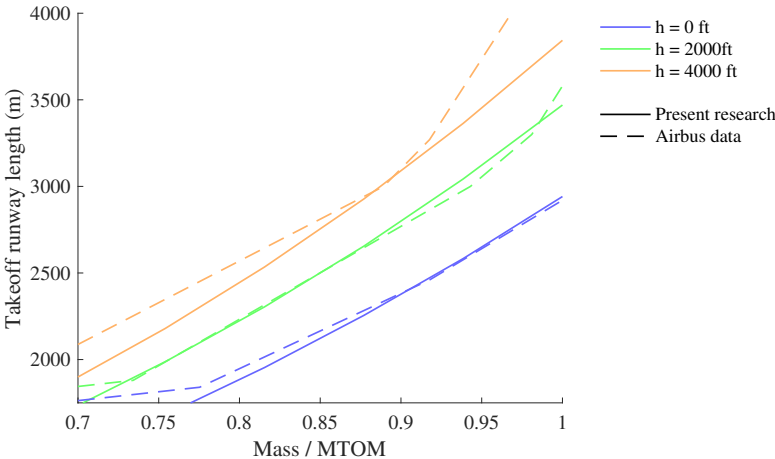
Figure 4.6: Airbus data and simulated runway length comparison.

5

RESULTS AND DISCUSSION

This chapter presents the results of calculated aircraft properties, the different simulations performed in this research and a reflection.

The estimated zero-lift drag coefficients of each aircraft component during takeoff, landing and cruise are presented in Table 5.1. Note that these values are coefficients normalised with respect to the reference area of the aircraft. As presented in Table 2.3, the reference areas of the FVK and A35K are 883 and 462 m^2, respectively. Part of the large difference in drag counts can be explained by the difference in reference area. Nevertheless, the FVK has an estimated 11%, 31% and 89% lower zero-lift drag during cruise, takeoff and landing, respectively. During takeoff and landing, this difference is largely due to flap drag. In low speed conditions the zero-lift drag contribution is a smaller portion of the total drag than in cruise conditions.

The three-dimensional drag divergence Mach number M_{3dd} and its components are shown in Table 5.2. The Flying-V has a smaller two-dimensional drag divergence Mach number M_{2dd} due to its larger thickness-to-chord ratio t/c. Due to the benefits of a large sweep angle and a small aspect ratio, M_{3dd} is substantially larger for the Flying-V than for the reference aircraft. However, due to the larger average t/c of the FVK, both aircraft still experience a similar amount of wave drag at the cruise Mach number, as can be concluded by looking at Figure B.4. Nevertheless, the difference in M_{3dd} results in a diverging wave drag difference between the two aircraft for Mach numbers higher than the cruise Mach number. It can be questioned whether the actual drag divergence Mach number of the FVK is as large as presented in Table 5.2, as the inboard wing does not feature super-critical airfoils. Also, shock formation at the junction between the inboard and outboard wing could reduce the drag divergence number. On the other hand, the FVK features a very good cross-sectional area distribution, which is beneficial for the drag divergence Mach number.

The moments of inertia that have been estimated using the method described in section 3.3 are presented in Table 5.3. As expected, the FVK has a larger I_{xx} than the A35K, as the absence of a fuselage results in a mass distribution further away from the x-axis. Due to its shorter length, the FVK features a smaller I_{yy} than the A35K, which is also reflected in the I_{zz} value. Especially the values of I_{yy} are of interest to this research, and it can be seen that for the FVK a considerably smaller torque is required to initiate a rotation about the y-axis than for the A35K.

Table 5.1: Estimated component zero-lift drag coefficients in counts during takeoff, landing and cruise.

Component C_{D_0} (cts)	Flying-V-1000			Airbus A350-1000		
	Takeoff	Landing	Cruise	Takeoff	Landing	Cruise
Fuselage	-	-	-	48.9	50.5	46.1
Wings	62.9	64.0	61.2	94.9	99.6	89.4
Nacelles	6.5	6.6	6.3	14.2	14.9	13.4
Pylons	3.5	3.5	3.4	5.3	5.5	5.0
Leakage	4.4	4.4	4.4	8.0	8.0	8.0
Flaps	-	-	-	68.5	205.4	-
Landing gear	50.5	50.5	-	80.0	80.0	-
Total	127.8	129.0	75.3	319.8	463.9	161.9

Table 5.2: Drag divergence Mach number comparison.

Item	Flying-V-1000	Airbus A350-1000
M_{dd2d}	0.791	0.810
$\Delta M_{\Lambda_{c/4}}$	0.140	0.042
ΔM_{AR}	0.030	0.015
M_{dd3d}	0.961	0.867

Table 5.3: Moments of inertia around the aircraft body principal axes at maximum takeoff weight and empty weight for the FVK and A35K.

Moment of Inertia (10^7 kg m^2)	Flying-V-1000		Airbus A350-1000	
	MTOM	Empty	MTOM	Empty
I_{xx}	3.96	1.23	3.18	0.94
I_{yy}	2.76	1.05	5.09	2.82
I_{zz}	6.58	2.14	8.64	3.75

5.1. TAKEOFF PERFORMANCE

To answer the research questions presented in chapter 1 regarding evaluation of the takeoff performance, takeoff simulations have been performed to evaluate and compare the takeoff distance, reference speeds and balanced field length.

5.1.1. TAKEOFF DISTANCE & REFERENCE SPEEDS

The takeoff distance is defined by CS25.113 as 115% of the horizontal distance travelled between standstill and clearing the screen height during an All Engines Operative takeoff [43]. The takeoff distances of the FVK and A35K are compared in Figure 5.1 for different takeoff masses and runway altitudes. For these simulations the CG has been placed at the forward-limit location, as this yields the longest takeoff distance, which will be discussed later in this chapter. At all altitudes and takeoff masses the FVK requires a shorter takeoff distance than the A35K. On average, the takeoff distance of the A35K for the same mass-to-MTOM fraction is 25% longer than for the FVK. This relative difference increases with increasing mass and altitude. It can be seen that for both aircraft the takeoff distance increase due to increasing mass is greater than it would be if these properties would be linearly related. This is because a larger mass does not only require more lift for liftoff, but also requires a larger elevator force to rotate the aircraft nose-up, increasing the liftoff speed.

Figure 5.1 also presents the optimal rotation velocity V_R for both aircraft. The optimal V_R is defined as the value that minimises the takeoff distance. The optimal V_R is significantly lower for the FVK than for the A35K for all simulated altitudes and mass fractions. The absolute optimal V_R difference between both aircraft increases with increasing mass, but seems to be relatively constant for varying altitude. However, it must be noted that the same absolute velocity difference means an increasing difference in dynamic pressure as the absolute value of the rotation speed itself increases. This could be the reason why the difference in optimal rotation speed does not increase with increasing takeoff mass. A small part of the reason why the FVK has a lower optimal rotation speed is that its takeoff attitude is larger due to its larger tailstrike attitude. Therefore, at the same pitch rate, rotation needs to be initiated earlier as the rotation phase takes more time to complete. However, as will be discussed later in this chapter, this is not the main cause for the obtained differences in optimal rotation speed.

The optimal rotation speed is determined using the same method for every mass-altitude combination. First, the takeoff distance is calculated for a number of rotation speeds separated by a 5 m/s spacing. From this initial evaluation, the 10 m/s V_R range where the optimum is located is determined. Within this range the takeoff distance is evaluated again at five different rotation speeds and the search range is refocused around the rotation speed with the minimum takeoff distance. This process is repeated until the optimal rotation speed is determined within 0.5 m/s of the optimum. This accuracy value is chosen based on the left-hand chart of Figure 5.2, which shows the influence of deviation from the optimal rotation speed, denoted ΔV_R, on the takeoff distance. It can be concluded that the takeoff distance is increasingly sensitive to the selected rotation speed as the distance to the optimum increases. Rotating too early results in additional drag due to an unnecessarily large pitch attitude while travelling down the runway at speeds too low for liftoff. Moreover, lifting off at an airspeed below the optimum can extend the airborne distance significantly. Rotating too late results in an unnecessarily large ground run distance. Finding the optimal rotation speed is therefore a trade-off between ground run distance and airborne distance. Figure 5.2 shows that if V_R is selected within 1 m/s of the optimum, the additional takeoff distance

is less than 5 m with respect to the optimum. Therefore, looking at the magnitude of the takeoff distance, a V_R accuracy of 0.5 m/s with respect to the optimum was deemed an acceptable margin. These optimal rotation speeds have been used to perform the takeoff manoeuvres presented in this section.
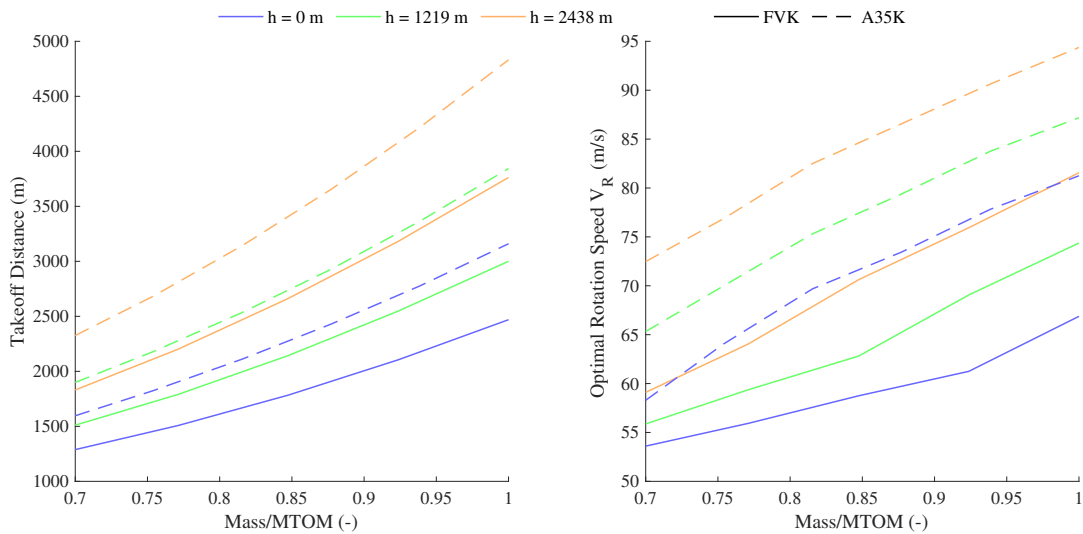
Figure 5.1: Takeoff distance and optimal rotation speed for minimum takeoff distance comparison between the FVK and the A35K.
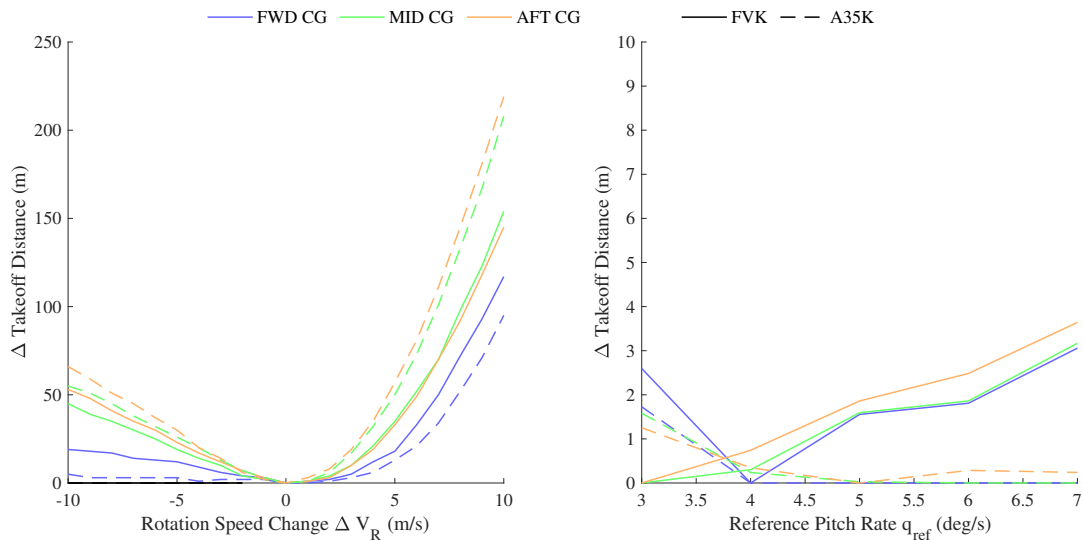
Figure 5.2: Influence of rotation speed deviation from the optimum and reference pitch rate on the takeoff distance.

The right-hand chart of Figure 5.2 shows the influence of the selected reference pitch rate on the takeoff distance. Once again, the rotation speed has been optimised for all cases. It can be concluded that if the optimal rotation speed is selected, the reference pitch rate has almost no influence on the takeoff distance. It must be noted that the reference pitch attitude is not necessarily achieved during rotation, but is merely a target. It can be seen that selecting a larger pitch attitude than 4 deg/s actually causes a slightly larger takeoff distance for the FVK. This is probably due to the formulation of the activation conditions of the takeoff controller, shown in Table 3.7. Due to the second activation condition of the α controller for continued takeoff, the α controller is activated at a lower pitch attitude if a larger pitch rate is attained to prevent overshoot. During the second part of the rotation phase, the AoA is cautiously increased towards the reference value. As this second phase is initiated earlier when a higher pitch rate is attained during the first part of the rotation, this leads to an extension of the duration of the second part of the rotation. It seems that the benefits of a shorter first phase and drawbacks of a longer second phase cancel each other out. Also, the conclusion that the reference pitch rate has little influence on the takeoff distance

seems to be a result of the formulation of activation conditions of the control system during takeoff. Possibly, the takeoff performance could be improved through selection of a larger reference pitch rate if the second rotation phase would be activated based on an absolute difference between the current pitch attitude and a reference pitch attitude.

The minimum unstick speed V_{MU} is the lowest speed at which an aircraft can lift off the runway and attain a positive steady climb gradient, which plays an important role in the takeoff performance of an aircraft. The left-hand chart of Figure 5.3 shows a comparison between the minimum unstick speed of the FVK and A35K with the CG located at the forward limit. Comparing this chart to the optimal rotation speeds in Figure 5.1, it can be concluded that the differences in optimal rotation speed between both aircraft are almost entirely caused by the minimum unstick speed differences. The large difference in the V_{MU} of both aircraft is not surprising. The FVK has a 9.2 larger tailstrike pitch attitude θ_{TS}, as shown in Table 2.3, allowing a much larger AoA at liftoff. Looking at Figure 3.3 and taking the different reference areas of both aircraft into account, it can be seen, that the additional lift generated per unit angle of attack is smaller for the FVK than for the A35K, but not by much. Therefore, the much larger attainable pitch attitude on the runway of the FVK results in a much larger attainable lift at the same airspeed. On top of that, the MTOM of the FVK is 18% smaller than for the A35K. As a result, the minimum unstick speed of the FVK is significantly lower than for the A35K, resulting in a lower optimal rotation speed and a shorter takeoff distance.

The right-hand chart of Figure 5.3 presents a somewhat more abstract concept that requires some additional explanation. On the vertical axis, the unconstrained minimum unstick attitude θ_{MU} is compared to the tailstrike attitude θ_{TS}. While in practice θ_{MU} can never exceed θ_{TS} on the runway due to geometric constraints, this chart shows at which attitude the aircraft would achieve its minimum unstick speed if the geometric constraint imposed by a tailstrike would be removed. Hence, if θ_{MU} is larger than θ_{TS}, the aircraft would rotate to a pitch attitude larger than the tailstrike attitude to attain a higher lift coefficient and unstick at a lower airspeed. Therefore, this chart shows whether the minimum unstick speed is governed by the elevator effectiveness or the geometry constraints of the aircraft. It can be concluded for both aircraft that V_{MU} is generally determined by geometric limitations, rather than control surface limitations. As these results have been obtained using the most forward CG location, it can be expected that for for all other CG locations the aircraft geometry governs the minimum unstick speed as well.
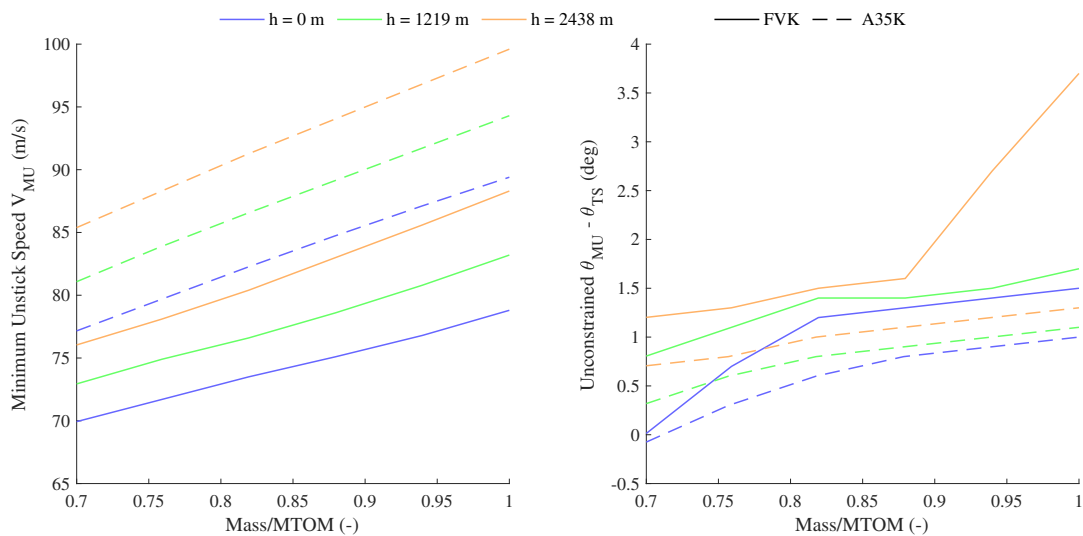
Figure 5.3: Minimum unstick speed comparison and unconstrained unstick attitude relative to tail strike attitude.

Figure 5.4 compares the distances travelled during different phases of the takeoff manoeuvre by the FVK (left) and A35K (right) for different CG positions. Figure 5.5 quantifies the distance difference per phase of the FVK with respect to the A35K. For both aircraft, the total takeoff distance decreases as the CG shifts rearwards, mainly due to a decrease in rotation distance. The FVK features a larger decrease in takeoff distance over the entire CG range. Figure 5.5 shows that the pre-rotation phase is almost single-handedly responsible for the difference in takeoff distance between the two aircraft. This difference increases as the CG shifts rearwards, indicating that the CG position has a larger influence on the optimal V_R for the FVK than for the A35K. As the CG range of the FVK is closer to the streamwise location of the main landing gear, this result could be expected. With the CG at

the most rearward position, the FVK CG has a shorter moment arm with respect to the main gear wheels than the A35K, making it easier to rotate the nose of the aircraft upward. In this situation, very little downforce has to be generated by the FVK trailing edge devices to rotate the aircraft, resulting in a higher net lift, which reduces the V_{MU} and optimal V_R.

Figure 5.11 also shows that the airborne phase of the FVK is shorter for all CG positions. This is due to a lower liftoff speed and a larger climb gradient for the FVK. As the CG position shifts rearwards the FVK loses its advantage with respect to the A35K during the rotation phase. It seems that part of the pre-rotation distance advantage gained with respect to the A35K is lost in the rotation phase. Looking at Figure 5.4 this seems mainly due to the rotation distance decrease of the A35K.
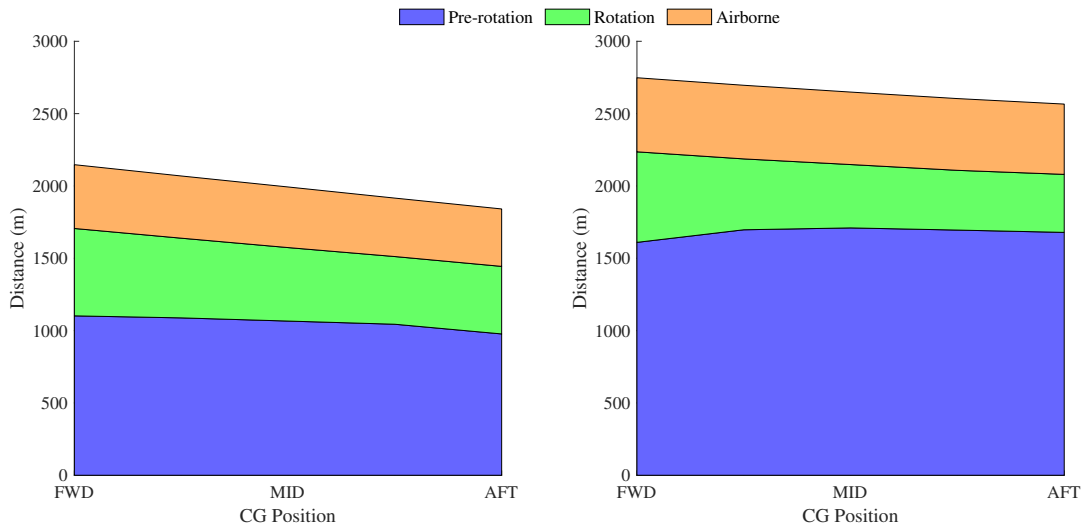
Figure 5.4: Horizontal distance comparison of the FVK (left) and A35K (right) during different takeoff phases for varying CG positions at sea level and maximum takeoff mass.
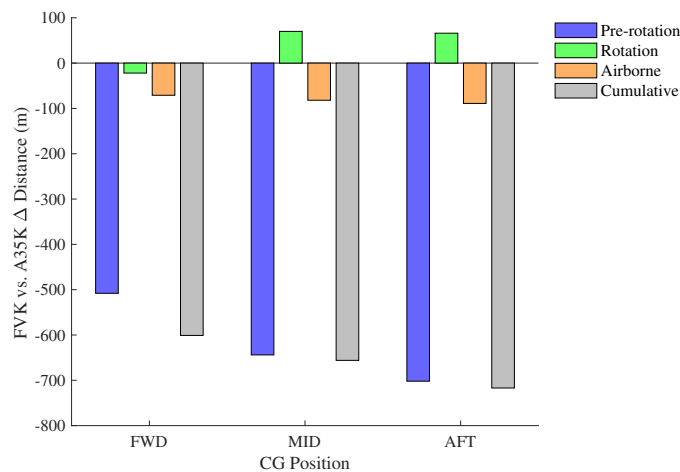
Figure 5.5: Comparison of takeoff distance differences between the FVK and A35K per phase.

5.1.2. BALANCED FIELD LENGTH

The concept of the Balanced Field Length (BFL) and corresponding reference speeds are described in section 2.2.1. Figure 5.6 compares the BFL distances of the FVK (left) and A35K (right) for different takeoff masses. The CG has been placed at the forward limit and the runway is located at sea level. Note that the distances shown are for a continued takeoff. For an aborted takeoff the distance travelled from standstill to the continue/abort decision moment is the same as for a continued takeoff. By definition, the braking distance of an aborted takeoff is equal to the sum of the ground run distance covered between the decision moment and liftoff and the airborne distance of the continued takeoff. Hence the braking distance can be derived from Figure 5.6 by summing the

green and orange distances. The FVK has a significantly shorter BFL than the A35K. Every phase of the FVK BFL requires a shorter distance than for the A35K, as shown in Figure 5.7 for different CG positions at MTOM. For increasing takeoff mass, the differences in BFL distances between the two aircraft increases. Especially the distance covered until V_1 is reached increases significantly for increasing takeoff mass.

Figure 5.7 shows that shifting the CG has little effect on the braking distance difference between the FVK and A35K, while the distance to V_1 decreases. Hence, the overall BFL difference between the two aircraft decreases as the CG shifts rearwards. At the same time the difference in the distance covered between the decision to continue and liftoff increases, while the airborne distance difference decreases.

Figure 5.8 shows a comparison between the decision speed V_1, takeoff safety speed V_2 and engine failure speed V_{EF}. Note that these velocities are calculated without any constraints on the available runway length. The reference speeds of the FVK are considerably lower than for the A35K, as could be expected from the BFL distance differences presented in Figure 5.6. Note that the higher decision and engine failure speeds of the A35K do not mean that the pilot can decide to abort takeoff later in a real situation. These velocities merely mean that the accelerate-go and accelerate-stop distances of the A35K are equal to each other for a higher decision speed, which corresponds to an engine failure at a higher velocity as well. The larger V_1 of the A35K results in a snowball effect on the BFL: a larger horizontal is covered while accelerating to V_1, which requires a longer braking distance to standstill for equal braking performance. Also, the larger airspeed at liftoff increases the horizontal airborne distance. The difference in BFL reference velocities between both aircraft can be directly related to the difference in minimum unstick speed shown in Figure 5.3.
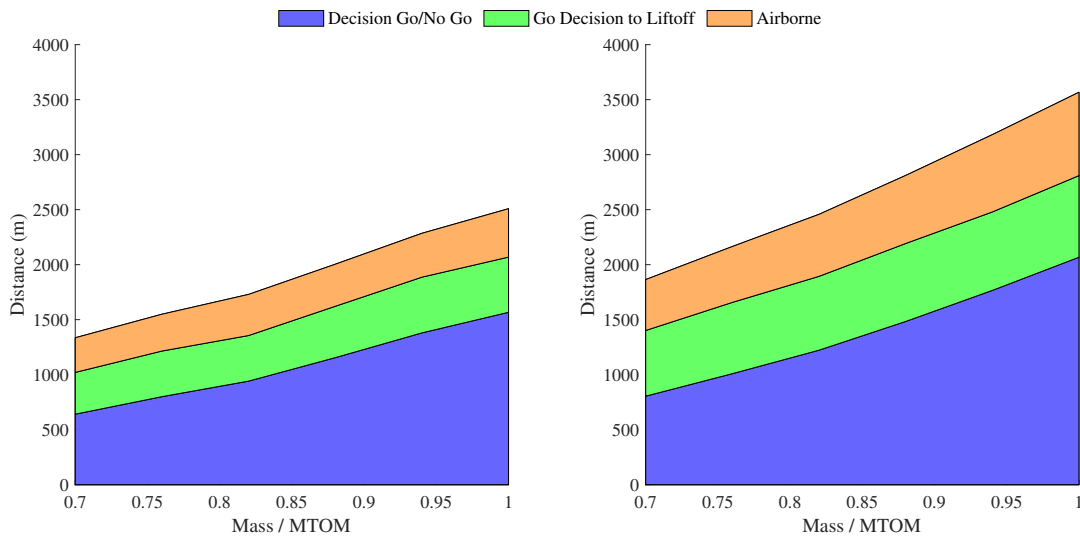
Figure 5.6: BFL distance comparison of the FVK (left) and A35K (right) for varying mass with the CG at the forward limit at sea level.
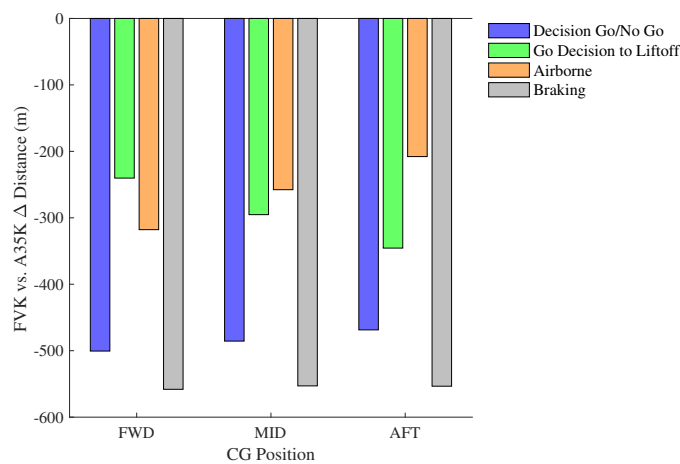
Figure 5.7: Comparison of BFL distance differences between the FVK and A35K per phase at MTOM.
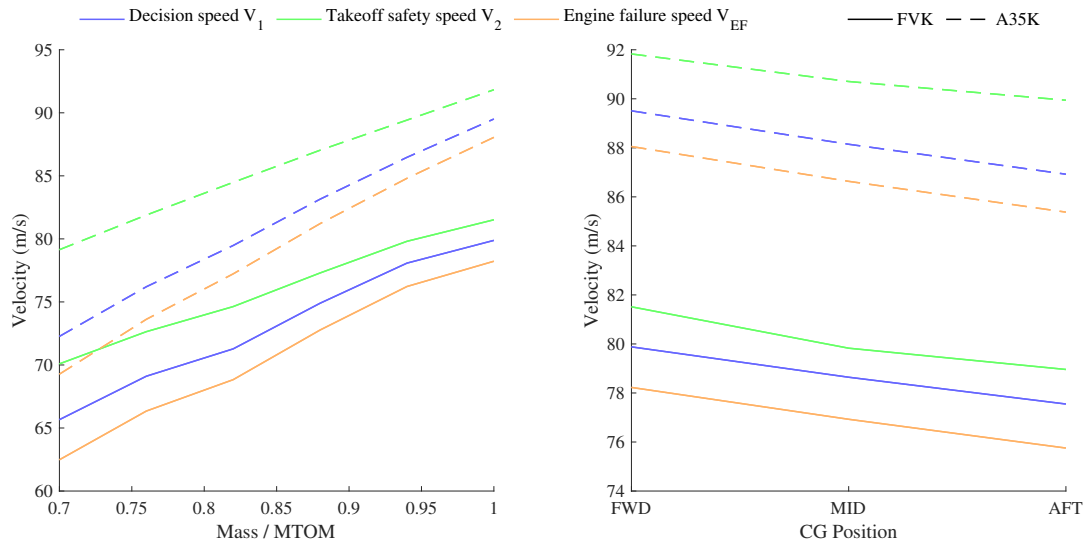
Figure 5.8: Comparison of BFL reference velocities as a function of takeoff mass and CG position.

Another reason why the Flying-V has favourable BFL characteristics compared to its competitor is the location where the engine is installed. Due to the over-the-wing position of the engine of the FVK, an engine failure will produce a pitch-up moment contribution with respect to the all-engines-operative situation. Therefore it becomes easier to rotate the nose of the aircraft upward with OEI, contrary to the A35K with its engines installed under the wing. Therefore the takeoff performance of the FVK is affected less negatively by a OEI situation than the A35K.

5.1.3. Ground Effect Influence

In this section the influence of the ground effect on the takeoff performance of the FVK will be discussed. The simulated conditions are at sea level with MTOM. As explained in section 3.2.4 the influence of the ground effect is a function of AoA and ride height, and is likely considerably overestimated in this section. Nevertheless, keeping the limitations of the applied methods in mind, the general trends can be captured. Figure 5.9a shows the influence of the ground effect on the horizontal distances travelled during different takeoff phases. Figure 5.9b shows the influence of the ground effect on aerodynamic coefficients during a typical takeoff run between V_R and reaching the screen height. It can be seen that as the pitch attitude increases, the ride height decreases and the magnitude of the ground effect increases. As the wing gets closer to the ground, additional lift is generated while the induced drag decreases. Note that the changes in lift and drag coefficient are momentarily zero as the pitch attitude (and AoA) becomes zero. This is because the Flying-V study into the ground effect [24] showed that for zero AoA the ground effect can be neglected regardless of the ride height, as shown in Figure 3.8. As can be understood from Figure 5.9b the ground effect aides the aircraft in accelerating both forward and upward. Therefore it can be expected that the takeoff distance decreases. This is confirmed by Figure 5.9a. The horizontal distances of each phase are reduced by the ground effect. The ground effect has the least influence during the pre-rotation phase, as the wing is relatively high above the runway. Nevertheless Figure 5.9b shows that even during the pre-rotation phase the induced drag is reduced considerably by 30 cts, which is approximately 20% of the total drag at that stage. The airborne distance is reduced as well, as the lift coefficient is increased by approximately 0.03 at the start of the airborne phase, which decreases as the takeoff progresses. Especially the rotation distance is significantly shortened by the influence of the ground effect due to the additional lift and large drag decrease.

The takeoff distance decrease due to ground effect becomes smaller as the CG shifts aft. This is because for a more rearward CG the aircraft is easier to rotate, decreasing the rotation time. Therefore the aircraft can benefit less from the advantages of the ground effect for more rearward CG positions.

(a) Ground effect takeoff run distances

(b) Ground effect aerodynamics
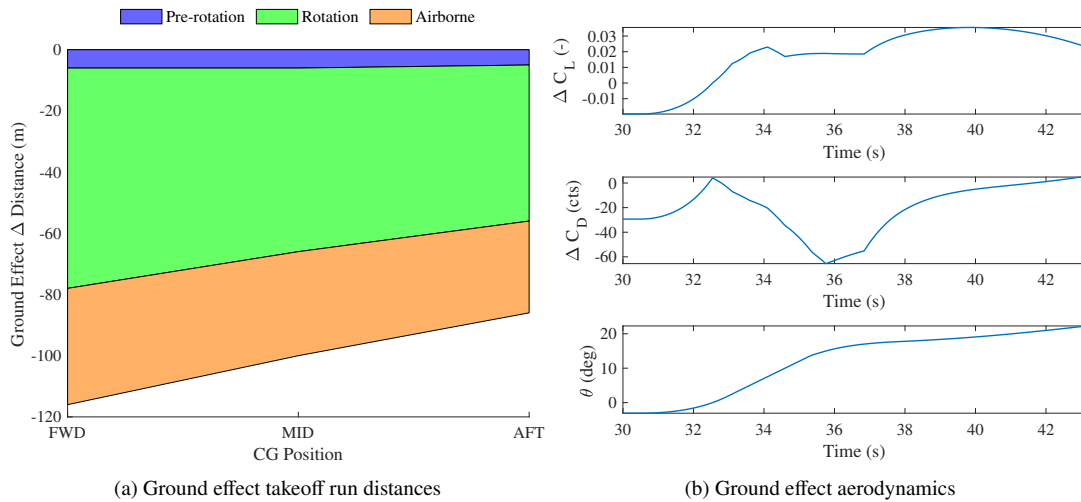
Figure 5.9: Balanced Field Length (BFL) comparison of reference velocities as a function of takeoff mass and centre of gravity position.

5.2. LANDING PERFORMANCE

Background information regarding landing definitions and regulations is presented in section 2.2.1 and a more detailed description of the landing manoeuvre is given in section 3.7.3. The landing manoeuvres are performed at sea level, with the maximum landing mass. The MLM and V_{app} can be found in Table 2.2. Figure 5.10 presents a comparison of horizontal distances travelled during different landing phases. The distance differences per landing phase are shown in Figure 5.11. It can be seen that the FVK and A35K have similar landing distances. For the most aft CG location, the FVK has a shorter landing distance, while for the mid-range and forward-limit CG position the A35K landing distance is shorter. Apparently, the Flying-V landing distance is more sensitive to the CG location. Although the total landing distances of both aircraft are similar, it can be observed that the distances covered during the different landing phases are differently distributed. The Flying-V features a superior braking performance, while the derotation distance is much longer for the Flying-V. This is due to a higher pitch attitude at touchdown, the ground attitude of -3 degrees and the imposed condition of a constant derotation rate. It would be expected that the airborne distances of both aircraft would be similar. However, the A35K covers a slightly larger distance during the airborne phase than the FVK. An explanation could be that the A35K has to reduce its descent rate slightly more than the FVK to arrive at the same descent rate at touchdown. This is because both aircraft arrive at the screen height at a flight path angle of -3 degrees, but the A35K has a slightly higher approach speed. This higher approach speed also contributes to the longer airborne distance, as more horizontal distance is covered per second. Together with a slightly more aggressive flare this could explain the airborne distance difference. Another explanation could be that for the flaring manoeuvre, control gains had to be tweaked in order to achieve the desired 6 ft/s descent rate as described in section 3.7.3. However, it is possible that for the FVK this method resulted in a more efficient path to the runway than for the A35K, causing the airborne distance to be larger than necessary. To eliminate this uncertainty, it would be recommended to optimise the control gains for the shortest airborne distance, although this has not been done during this research. For both aircraft it can be seen that the derotation distance decreases as the CG shifts rearwards, which is due to a lower touchdown pitch attitude. For the FVK this effect has a larger impact on the landing distance than for the A35K.

For both aircraft, the braking distance is minimal for the mid-range CG position. This is due to a trade-off between the aerodynamic and gravitational load on the main landing gear. This is demonstrated by the left-hand figure of Figure 5.12, showing the load on the main gear during landing. Shifting the CG forward allows a higher aerodynamic main gear load while keeping at least 8% of the weight on the nose gear wheel, as the CG generates a larger moment around the main gear wheels. Figure 5.12 shows that shifting the CG forward causes a higher peak load on the main gear wheels, which results in the largest peak deceleration as well. However, as dynamic pressure decreases while braking, the load balance converges towards the static equilibrium at rest. Therefore it can be seen that for a more forward CG the main gear load is smaller towards the end of the landing manoeuvre. Apparently, the mid-range CG position results in the most favourable combination of aerodynamic and gravity loads on the main gear wheels that maximises the area under the deceleration curve in Figure 5.12.
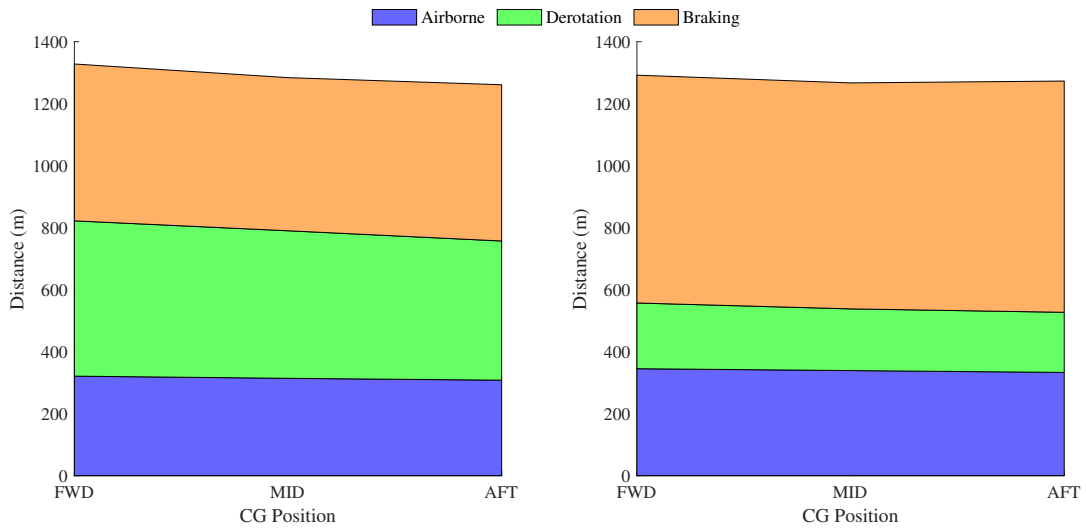
Figure 5.10: Landing distances comparison of the FVK (left) and A35K (right) for different landing phases.
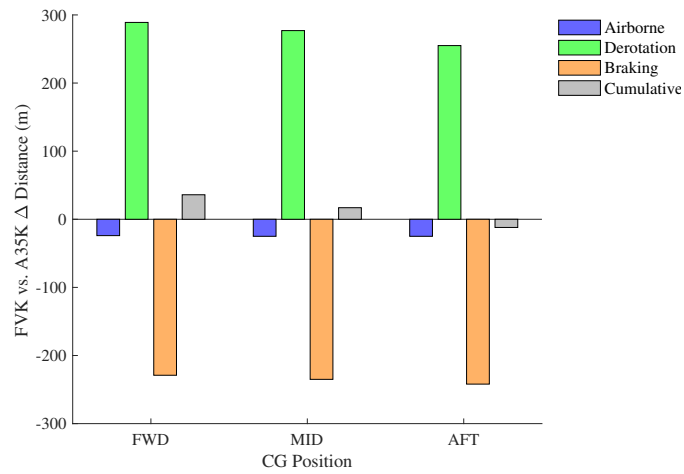
Figure 5.11: Comparison of landing distance differences between the FVK and A35K per phase.
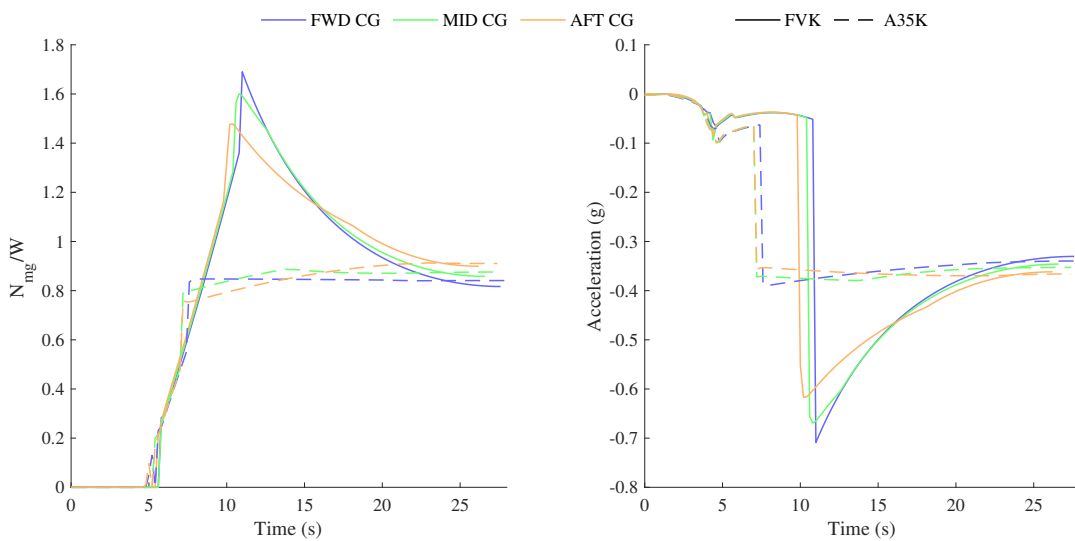
Figure 5.12: Load on the main gear wheels (left) and deceleration (right) during landing.

A notable difference in braking distance is observed between the FVK and A35K. The right-hand figure of
Figure 5.10 shows that the peak deceleration of the FVK can be as much as 0.7g, while the A35K deceleration
rate peaks at 0.4g. This difference can be explained by looking at Figure 5.12, which shows that the FVK is much
better able to apply an aerodynamic load on the main gear wheels. Both aircraft use spoilers for lift dumping
during braking, but the FVK also uses all its trailing-edge control surfaces to generate downforce. As the A35K
only uses its horizontal tail for pitch control, it can be expected that the A35K is unable to generate the levels
of downforce that the FVK can using its trailing edge devices. More importantly, the airframes of both aircraft
in landing configuration are very different. The A35K has landing flaps extended and a ground attitude of zero
degrees. The FVK has no flaps and a -3 degrees ground attitude. From Figure 3.3 it can be seen that the A35K,
without spoiler deployment, has a lift coefficient of approximately 0.8 in landing configuration at zero AoA,
while the FVK has a lift coefficient of approximately -0.2 at -3 AoA. Hence, the FVK naturally produces an
aerodynamic load on the main gear wheels while travelling down the runway, while the A35K aerodynamically
reduces the load on the main gear wheels. Based on this observation, a sensitivity analysis for the FVK was
performed to assess the influence of the ground attitude on the landing performance. This is shown in Figure 5.13.
The left-side figure shows the horizontal distances travelled during derotation and braking and the total distance
from screen height to standstill. The right-side figure compares these distances for different ground attitudes to
the FVK ground attitude of -3 degrees. Clearly, when changing the ground attitude, a trade-off is made between
the derotation distance and the braking distance. For both CG positions, the braking distance increases with
ground attitude as airframe lift is increased, unloading the main gear wheels. On the contrary, the derotation
distance decreases with increasing ground attitude, as expected. Interestingly, the overall influence on the landing
distance shows different trends for the forward and aft CG positions. For the forward CG position the advantage
of a shorter derotation distance outweighs the disadvantage of a longer braking distance, while for the aft CG
position it is the other way around. Hence, no general conclusion can be drawn for all CG positions regarding the
influence of the ground attitude on the landing distance.
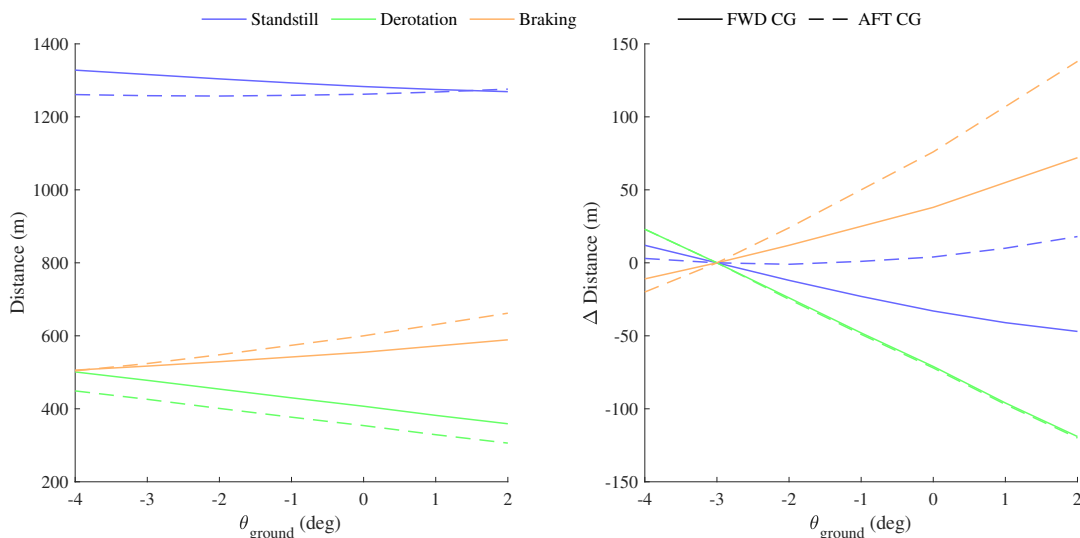
Figure 5.13: Influence of the ground attitude on the FVK landing distance. Right side: comparison with respect to $\theta_{\text{ground}} = -3$ deg.

5.2.1. Pilot Vision
Due to its highly swept wing and the absence of high lift systems, the FVK is required to land at a larger pitch
attitude than the A35K. During the flare manoeuvre the pitch attitude is increased even more to slow the descent
rate, while a more forward CG also increases the pitch attitude. A comparison of the pitch attitude during the
flaring manoeuvre is shown in Figure 5.14. At high pitch attitudes it may become problematic for the pilots to
have a clear view of the runway. Therefore it is relevant to know the view that the pilots have from the cockpit
during the flaring manoeuvre. Pilot vision definitions, including the obscured segment, are shown in Figure 2.4.
The pilot's eye is assumed to be located 1.87 m behind the nose and 1.00 m above the aircraft centre line, based on
preliminary results from an ongoing research into the aerodynamic optimisation of the Flying-V cockpit. Based
on the same study the overnose angle, denoted as the cockpit-cutoff angle in Figure 2.4, is assumed to be 25.7
degrees for the FVK and 20 degrees for the A35K [40]. Figure 5.14, shows the altitude of the pilot's eye and the
obscured segment during landing. The obscured segment is the horizontal distance to the closest point on the

ground that the pilot can see.
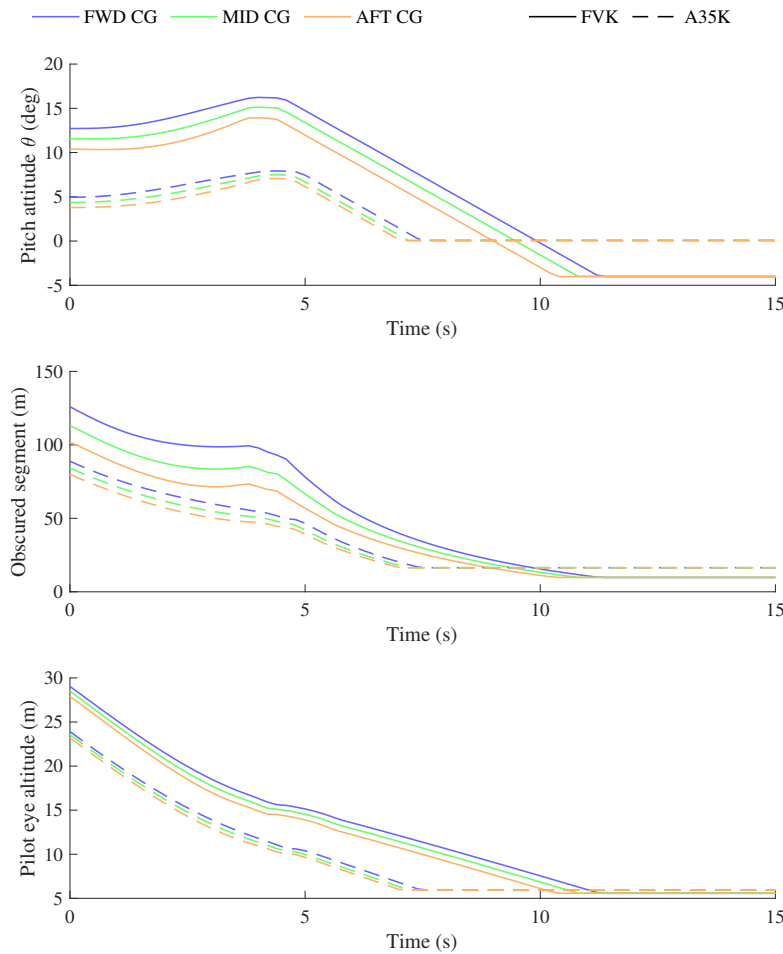
Figure 5.14: Comparison of the pitch attitude, obscured segment and pilot eye altitude during the flaring manoeuvre.

From Figure 5.14 it can be seen that the FVK flies at a much larger pitch attitude than the A35K throughout the airborne phase of the manoeuvre. This also results in a higher pilot eye position and larger obscured segment. As the aircraft gets close to the ground, the nose is pulled up, increasing the pitch attitude and obscured segment. The obscured segment of the FVK can be up to twice as large as the A35K obscured segment, depending on the CG position. For both aircraft, it can be seen that the landing pitch attitude increases when the CG is shifted forward, which also results in a significantly larger obscured segment.

5.3. CLIMB PERFORMANCE

In this section the climb performance characteristics of the FVK and A35K are compared at MTOM and the forward-limit CG position. The aircraft is trimmed at the prescribed thrust setting at various points in the airspeed-altitude plane. Hence, the resulting climb gradients are obtained for steady climb. Based on the resulting climb contours a number of different climb aspects can be compared, such as the fastest and steepest climb trajectories and service ceilings. Note the difference between the definitions of the service ceiling and the *absolute* service ceiling. The absolute service ceiling is defined as the maximum altitude that an aircraft can reach, where the maximum climb gradient is zero at maximum available thrust. The service ceiling is defined as the maximum altitude where an aircraft can sustain a steady climb rate of 100 ft/min (≈ 0.5 m/s) at maximum continuous thrust. For background theory on climb performance evaluation the reader is referred to section 2.2.2.
Figure 5.16 and Figure 5.17 show a climb contour comparison at maximum continuous and maximum available thrust, respectively. The drag divergence Mach numbers of both aircraft, presented in Table 5.2, and the sonic speed are drawn as a reference. In Figure 5.16 the service ceiling is shown, as this is determined at maximum continuous thrust, while Figure 5.17 shows the absolute service ceiling. The maximum angle of climb (AoC) and

rate of climb (RoC) are shown as a function of altitude and airspeed. For a given T/W, the AoC is maximised for maximum aerodynamic efficiency L/D. The maximum RoC is found by maximising C_L^3/C_D^2, as explained in section 2.2.2. Therefore the maximum AoC and RoC are not located at the same location in the airspeed-altitude plane, and different trajectories for fastest and steepest climb exist. From the climb contour plots it can be seen that the FVK has a higher service ceiling and absolute service ceiling than the A35K. This result was expected, as Figure 3.3 shows that the FVK possesses a higher maximum L/D. The service ceiling values are presented in Table 5.4.

Table 5.4: Service ceiling comparison at MTOM and forward-limit CG position.

	Flying-V-1000	Airbus A350-1000
Service ceiling (km)	12.0	10.7
Absolute service ceiling (km)	13.4	12.0

Figure 5.16 and Figure 5.17 also show the locus for fastest and steepest climb. These are the trajectories that should be followed to minimise the horizontal distance and the climb time of the climb trajectory, respectively. These trajectories at maximum available thrust are compared for both aircraft in Figure 5.15. For most altitudes the steepest climb trajectory of the FVK is located at a lower airspeed than for the A35K, while their steepest climb trajectories cross over at approximately 7 km and again at 11 km. According to the theory presented in section 2.2.2, the airspeed for fastest climb should be larger than the airspeed for steepest climb for a given altitude. For both aircraft, this is holds for the majority of the simulated altitude range. However, at approximately 11.9 km the steepest climb speed becomes larger than the fastest climb speed for the A35K, while this happens at approximately 13.4 km for the FVK. Looking at the theory in section 2.2.2 it can be seen that the statement that the airspeed for fastest climb should be larger than the airspeed for steepest climb actually only holds if the maximum AoC is positive. Hence, it can be expected that the steepest and fastest climb trajectories cross over at the maximum altitude where steady level flight can be attained. For maximum available thrust this altitude is the absolute service ceiling. Looking at Table 5.4 it can seen that the crossover point of the steepest and fastest climb trajectories indeed occurs at the absolute service ceiling for both aircraft. For altitudes beyond this point, the maximum AoC and RoC that can be attained is negative. Hence at these altitudes the steepest and fastest climb trajectories are actually the least negative AoA and RoC trajectories.
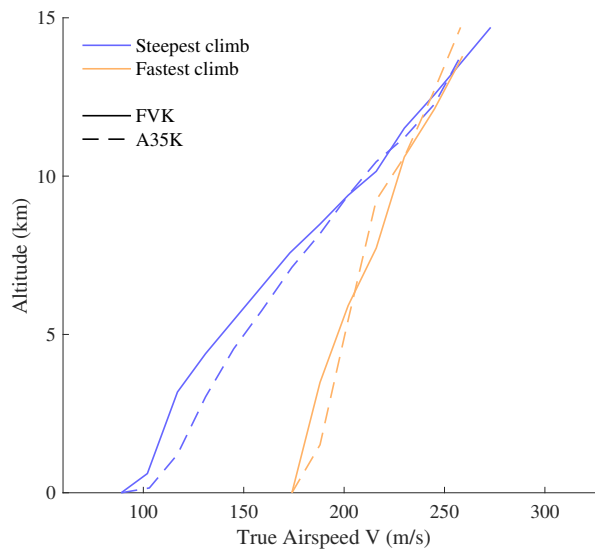
Figure 5.15: Fastest and steepest climb locus comparison for maximum available thrust.
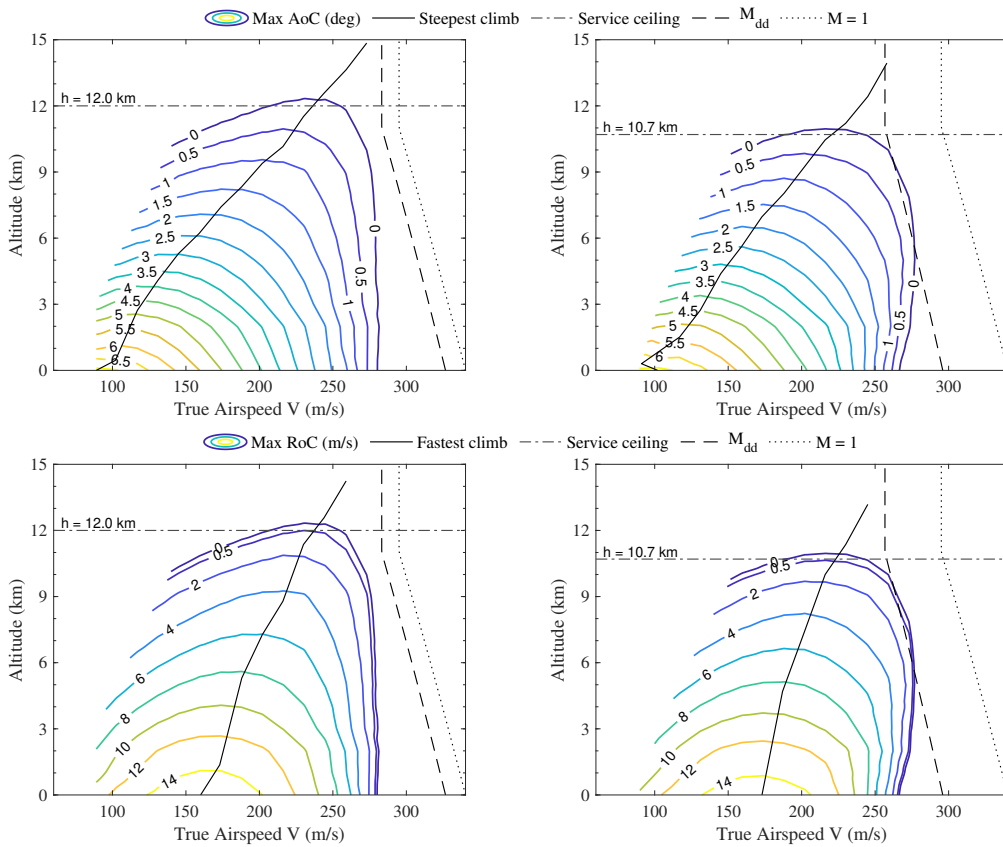
Figure 5.16: Climb performance comparison of the FVK (left) and A35K (right) at maximum continuous thrust and MTOM.
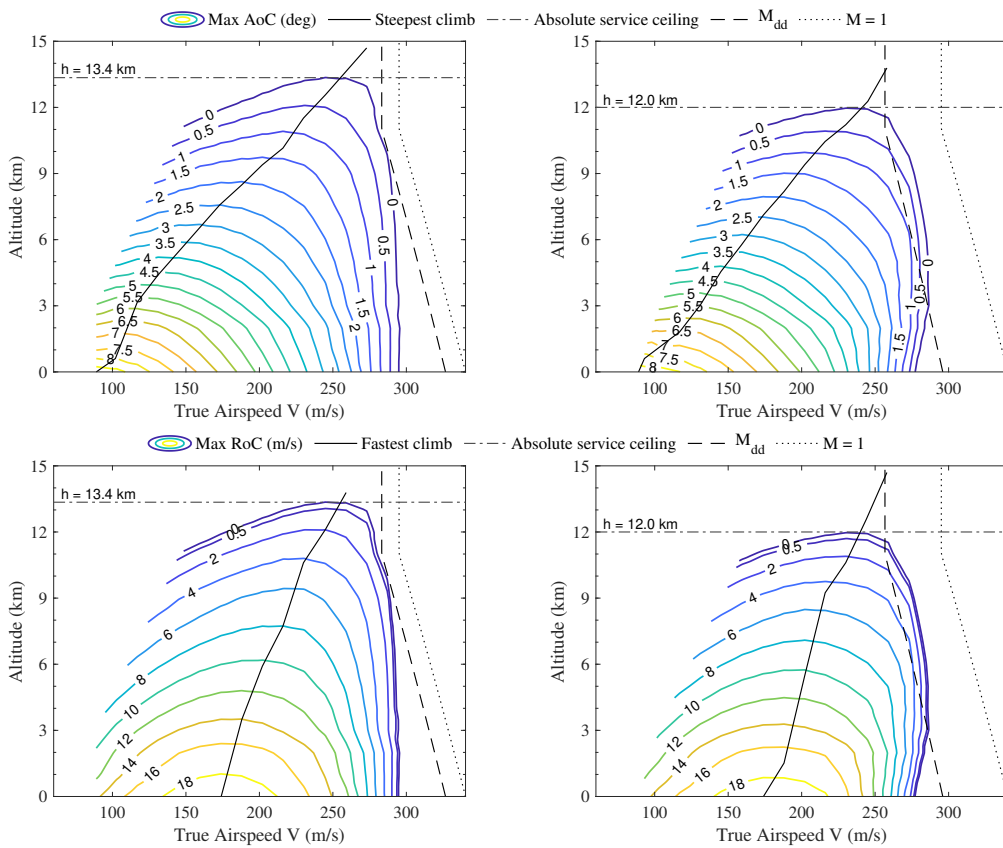
Figure 5.17: Climb performance comparison of the FVK (left) and A35K (right) at maximum available thrust and MTOM.

5.3.1. ONE ENGINE INOPERATIVE CLIMB

As described in section 2.2.2, two-engined aircraft are required by CS25 [43] to be able to attain an AoC of at least 1.37 degrees with OEI at the takeoff safety speed V_2 with the landing gear retracted. In this section the climb performance of both aircraft with OEI is compared at different takeoff masses and altitudes with the CG at the most forward position. This CG position has been chosen as this results in the smallest AoC. Figure 5.18 shows the AoC (left) with one engine inoperative at the optimal V_2 (right) that minimises the takeoff distance. In line with results shown in previous sections, the reference speed V_2 is higher for the A35K than for the FVK. From Figure 5.18 it can be concluded that the FVK achieves a larger AoC at each altitude and mass fraction than the A35K. The attained AoC reduces with increasing mass and altitude due to reduced T/W and air density. The required AoC is plotted as well, and it can be seen that the FVK achieves the required AoC for all tested altitudes and takeoff masses. The A35K meets the climb requirements for most cases, except at the highest altitude under consideration at MTOM. In order to meet the requirements for OEI climb at 8000 ft, the A35K could take off with a lower mass of at most 94% of the MTOM. Alternatively, in the hypothetical case that a new engine could be installed, an engine with 8% more thrust would provide sufficient thrust. For the FVK it can be concluded that matching the A35K thrust-to-weight ratio provides sufficient thrust to meet the climb gradient requirements imposed by CS25.121 up to altitudes of 8000 ft.
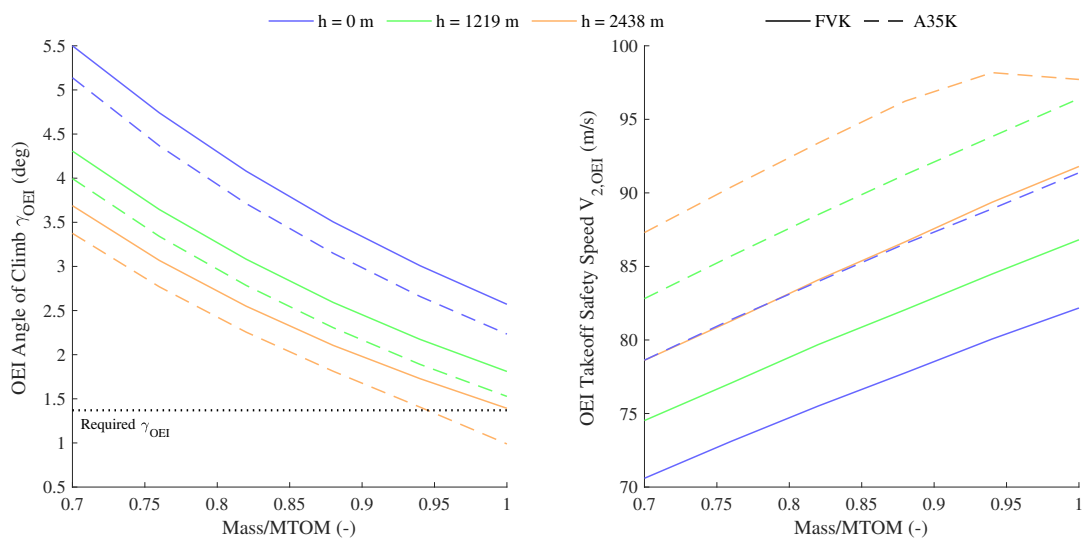
Figure 5.18: Comparison of the OEI angle of climb and V_2 optimised for minimum takeoff distance.

5.4. CRUISE PERFORMANCE

Table 5.5: Cruise performance parameters comparison.

	Flying-V-1000			Airbus A350-1000		
	Value	Mach	C_L	Value	Mach	C_L
L/D_{max}	23.7	0.75	0.37	20.3	0.65	0.71
ML/D_{max}	18.9	0.82	0.32	15.6	0.83	0.53
RP_{max}	9.7	0.82	0.32	8.0	0.75	0.69

In this section the cruise performance of the FVK and A35K is compared at MTOM. The aircraft are trimmed in steady level flight at different points in the airspeed-altitude plane. The results are summarised in Table 5.5. For background theory regarding cruise performance and the different cruise performance parameters discussed in this section, the reader is referred to section 2.2.2. The main takeaways from the background theory are that cruise performance is evaluated based on the specific air range (SAR) parameter, which is defined as the range covered per unit of consumed fuel. When the powerplant efficiency is assumed to be constant, the SAR is proportional to the aerodynamic efficiency L/D. When the thrust specific fuel consumption (TSFC) is assumed to be constant, the SAR is proportional to the transonic efficiency ML/D. When TSFC is not assumed to be constant, the SAR is proportional to the more general range parameter [48]. Results are summarised in Table 5.5.

Contour plots of the trimmed L/D of both aircraft as a function of Mach number and lift coefficient are shown in Figure 5.19. The maximum trimmed L/D of the FVK is 23.7, which is 17% higher than for the A35K. It can be seen that for both aircraft the maximum trimmed L/D is located at a smaller Mach number than the assumed cruise Mach number value of 0.85. This is most likely due to transonic wave drag. However, despite the larger drag divergence Mach number of the FVK, both aircraft experience a similar amount of wave drag at the cruise Mach number due to the larger wing thickness-to-chord ratio of the FVK. Nevertheless wave drag decreases more rapidly for the A35K for Mach numbers smaller than the reference cruise Mach number. Therefore wave drag could still be the reason why the peak trimmed L/D is located at a lower Mach number for the A35K. Another indication that this hypothesis may be true is the fact that the difference between the Mach numbers of maximum L/D is approximately equal to the difference in drag divergence Mach number, as can be concluded from Table 5.2 and Table 5.5.

In Figure 5.20 contour plots of ML/D are drawn in the C_L-Mach plane. As the transonic efficiency is closely related to the aerodynamic efficiency, the FVK outperforms the A35K in terms of ML/D as well. The maximum trimmed ML/D of the FVK is found to be 18.9, compared to 15.6 for the A35K. Therefore the maximum ML/D is 21% higher than for the A35K. Contrary to the maximum L/D, it can be seen that the transonic efficiency peak values occur at similar Mach numbers for both aircraft.

In order to compare the range parameter RP of both aircraft, the TSFC is calculated as described in section 3.4.3 with a method from [63]. The resulting RP contour plots are shown in Figure 5.21. The maximum RP of the FVK is 9.74, while the A35K maximum RP is 8.05. Therefore the FVK outperforms the A35K by 21% in terms of the maximum RP, which occurs at Mach 0.82 for the FVK and at Mach 0.78 for the A35K. It can be concluded that when the least simplifying assumptions are made, which is the case for the RP, the amount of range covered per unit consumed fuel is 21% larger for the FVK than for the A35K, while both aircraft achieve their maxima at Mach numbers close to the assumed reference Mach number. The maximum RP values of the FVK and A35K occur at C_L values of 0.32 and 0.69, respectively. If both aircraft would be cruising with a mass equal to the MOTM, at the Mach number and lift coefficient that maximise RP, this would yield an optimal cruise altitude of 12.0 km for the FVK and 11.3 km for the A35K. For the FVK this is exactly the same altitude as its service ceiling (note, not the absolute service ceiling). For the A35K this optimal cruise altitude is higher than its service ceiling, but approximately equal to the maximum attainable altitude at maximum continuous thrust.

(a) Flying-V-1000

(b) Airbus A350-1000
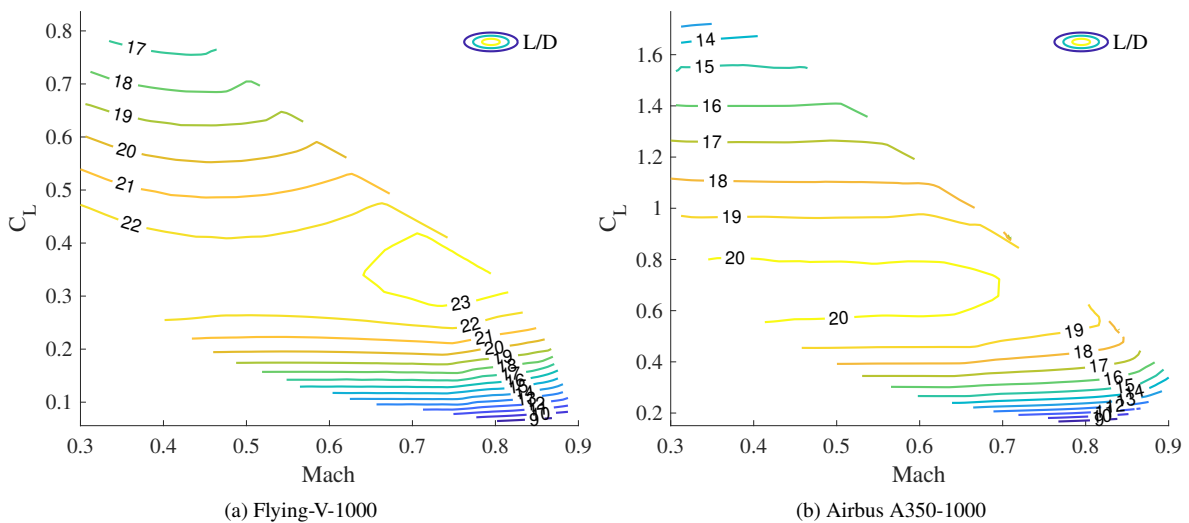
Figure 5.19: Trimmed aerodynamic efficiency L/D contour plots as a function of lift coefficient and flight Mach number.

(a) Flying-V-1000

(b) Airbus A350-1000
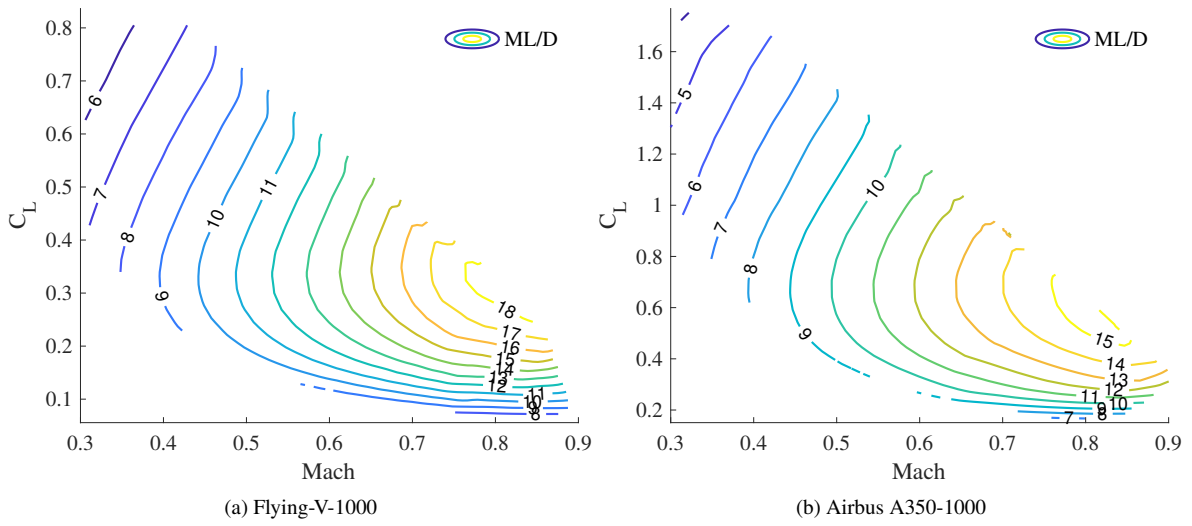
Figure 5.20: Transonic efficiency ML/D contour plots as a function of lift coefficient and flight Mach number.

(a) Flying-V-1000

(b) Airbus A350-1000
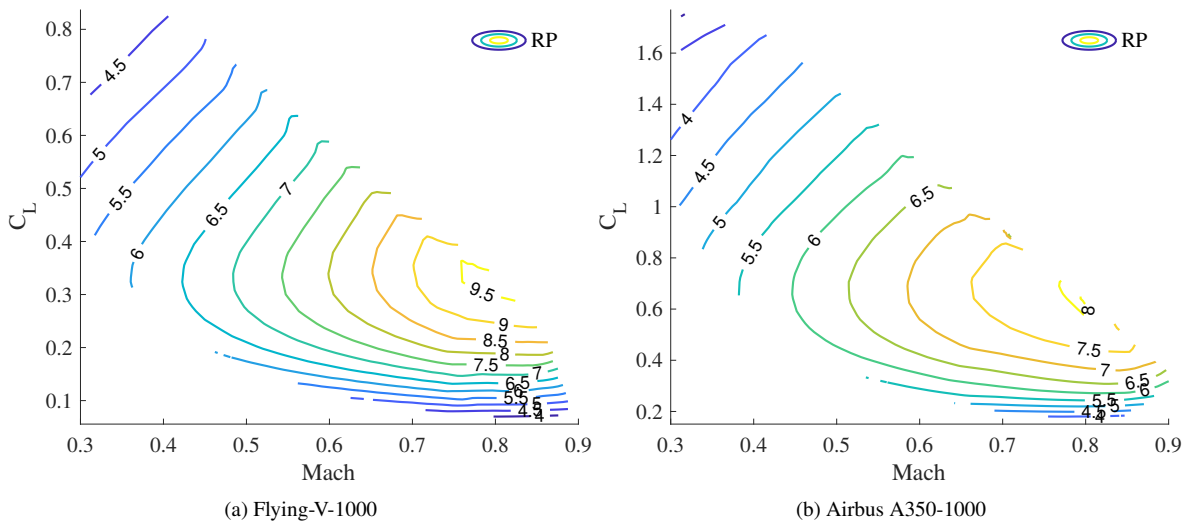
Figure 5.21: Range Parameter RP contour plots as a function of lift coefficient and flight Mach number.

<div style="text-align: right; font-size: 3em; font-weight: bold;">6</div>

CONCLUSIONS AND RECOMMENDATIONS

This research evaluates and compares the flight performance characteristics of the Flying-V-1000 (FVK) and the Airbus A350-1000 (A35K) under the assumption of an identical thrust-to-weight ratio. A flight mechanics model was used to simulate takeoff, landing, climb and cruise. In this chapter conclusions are drawn, answers to the research questions are formulated and recommendations for future research are presented.

6.1. CONCLUSIONS

On average, the FVK features a 25% shorter takeoff distance than the A35K. This difference is mainly due to the significantly longer pre-rotation phase of the A35K, which is the consequence of the larger minimum unstick speed of the A35K. This leads to a higher rotation initiation speed, which also increases the horizontal distances of the rotation and airborne phases. The minimum unstick speed of the A35K is 7-11 m/s higher than for the FVK, depending on the takeoff mass, CG position and altitude. It has been shown that this is mainly due to the much larger tailstrike attitude of the FVK. For both aircraft, geometric tailstrike constraints determine the minimum unstick speed, rather than the elevator effectiveness. The shorter takeoff distance of the FVK also leads to a shorter Balanced Field Length. On average, the BFL of the FVK is 30% shorter than for the A35K. This relative difference between the BFL of both aircraft is larger than for the takeoff distance, because the FVK is able to brake more effectively than the A35K.

The landing distances and approach speeds of both aircraft are similar, although the total landing distance is distributed differently over the phases of the landing manoeuvre. Due to its highly swept wing, the FVK has a larger touchdown attitude than the A35K, while it also has a smaller ground attitude. Therefore, the derotation distance of the FVK is significantly larger than for the A35K, as it is assumed that both aircraft derotate at the same angular rate. Due to its braking capabilities, the FVK is able to compensate its longer derotation distance with a shorter braking distance to achieve a similar total landing distance as the A35K. It has been shown that the FVK can more effectively transfer an aerodynamic load to the main gear wheels due to the absence of high lift devices and a negative ground attitude. As a consequence, the peak deceleration of the FVK can assume values up to 0.7 g, while the maximum deceleration of the A35K is 0.4 g. A sensitivity analysis of the influence of the ground attitude of the FVK on the landing distance has shown that the optimal ground attitude that minimises the landing distance depends on the position of the CG. An analysis of the pilot's vision during the landing flare manoeuvre has shown that the obscured segment can be up to twice as large for the FVK as for the A35K. For landings performed with poor visibility, this could be problematic for the FVK.

Due to its larger maximum L/D, the FVK has better climb performance characteristics than the A35K. With One Engine Inoperative, the FVK was able to meet the climb gradient requirements of CS25.125 for altitudes up to 8000 ft at MTOM. The A35K has been found to be able to meet these requirements for most situations, but for a takeoff at 8000 ft the takeoff mass should be less than 94% of the MTOM to comply with the aforementioned regulations. The service ceilings of the FVK and the A35K are 12.0 km and 10.7 km, respectively. The absolute service ceilings were found to be 13.4 km and 12.0 km for the FVK and A35K, respectively. The lower service ceiling of the A35K is also partially due to its lower Mach divergence number. Comparing the trajectories of steepest and fastest climb shows that the FVK trajectory for steepest climb is located at a lower airspeed for altitudes lower than 9.5 km and altitudes higher than 11 km. The FVK trajectory for fastest climb is located at a lower airspeed for altitudes below 7 km.

Evaluation of the Specific Air Range (SAR) parameter, which is defined as the range convered per unit consumed fuel, shows that the FVK outperforms the A35K in terms of cruise efficiency. The maximum trimmed L/D of the FVK has been found to be 23.7, compared to 20.3 for the A35K, which is a 17% difference. The maximum transonic efficiency of the FVK has been found to be 18.9, which is 21% higher than the value of 15.6 found for the A35K. The maximum value of the Range Parameter, which takes into account that the thrust specific fuel consumption depends on altitude and flight Mach number, is also found to be higher for the FVK. The maximum RP was found to be 9.7 for the FVK and 8.0 for the A35K, a 21% difference. The Mach number and lift coefficient at which the RP maxima are located suggest an optimal cruise altitude of 12.0 km for the FVK and 11.3 km for the A35K.

It can be concluded that for an identical thrust-to-weight ratio the Flying-V outperforms the reference aircraft in terms of takeoff, climb and cruise performance. The landing performances of both aircraft in terms of landing distance are similar, although the significantly larger obscured segment of the pilot's vision could cause problems for the Flying-V during landing with poor visibility.

Every model has its limitations, and the flight mechanics model used in this research is no exception to this rule. In the following section, these limitations will be addressed and recommendations for future research are made to improve the predictive qualities of the flight mechanics model.

6.2. Recommendations

To improve the predictive qualities of the flight mechanics model used in this research, a number of recommendations can be made.

- The present research makes use of aerodynamic coefficients generated by a VLM enhanced with empirical zero-lift drag and wave drag models. Moreover, the empirical data does not include flying wing aircraft. Therefore it is unknown to what extent these models are able to predict the characteristics of the Flying-V. Although VLMs are attractive in the preliminary and conceptual design phase due to their low computational cost, VLMs are inherently limited due to absence of thickness and viscosity effects. Predictive qualities of the flight mechanics model could be improved by relying on higher fidelity aerodynamic solvers such as RANS solvers.

- During takeoff and landing, a considerable portion of the manoeuvre is performed in ground proximity. As literature suggests that the ground effect can significantly influence induced drag and lift, it may be worth investigating the dynamic influence of the ground effect. Additionally, the ground effect with deflected trailing edge devices could be investigated as this is relevant during the rotation phase and considerably influences the flow field.

- The braking and friction coefficients of the landing gear are assumed to be constant in this research. However, these values depend on many factors and therefore the complexity of determining these parameters is much larger than this research assumes. Modelling the interaction of the landing gear tires and shock dampers with the runway using multi-body physics could provide better insights into the actual values of the friction and braking coefficients at each time instant. This would include taking into account tyre skidding and braking dynamics.

- Inertia matrices used in this research are based on a preliminary structural sizing study. A detailed weight & balance model for different loading strategies would improve the accuracy of the inertia tensor.

- The propulsion model is based on experimental data from two-shaft turbofan engines with a BPR of 3 to 9 and an OPR of 18 to 36. The model has a high accuracy for the sampled engines, but therefore it is possibly over-fitted to predict thrust for engines outside the sample range accurately. Modern high BPR turbofan engines have BPR values of approximately 10 and OPR values of 50 and often use a three-shaft architecture. It is expected that future high BPR engines will have BPR values of up to 15 and an OPR of up to 70[1]. Therefore it could be worthwhile to consider modelling these engines using OpenModelica [69], GTPy [70] or GSP [71]. These programs allow to build engine architectures in a component-based manner.

---

[1]Rolls Royce. https://www.rolls-royce.com/products-and-services/civil-aerospace/future-products (Accessed: March 8, 2022).

BIBLIOGRAPHY

[1] R. Martinez-Val, E. Perez, J. Puertas, and J. Roa. Optimization of planform and cruise conditions of a transport flying wing. *Proceedings of the Institution of Mechanical Engineers, Part G: Journal of Aerospace Engineering*, 224:1243–1251, 2010. ISSN 09544100. doi: 10.1243/09544100JAERO812.

[2] Francesco Faggiano, Roelof Vos, Max Baan, and Reinier Van Dijk. Aerodynamic design of a flying V aircraft. In *17th AIAA Aviation Technology, Integration, and Operations Conference, 2017*, 2017. ISBN 9781624105081. doi: 10.2514/6.2017-3589.

[3] Airbus. Global Market Forecast 2019-2038: Cities, Airport and Aircraft. Technical report, 2018.

[4] A. L. Bolsunovsky, N. P. Buzoverya, B. I. Gurevich, V. E. Denisov, A. I. Dunaevsky, L. M. Shkadov, O. V. Sonin, A. J. Udzhuhu, and J. P. Zhurihin. Flying wing - Problems and decisions. *Aircraft Design*, 2001. ISSN 13698869. doi: 10.1016/S1369-8869(01)00005-2.

[5] R. H. Liebeck. Design of the Blended Wing Body Subsonic Transport. *Journal of Aircraft*, 2004. ISSN 15333868. doi: 10.2514/1.9084.

[6] R. Martinez-Val, J. F. Palacin, and E. Perez. The evolution of jet airliners explained through the range equation. *Proceedings of the Institution of Mechanical Engineers, Part G: Journal of Aerospace Engineering*, 2008. ISSN 09544100. doi: 10.1243/09544100JAERO338.

[7] R. Martinez-Val. Flying Wings. A New Paradigm for Civil Aviation? *Acta Polytechnica*, 47(1):32–43, 2007. ISSN 1805-2363. doi: 10.14311/914.

[8] Richard M. Wood and Steven X.S. Bauer. Flying wings / flying fuselages. In *39th Aerospace Sciences Meeting and Exhibit*, 2001. doi: 10.2514/6.2001-311.

[9] Vladimir G. Dmitriev, Leonid M. Shkadov, and Vladimir E. Denisov. The flying-wing concept-chances and risks. In *AIAA\ICAS International Air and Space Symposium and Exposition: The Next 100 Years*, pages 1–11, 2003.

[10] B. Mialon, T. Fol, and C. Bonnaud. Aerodynamic optimization of subsonic flying wing configurations. In *20th AIAA Applied Aerodynamics Conference*, pages 1–7, 2002. ISBN 9781624101106. doi: 10.2514/6.2002-2931.

[11] T. I. Saeed and W. R. Graham. Design study for a laminar-flying-wing aircraft. *Journal of Aircraft*, 52(5): 1373–1385, 2015. ISSN 15333868. doi: 10.2514/1.C032862.

[12] Dino Roman, Richard Gilmore, and Sean Wakayama. Aerodynamics of high-subsonic blended-wing-body configurations. In *41st Aerospace Sciences Meeting and Exhibit*, pages 1–9, 2003. ISBN 9781624100994. doi: 10.2514/6.2003-554.

[13] N. Qin, A. Vavalle, A. Le Moigne, M. Laban, K. Hackett, and P. Weinerfelt. Aerodynamic studies for blended wing body aircraft. In *9th AIAA/ISSMO Symposium on Multidisciplinary Analysis and Optimization*, pages 1–11, 2002. doi: 10.2514/6.2002-5448.

[14] N. Qin, A. Vavalle, A. Le Moigne, M. Laban, K. Hackett, and P. Weinerfelt. Aerodynamic considerations of blended wing body aircraft, 2004. ISSN 03760421.

[15] Tjoetjoek Eko Pambagjo, Kazuhiro Nakahashi, Shigeru Obayashi, and Kisa Matsushima. Aerodynamic design of a medium size blended-wing-body airplane. In *39th Aerospace Sciences Meeting and Exhibit*, 2001. doi: 10.2514/6.2001-129.

[16] Thomas A. Reist and David W. Zinggy. Aerodynamic design of blended wing-body and lifting-fuselage aircraft. In *34th AIAA Applied Aerodynamics Conference*, 2016. ISBN 9781624104374. doi: 10.2514/6.2016-3874.

[17] J. Benad. The Flying V - A new Aircraft Configuration for Commercial Passenger Transport. (September), 2015. doi: 10.25967/370094.

[18] Francesco Faggiano. *Aerodynamic Design Optimization of a Flying V Aircraft*. Msc thesis, Delft University of Technology, 2016.

[19] L. van der Schaft. *Development, Model Generation and Analysis of a Flying V Structure Concept*. Msc thesis, Delft University of Technology, 2017.

[20] Berta Rubio Pascual and Roelof Vos. The effect of engine location on the aerodynamic efficiency of a flying-v aircraft. In *AIAA Scitech 2020 Forum*, 2020. ISBN 9781624105951. doi: 10.2514/6.2020-1954.

[21] B. Rubio Pascual. *Engine-Airframe Integration for the Flying V*. Msc thesis, Delft University of Technology, 2018.

[22] Sjoerd Van Empelen and Roelof Vos. Effect of Engine Integration on a 4.6%-Scale Flying-V Subsonic Transport. 2021. doi: 10.2514/6.2021-0939.

[23] S van Empelen. *Engine Integration of the Flying V - Quantification of Engine Integration Effects using Wind Tunnel Experiments*. Msc thesis, Delft University of Technology.

[24] A. J. Santosh. *Influence of Ground Effect on the Flying V Aircraft*. Msc thesis, Delft University of Technology, 2020.

[25] R Viet. *Analysis of the flight characteristics of a highly swept cranked flying wing by means of an experimental test*. Msc thesis, Delft University of Technology, 2019.

[26] Marco Palermo and Roelof Vos. Experimental aerodynamic analysis of a 4.6%-scale flying-v subsonic transport. In *AIAA Scitech 2020 Forum*, 2020. ISBN 9781624105951. doi: 10.2514/6.2020-2228.

[27] Marco Palermo. *The Longitudinal Static Stability and Control Characteristics of a Flying V Scaled Model: An Experimental and Numerical Investigation*. Msc thesis, Delft University of Technology, 2019.

[28] A. Ruiz Garcia. *Aerodynamic Model Identification of the Flying V using wind tunnel data*. Msc thesis, Delft University of Technology, 2019.

[29] Alberto Ruiz-García, Roelof Vos, and Coen C. de Visser. Aerodynamic model identification of the flying V from wind tunnel data. In *AIAA AVIATION 2020 FORUM*, 2020. ISBN 9781624105982. doi: 10.2514/6. 2020-2739.

[30] J. J. D. van Uitert. *Experimental Investigation into the Effect of Aerodynamic Add-ons on the Aerodynamic Characteristics of the Flying V*. Msc thesis, Delft University of Technology.

[31] N Johnson. *Effect of Winglet Integration and Rudder Deflection on Flying-V Aerodynamic Characteristics*. Msc thesis, Delft University of Technology, 2021.

[32] O. Erdincler. *Aerodynamic and Performance Analysis of Ground Spoilers on the Flying V*. Msc thesis, Delft University of Technology, 2021.

[33] M Hillen. *Parametrisation of the Flying-V Outer Mould Line*. Msc thesis, Delft University of Technology, 2020.

[34] G Bourget. *The effect of landing gear implementation on Flying V aerodynamics, stability and controllability*. Msc thesis, Delft University of Technology, 2020.

[35] R. van der Pluijm. *Cockpit Design and Integration into the Flying V*. Msc thesis, Delft University of Technology, 2021.

[36] M.B.P. Claeys. *Flying V and Reference Aircraft Structural Analysis and Mass Comparison*. Msc thesis, Delft University of Technology, 2018.

[37] T. Cappuyns. *Handling Qualities of a Flying V Configuration*. Msc thesis, Delft University of Technology, 2019.

[38] S. K. Ojha. *Flight Performance of Aircraft*. American Institute of Aeronautics and Astronautics, Washington D.C., 1995. ISBN 1-56347-113-2. doi: 10.2514/4.861826.

[39] W. Oosterom. *Flying-V Family Design*. Msc thesis, Delft University of Technology, 2021.

[40] Airbus. Airbus A350 Aircraft Characteristics Airport and Maintenance Planning. Technical report, 2016.

[41] European Union Aviation Safety Agency (EASA). Type-Certificate Data Sheet: Trent XWB series engines, 2019. URL https://www.easa.europa.eu/sites/default/files/dfu/EASAE111TCDSissue12{_}TrentXWB.pdf.

[42] European Union Aviation Safety Agency (EASA). CS-25: Certification Specifications and Acceptable Means of Compliance for Large Aeroplanes. Amendment 26., 2020. URL https://www.easa.europa.eu/sites/default/files/dfu/cs-25{_}amendment{_}26{_}0.pdf.

[43] European Union Aviation Safety Agency (EASA). Certification Specifications and Acceptable Means of Compliance for Large Aeroplanes (CS-25). Amendment 27., 2021. URL https://www.easa.europa.eu/document-library/certification-specifications/cs-25-amendment-27.

[44] Thiago Degaspare, Pedro Paglione, and Cleverson Marinho. Development of a simulation environment for ground control laws design. In *Proceedings of the 23rd ABCM International Congress of Mechanical Engineering*, 2015. doi: 10.20906/cps/cob-2015-0499.

[45] G J J Ruijgrok. *Elements of Airplane Performance*. Delft Academic Press (VSSD), Delft, 2 edition, 2009. ISBN 9789065622037.

[46] Federal Aviation Administration. Pilot Guide to Takeoff Safety. URL https://www.faa.gov/other{_}visit/aviation{_}industry/airline{_}operators/training/media/takeoff{_}safety.pdf.

[47] Airbus. A330 Flight Deck and Systems Briefing For Pilots. Technical report, 2015.

[48] E. Torenbeek. *Optimum Cruise Performance of Subsonic Transport Aircraft*. Delft University Press, Delft, 1998.

[49] C. Varriale. Aircraft Performance Analysis and Mission Profile Optimization. PARSIFAL Deliverable D.6.1. Technical report, Delft University of Technology, 2018.

[50] D. A.J. Van Ginneken, Mark Voskuijl, Michel J.L. Van Tooren, and Aldo Frediani. Automated control surface design and sizing for the Prandtl Plane. In *Collection of Technical Papers - AIAA/ASME/ASCE/AHS/ASC Structures, Structural Dynamics and Materials Conference*, 2010. ISBN 9781600867422. doi: 10.2514/6.2010-3060.

[51] Mark Voskuijl, Jan de Klerk, and Daan van Ginneken. Flight Mechanics Modeling of the PrandtlPlane for Conceptual and Preliminary Design. In *Variational Analysis and Aerospace Engineering: Mathematical Challenges for Aerospace Design*, pages 435–462. Vol. 66 edition, 2012. doi: 10.1007/978-1-4614-2435-2_19.

[52] Carmine Varriale, Kevin Hameeteman, Mark Voskuijl, and Leo L. Veldhuis. A Thrust-Elevator Interaction Criterion for Aircraft Optimal Longitudinal Control. In *2019 AIAA Aviation Forum*, Dallas, TX, 2019. doi: 10.2514/6.2019-3001.

[53] Carmine Varriale and Mark Voskuijl. A Control Allocation approach to induce the center of pressure position and shape the aircraft transient response. *Aerospace Science and Technology*, 2021. ISSN 12709638. doi: 10.1016/j.ast.2021.107092.

[54] Carmine Varriale and Mark Voskuijl. A trim problem formulation for maximum control authority using the Attainable Moment Set geometry. *CEAS Aeronautical Journal*, 2022. ISSN 18695590. doi: 10.1007/s13272-021-00560-4.

[55] Mustafa Cavcar. The International Standard Atmosphere (ISA). *Anadolu University, Turkey*, 2000.

[56] C.Varriale. *Flight Mechanics and Performance of Direct Lift Control: Applying Control Allocation Methods to a Staggered Box-Wing Aircraft Configuration*. Phd thesis, Delft University of Technology, 2022.

[57] Airbus. A350-900 Flight Deck and Systems Briefing for Pilots. Technical report, 2011.

[58] C Rodney Hanke. The Simulation Of Large Jet Transport Aircraft. *NASA Contractor Report*, 1971.

[59] Daniel Raymer. *Aircraft Design: A Conceptual Approach*. 2013. ISBN 0-7918-4727-6.

[60] E. Torenbeek. *Synthesis of Subsonic Airplane Design*. Kluwer Academic Publishers, Dordrecht, 1982. ISBN 90-247-2724-3.

[61] J.A. Vargas Jimenez. *Development of a Wave Drag Prediction Tool for the Conceptual Design Phase*. Msc thesis, Delft University of Technology, 2015.

[62] Rc Feagin and Wd Morrison. Delta Method, An Empirical Drag Buildup Technique. *NASA CR-151971, Dec*, 1978.

[63] M. Bartel and T. Young. Simplified Thrust and Fuel Consumption Models for Modern Two-Shaft Turbofan Engines. *Journal of Aircraft*, 45(4):1450–1456, 2008. doi: 10.2514/1.35589.

[64] D. Scholz. Skript zur Vorlesung Flugzeugentwurf, Anhang C. 1999.

[65] Roelof Vos, Catherine Eeckels, Rommert Jan Schoustra, and Mark Voskuijl. Analysis of a ground-based magnetic propulsion system. *Journal of Aircraft*, 2014. ISSN 15333868. doi: 10.2514/1.C032555.

[66] P. G. Maropoulos and D. Ceglarek. Design verification and validation in product lifecycle. *CIRP Annals - Manufacturing Technology*, 2010. ISSN 00078506. doi: 10.1016/j.cirp.2010.05.005.

[67] Federal Aviation Administration. Chapter 13: Transition to Multiengine Airplanes. In *Airplane Flying Handbook*. 2021. URL https://www.faa.gov/regulations{_}policies/handbooks{_}manuals/aviation/airplane{_}handbook/media/14{_}afh{_}ch12.pdf.

[68] European Union Aviation Safety Agency (EASA). Type-certificate Data Sheet: Airbus A350-941 and A350-1041. Technical report, 2019.

[69] P. Fritzson, A. Pop, K. Abdelhak, A. Asghar, and B. Bachmann. The OpenModelica Integrated Environment for Modeling, Simulation, and Model-Based Developmen. *Modeling, Identification and Control*, 41(4):241–285, 2020. doi: 10.4173/mic.2020.4.1.

[70] P Proesmans. *Preliminary Propulsion System Design and Integration for a Box-Wing Aircraft Configuration: A Knowledge Based Engineering Approach*. Msc thesis, Delft University of Technology, 2019.

[71] Wilfried P.J. Visser and Michael J. Broomhead. GSP, a generic object-oriented gas turbine simulation environment. In *Proceedings of the ASME Turbo Expo*, 2000. ISBN 9780791878545. doi: 10.1115/2000-GT-0002.

[72] Egbert Torenbeek. Development and Application of a Comprehensive, Design-sensitive Weight Predicition Method for Wing Structures of Transport Category Aircraft. Technical report, 1992.

[73] H. Schlichting and E.A. Truckenbrodt. *Aerodynamik des Flugzeuges: Erster Band*. 2000.

[74] H. Schlichting and E.A. Truckenbrodt. *Aerodynamik des Flugzeuges: Zweiter Band*. 2000.

A

ZERO-LIFT DRAG CALCULATIONS

This appendix elaborates on the methodology and geometry used to estimate the zero-lift drag of the Flying-V and reference aircraft. Equations from Raymer [59] and Torenbeek [72] form the basis of this semi-empirical approach. The relevant geometry data has been obtained from Airbus [40] and previous Flying-V research.

To calculate zero-lift drag, the component buildup method described by Raymer is used. Contributions of the wings, fuselage, nacelles, pylons, landing gear, flaps and drag due to leakage and protuberances are summed to calculate the total zero-lift drag.

$$C_{D_0} = C_{D_{0\text{wings}}} + C_{D_{0\text{fus}}} + C_{D_{0\text{nac}}} + C_{D_{0\text{pyl}}} + C_{D_{0\text{LG}}} + C_{D_{0\text{leak}}} + C_{D_{0\text{flap}}} \tag{A.1}$$

For the wings, fuselage, nacelles and pylons the zero-lift drag coefficient is calculated using the flat plate skin-friction coefficient C_f, a form factor f to account for wave drag, an interference factor Q and the wetted area of the component S_{wet}. For each component the zero-lift drag contribution can be calculated using Equation A.2, where subscript c denotes the respective component.

$$C_{D_{0c}} = C_{f_c} \cdot f_c \cdot Q_c \frac{S_{\text{wet}_c}}{S} \tag{A.2}$$

It is assumed that the flow is turbulent due to the large Reynolds numbers during operation. The flat plate skin-friction coefficient for turbulent flow is given by Equation A.3 [59].

$$C_f = \frac{0.455}{(\log_{10} Re)^{2.58} (1 + 0.144 M^2)^{0.65}} \tag{A.3}$$

The skin friction coefficient is a function of the Reynolds number, which depends on the characteristic length scale of each component. Hence, the skin friction coefficient has to be calculated for each component separately. Equations for the form factor and wetted area of each component are presented in the sections below. The interference factor Q has been taken from Raymer [59], where a mid-range value is chosen in the cases where a range of valid values was presented. A summary of the parameters in Equation 3.9 for each component is displayed in Table A.1 and Table A.2 for the Flying-V and the Airbus A350, respectively.

A.1. WINGS

For each wing segment, the form factor is calculated using Equation A.4 by Torenbeek [60], where the thickness-to-chord ratio $\left(\frac{t}{c}\right)$ is taken to be the average of the root and tip section of the segment. $\Lambda_{0.5}$ is the half-chord sweep angle of the segment.

$$f_{\text{wing segment}} = 1 + \left(2.7 \cdot \frac{t}{c} + 100 \cdot \left(\frac{t}{c}\right)^4 \cos^2(\Lambda_{0.5})\right) \tag{A.4}$$

To calculate the thickness-to-chord ratio of each segment, the airfoils defined in Table A.3 have been used for the Flying-V. The main wing section airfoils have been retrieved from the work of Palermo [26] on the 4.6% sub-scale

model of the Flying-V. The winglets have been modelled with symmetric NACA0012 airfoils. The airfoils of the A350-900 wing sections have been obtained from Oosterom [39], using a NACA0020 airfoil at the wing root, a NACA2415 airfoil at the end of the yehudi, a Withcomb supercritical airfoil with a 9% t/c at the wing tip and a NACA0012 for the winglet. Both the horizontal tailplane and the vertical tailplane are also modelled with a NACA0012 airfoil. The corresponding Bernstein coefficients can be found in Table A.4. The wetted area of each wing segment is calculated using Equation A.5 [60], where $S_{\exp}$ is the exposed wing area, τ is the average thickness-to-chord ratio of the root and the tip sections and λ is the taper ratio.

$$S_{\text{wet, wing segment}} = 2 \cdot S_{\exp} \cdot \left(1 + 0.25 \cdot (t/c)_r \cdot \frac{1 + \tau \cdot \lambda}{1 + \lambda}\right) \tag{A.5}$$

The interference factor of the wing is 1.0 for the Flying V, as it does not have a fuselage to interfere with. For the wing of the Airbus A350, an interference factor of 1.2 is chosen, which is mid-range (1.0-1.4) for a low wing. For the empennage a factor 1.05 is advised by Raymer.

The main wing sections and segments of the Flying-V and the Airbus A350 are shown in Figure A.1. Information regarding the airfoils at each section and wing segment parameters can be found in section A.7.
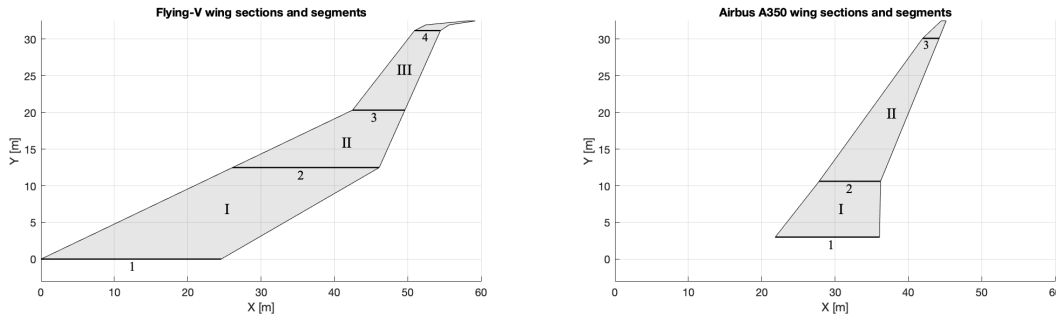
Figure A.1: Main wing sections and segments definitions for the Flying-V and Airbus A350.

A.2. FUSELAGE

Torenbeek [60] presented Equation A.6 to estimate the wetted area of a fuselage with a cylindrical middle section:

$$S_{\text{wet, fus}} = \pi \cdot D_{\text{fus}} \cdot l_{\text{fus}} \cdot \left(1 - \frac{2}{\lambda_{\text{fus}}}\right)^{2/3} \left(1 + \frac{1}{\lambda_{\text{fus}}^2}\right) \tag{A.6}$$

where D_{fus} is the fuselage diameter, l_{fus} is the fuselage length, and $\lambda_{\text{fus}} = l_{\text{fus}}/D_{\text{fus}}$ is the fuselage finesse ratio. Using the fuselage finesse ratio, the form factor of the fuselage can be estimated using Equation A.7. The dimensions of the A350-900 fuselage have been retrieved from Airbus [40].

$$f_{\text{fus}} = 1 + \frac{60}{\lambda_{\text{fus}}^3} + \frac{\lambda_{\text{fus}}}{400} \tag{A.7}$$

The interference factor Q of the fuselage is taken to be 1.0 following Raymer, because interference factors are usually taken with respect to the fuselage and it does not interfere with itself.

A.3. NACELLES AND PYLONS

The wetted area of the nacelles is calculated using the geometry definitions presented in Figure A.2. The dimensions of the nacelles and pylons have been obtained from Airbus [40] and are presented in Figure A.3. The form factor of nacelles and pylons is estimated using Equation A.8. The wetted area of the nacelles can be divided into three parts: fan cowling, gas generator and plug, which are calculated using Equation A.10, Equation A.11 and Equation A.12, respectively. The wetted area of the pylons is approximated roughly as the

shape is unconventional. For the interference factor of the nacelles a factor 1.3 and 1.5 is chosen for the Flying-V and Airbus A350, respectively. These values correspond with an installation within approximately 1 diameter from the wing and an installation in the direct proximity of the wing.

$$f_{\text{nac,pyl}} = 1 + \frac{0.35}{l/D} \tag{A.8}$$

$$S_{\text{wet, nacelle}} = S_{\text{wet, fan cowl.}} + S_{\text{wet, gas gen.}} + S_{\text{wet, plug}} \tag{A.9}$$

$$S_{\text{wet, fan cowl.}} = l_n \cdot D_n \cdot \left[2 + 0.35 \frac{l_1}{l_n} + 0.8 \cdot \frac{l_1 \cdot D_{hl}}{l_n \cdot D_n} + 1.15 \cdot \left(1 - \frac{l_1}{l_n}\right) \cdot \frac{D_{ef}}{D_n} \right] \tag{A.10}$$

$$S_{\text{wet, gas gen.}} = \pi \cdot l_g \cdot D_g \cdot \left[1 - \frac{1}{3} \cdot \left(1 - \frac{D_{eg}}{D_g}\right) \cdot \left(1 - 0.18 \cdot \left(\frac{D_g}{l_g}\right)^{\frac{5}{3}}\right) \right] \tag{A.11}$$

$$S_{\text{wet, plug}} = 0.7 \cdot \pi \cdot l_p \cdot D_p \tag{A.12}$$
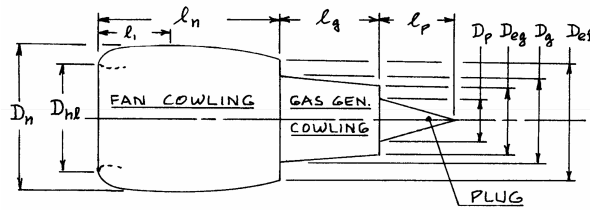
Figure A.2: Geometry of the nacelle as used to calculate the wetted area [60].
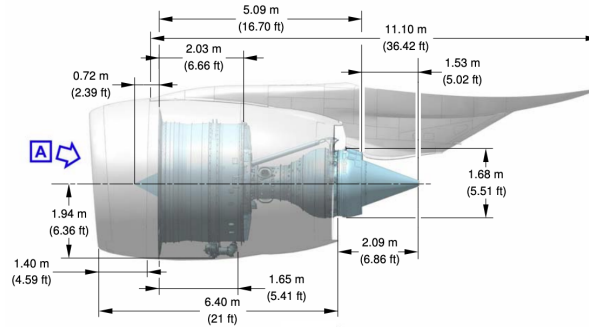
Figure A.3: The nacelle and pylon geometry and dimensions of the Airbus A350 [40].

A.4. Landing gear

The Flying-V landing gear is based on the study performed by Bourget [34]. The configuration used in this study is the 5.5 configuration, where the nose gear strut length is 3.81m and the main gear strut length is 5.41m (assuming a 2/3 compressed shock absorber [59]). The Airbus A350-900 landing gear dimensions have been provided by Airbus [40], where the nose gear strut length is measured to be 2.73m and the main gear strut length is 3.27m. For the Flying-V it is assumed that the wheel configurations of the nose and landing gear are the same as for the A350-900 and that the only drag difference come from the different strut lengths on both aircraft. To calculate the total zero-lift drag, the landing gear is divided into different components. For each component, the frontal area can be calculated and a multiplication factor based on the type of component is taken from Raymer [59], listed in Table A.5. To account for interference, the sum of components should be multiplied by 1.2, while open doors while the landing gear is deployed accounting for another factor 1.07, as advised by Raymer. The dimensions of the landing gear used in this study are shown in Figure A.5.
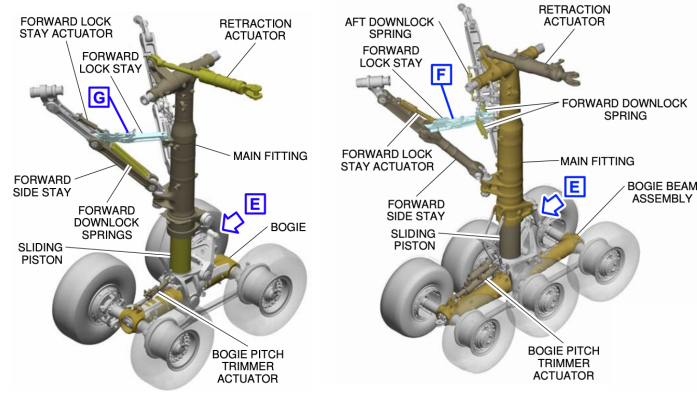
Figure A.4: Airbus A350-900 (left) and A350-1000 (right) main landing gear geometry. Figures by Airbus [40].
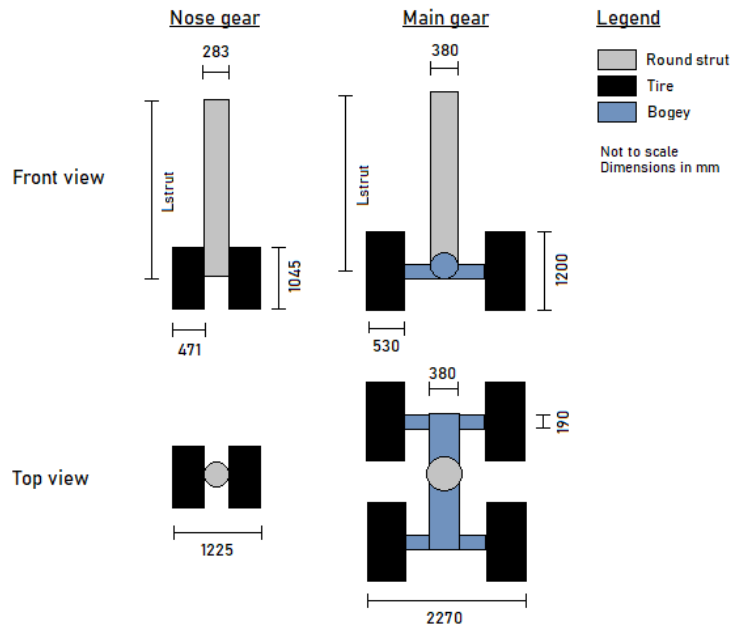
Figure A.5: Landing gear dimensions used in this study to calculate the parasite drag of the nose and main landing gear.

A.5. FLAPS

The Flying-V does not have a flap system, but the Airbus A350 does. Separated flow above the flap causes additional parasitic drag, which is estimated using Equation A.13 [59].

$$C_{D_{0\,\text{flap}}} = F_{\text{flap}} \frac{c_f}{c} \frac{S_{\text{flapped}}}{S_{\text{ref}}} (\delta_{\text{flap}} - 10) \tag{A.13}$$

where δ_{flap} is in degrees, c_f is the flap chord, c is the local chord and the flapped area S_{flapped} is illustrated in Figure A.6. For F_{flap} a value of 0.0074 is used, which corresponds to a slotted flap. The flap deflection depends on the configuration of the aircraft. The total flapped area for the inboard and outboard flap of the A350-1000 is taken to be 164 and 124 m^2, respectively. The flap chord as a ratio of the local chord length is taken to be 0.141 for the inboard flap and 0.158 for the outboard flap.
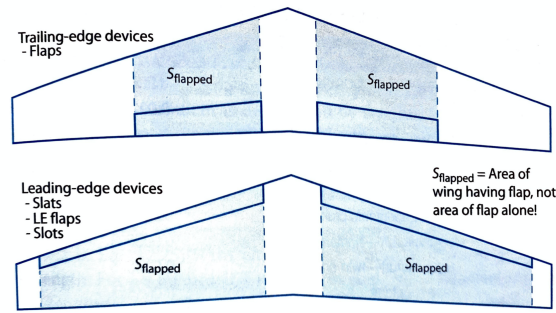
Figure A.6: Flapped wing area definition.

A.6. LEAKAGE & PROTUBERANCES

According to Raymer, leakage and protuberance can account for 2-5% of the total parasite drag for transport aircraft. For the Flying-V, an estimation of 4.4 counts has been made by K. Bender, which value is used in this research. For simplicity it is assumed that the total drag due to leakage and protuberances is equal for the Flying-V and the Airbus A350. Hence, taking the different reference areas into account, the leakage and protuberances parasite drag of the A350 is estimated to be 8 counts.

A.7. TABLES

Table A.1: Flying-V parameters used to calculate zero-lift drag. Note that the wetted area is given for both wing halves in case a mirrored counterpart exists.

Category	Part	S_{wet} [m²]	f [-]	Q [-]	L_{Re} [m]	C_{D_0} [cts]
Wing segments	MW-I	1134	1.452	1.0	21.96	
	MW-II	430	1.350	1.0	14.38	
	MW-III	234	1.265	1.0	5.29	
	WL	50	1.336	1.0	2.37	
Nacelles		163	1.162	1.3	8.49	
Pylons		97	1.073	1.3	10.80	
Landing Gear	Main					42.2
	Nose					8.3
Leakage						4.4

Table A.2: Reference aircraft parameters used to calculate zero-lift drag. Note that the wetted area is given for both wing halves in case a mirrored counterpart exists.

Category	Part	S_{wet} [m²]	f [-]	Q [-]	L_{Re} [m]	C_{D_0} [cts]
Wing segments	MW-I	357	1.556	1.25	11.55	
	MW-II	428	1.342	1.25	5.90	
	WL	19	1.290	1.25	1.60	
	HT	178	1.340	1.05	4.82	
	VT	106	1.338	1.05	5.89	
Fuselage		1123	1.073	1.0	66.61	
Nacelles		163	1.162	1.5	8.49	
Pylons		70	1.048	1.5	11.10	
Landing Gear	Main					67.8
	Nose					12.2
Leakage						8.0

Table A.3: Flying-V wing section Bernstein coefficients for main wing (MW) and winglet (WL) sections.

Section	Upper						Lower					
	β_1	β_2	β_3	β_4	β_5	β_6	β_1	β_2	β_3	β_4	β_5	β_6
MW-1	0.198	0.134	0.405	-0.053	0.647	-0.467	-0.155	-0.228	-0.018	-0.419	-0.021	-0.999
MW-2	0.235	0.109	0.252	0.166	0.259	0.210	-0.232	-0.132	-0.288	-0.240	-0.223	-0.158
MW-3	0.085	0.075	0.197	0.102	0.219	0.253	-0.131	-0.091	-0.030	-0.300	0.060	0.223
MW-4	0.133	0.070	0.202	0.070	0.153	0.265	-0.096	-0.094	-0.009	-0.413	0.084	0.144
WL-1	0.170	0.160	0.144	0.166	0.111	0.179	-0.170	-0.160	-0.144	-0.166	-0.111	-0.179
WL-2	0.170	0.160	0.144	0.166	0.111	0.179	-0.170	-0.160	-0.144	-0.166	-0.111	-0.179

Table A.4: Reference aircraft wing section Bernstein coefficients for main wing (MW), winglet (WL), horizontal tail (HT) and vertical tail (VT) sections.

Section	Upper						Lower					
	β_1	β_2	β_3	β_4	β_5	β_6	β_1	β_2	β_3	β_4	β_5	β_6
MW-1	0.284	0.267	0.240	0.277	0.185	0.299	-0.284	-0.267	-0.240	-0.277	-0.185	-0.299
MW-2	0.243	0.233	0.265	0.233	0.221	0.287	-0.187	-0.162	-0.101	-0.177	-0.059	-0.161
MW-3	0.127	0.121	0.109	0.118	0.093	0.128	-0.127	-0.121	-0.109	-0.118	-0.093	-0.128
WL-1	0.170	0.160	0.144	0.166	0.111	0.179	-0.170	-0.160	-0.144	-0.166	-0.111	-0.179
WL-2	0.170	0.160	0.144	0.166	0.111	0.179	-0.170	-0.160	-0.144	-0.166	-0.111	-0.179
HT-1	0.170	0.160	0.144	0.166	0.111	0.179	-0.170	-0.160	-0.144	-0.166	-0.111	-0.179
HT-2	0.170	0.160	0.144	0.166	0.111	0.179	-0.170	-0.160	-0.144	-0.166	-0.111	-0.179
VT-1	0.170	0.160	0.144	0.166	0.111	0.179	-0.170	-0.160	-0.144	-0.166	-0.111	-0.179
VT-2	0.170	0.160	0.144	0.166	0.111	0.179	-0.170	-0.160	-0.144	-0.166	-0.111	-0.179

Table A.5: Drag per dynamic pressure per frontal area for different landing gear component types [59].

Component	$\frac{D/q}{A_{\text{frontal}}}$
Regular wheel and tire	0.25
Second wheel and tire in tandem	0.15
Round strut	0.30
Fork, bogey, irregular fitting	1.2

Table A.6: Landing gear drag comparison.

Landing gear	Variable		Flying-V-1000	Airbus A350-1000
Nose gear	Strut length	(m)	3.81	2.73
	Strut C_{D_0}	(cts)	4.7	6.4
	Wheel C_{D_0}	(cts)	3.6	5.8
Main gear	Strut length	(m)	5.41	3.27
	Strut C_{D_0}	(cts)	17.9	20.7
	Wheel C_{D_0}	(cts)	24.3	47.1
Total	C_{D_0}	(cts)	50.5	80.0
	$C_{D_0}S$	(m^2)	4.46	3.69

B

WAVE DRAG ESTIMATION: DELTA METHOD

This appendix elaborates on how the wave drag coefficient is determined using the Delta method [62]. The first step is to determine the design lift coefficient using Figure B.1. The aspect ratio and quarter-chord sweep angles can be found in Table 2.3. The value h/c is defined as 100 times the wing camber at 70% semispan. For the Flying-V-1000 this value has been taken to be 2.0, while 1.0 has been used for the Airbus A350-1000. Using the design lift coefficient and the average thickness-to-chord ratio of the wing, the two-dimensional drag divergence number M_{dd2d} is found using Figure B.2. Using Figure B.3 the two-dimensional value is corrected using Equation 3.12 to find the values presented in Table 5.2.
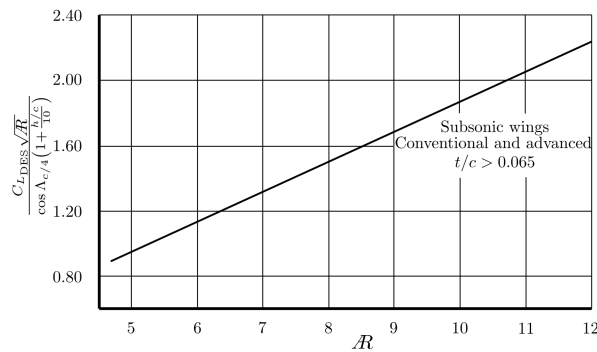
Figure B.1: Design lift coefficient vs. Aspect ratio.
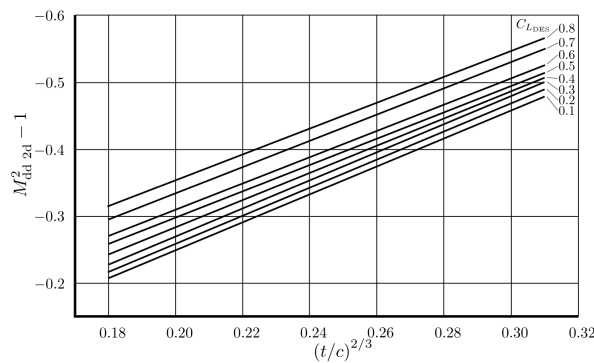
Figure B.2: Two-dimensional drag divergence Mach number vs. design lift coefficient and wing thickness-to-chord ratio.

(a) Sweep angle correction

(b) Aspect ratio correction
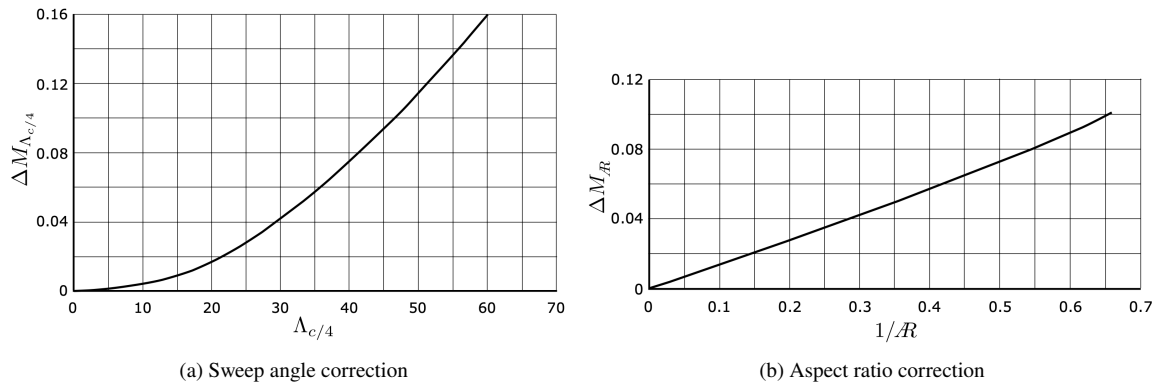
Figure B.3: Drag divergence Mach number corrections for quarter-chord sweep angle and aspect ratio.

Based on charts in the report that presents the Delta method [62] and the thickness-to-chord ratio of the wings of both aircraft, Figure B.4 has been created. These charts have been implemented in the flight mechanics model to determine the wing wave drag coefficient based on the flight Mach number and the divergence drag Mach number.
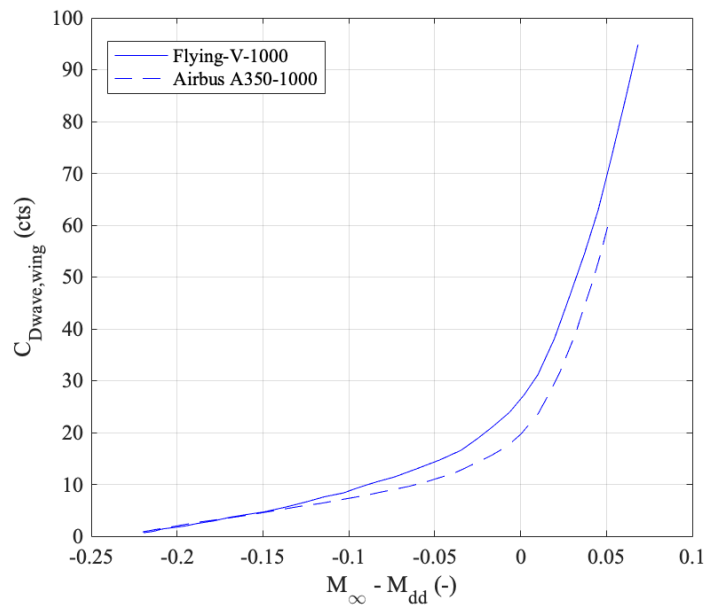
Figure B.4: Wing wave drag coefficient as a function of flight Mach number and drag divergence Mach number.
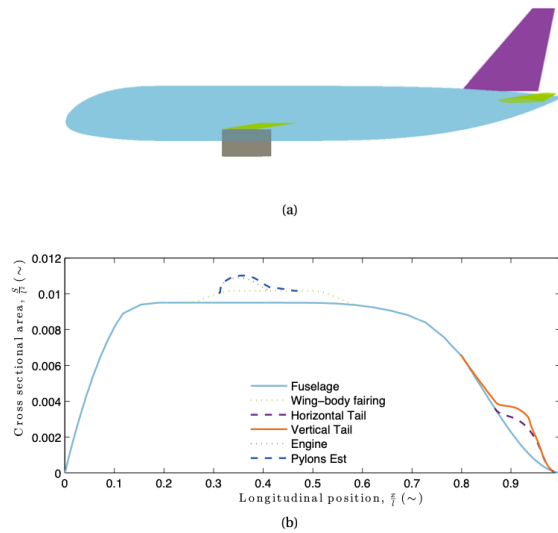
Figure B.5: Cross-sectional area distribution of typical tube-and-wing aircraft [61].

For the Airbus A350-1000 a fuselage wave drag coefficient has been implemented. Based on Figure B.5 and the dimensions of the Airbus A350-1000 the maximum cross-sectional area of the Airbus A350-1000 was found to be $S_{\max} = 60$ m^2. Due to the highly tapered aft fuselage the ratio $S_b/S_{\max}$ was assumed to be very small. Hence, for $(1 + S_b/S_{\max})$ the value 1.0 was adopted in Figure B.6.
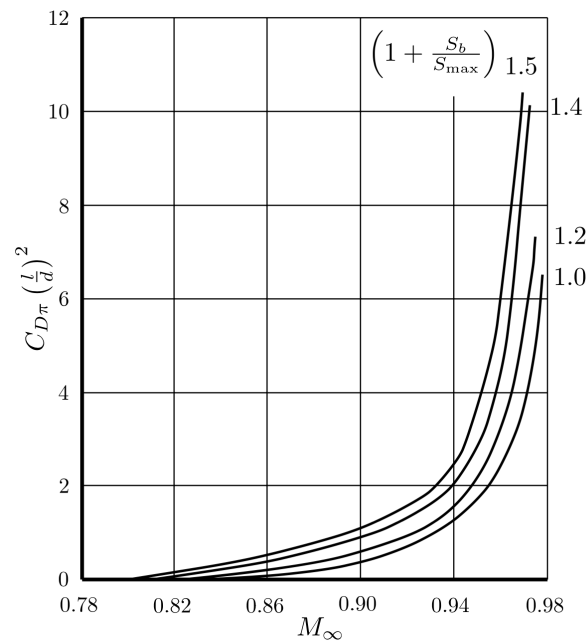
Figure B.6: Fuselage wave drag coefficient vs free-stream Mach number.

The coefficient found from Figure B.6 must be normalised using the wing reference area S using Equation B.1 to find the fuselage wave drag coefficient.

$$C_{D_{w_{\text{fus}}}} = C_{D_\pi} \left(\frac{S_{max}}{S} \right)$$

(B.1)

C

AIRBUS A350-1000 INERTIA DERIVATION

Table C.1 shows a comparison between the maximum takeoff mass and minimum operating empty mass of the Airbus A350-900 as modelled by Claeys [36] and specified by Airbus [40]. The multiplication factor required to bridge the gap between these values is used to linearly scale the moments of inertia matrices at MTOM and empty weight under the assumption of an equal mass distribution to find the values used in the present research for the A350-900, shown in Table C.2.

To find the moments of inertia for the Airbus A350-1000, the reference aircraft for the present research, the A350-900 inertia matrix is modified. As the main difference between the -900 and -1000 version are the additional fuselage plugs, as shown by Figure 3.5. Therefore, the additional moment of inertia around the x-axis is estimated by adding the inertia of a cylinder with mass ΔM_{fus}, the additional fuselage mass, and a radius R_{fus}, the fuselage radius. This amounts to $\Delta I_{xx} = \frac{1}{2}\Delta M_{\text{fus}}R_{\text{fus}}^2$. From Airbus specifications, it is estimated that $\Delta M_{\text{fus}} = 31,000$kg and $R_{\text{fus}} = 3.05$m. The moments of inertia around the y- and z-axes have been shown by Cappuyns [37] to scale roughly quadratically with aircraft length scales. Figure C.1 shows that I_{yy} can be estimated by scaling with the length of the aircraft squared. The same method can be used to scale I_{zz} with the sum of the squares of the length and height of the aircraft. From Airbus specifications the height and aircraft length difference between the A350 -900 and -1000 can be retrieved (Figure C.2 and Figure C.3). Using these dimensions the scaling factors for I_{yy} and I_{zz} are found be 1.221 and 1.209, respectively. Multiplying the A350-900 moments of inertia by these scaling factors yield the A350-1000 values used in the present research, presented in Table C.2.

Table C.1: Maximum takeoff mass (MTOM) and Minimum operating empty mass (MOEM) comparison of Airbus A350-900 specifications [40] and previous research by Claeys [36].

Item	Claeys model	Airbus specs	Factor difference
MTOM (ton)	260.4	280.0	0.93
MOEM (ton)	107.5	117.0	0.92

Table C.2: Moments of inertia around the aircraft body principal axes at maximum takeoff weight and empty weight for the Airbus A350-900 and -1000. A comparison is made between the values found by Claeys and values used in the present research.

Inertia	A350-900 Claeys		A350-900 present		A350-1000 present	
	MTOM	Empty	MTOM	Empty	MTOM	Empty
I_{xx} ($\cdot 10^7$ kg m^2)	2.945	0.853	3.167	0.928	3.181	0.942
I_{yy} ($\cdot 10^7$ kg m^2)	3.878	2.123	4.170	2.310	5.089	2.820
I_{zz} ($\cdot 10^7$ kg m^2)	6.648	2.846	7.149	3.097	8.644	3.745
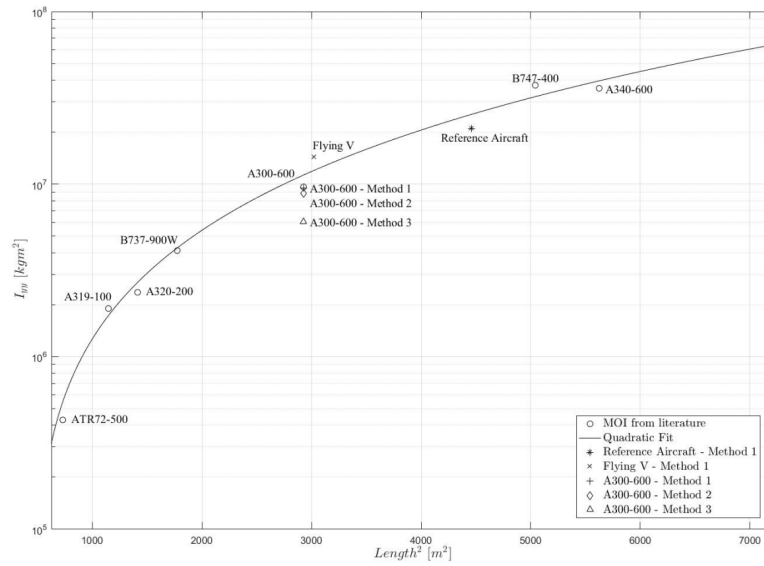
(a) I_{yy} vs. aircraft length squared
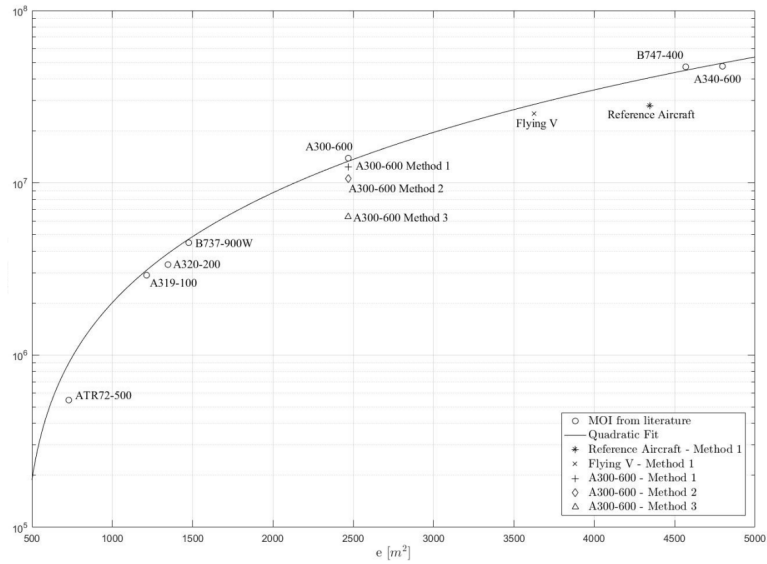
(b) I_{zz} vs. sum of squares of aircraft length and height

Figure C.1: Moments of inertia around the body y- and z-axes of various aircraft.

C.1. Airbus A350-900 and -1000 dimensions
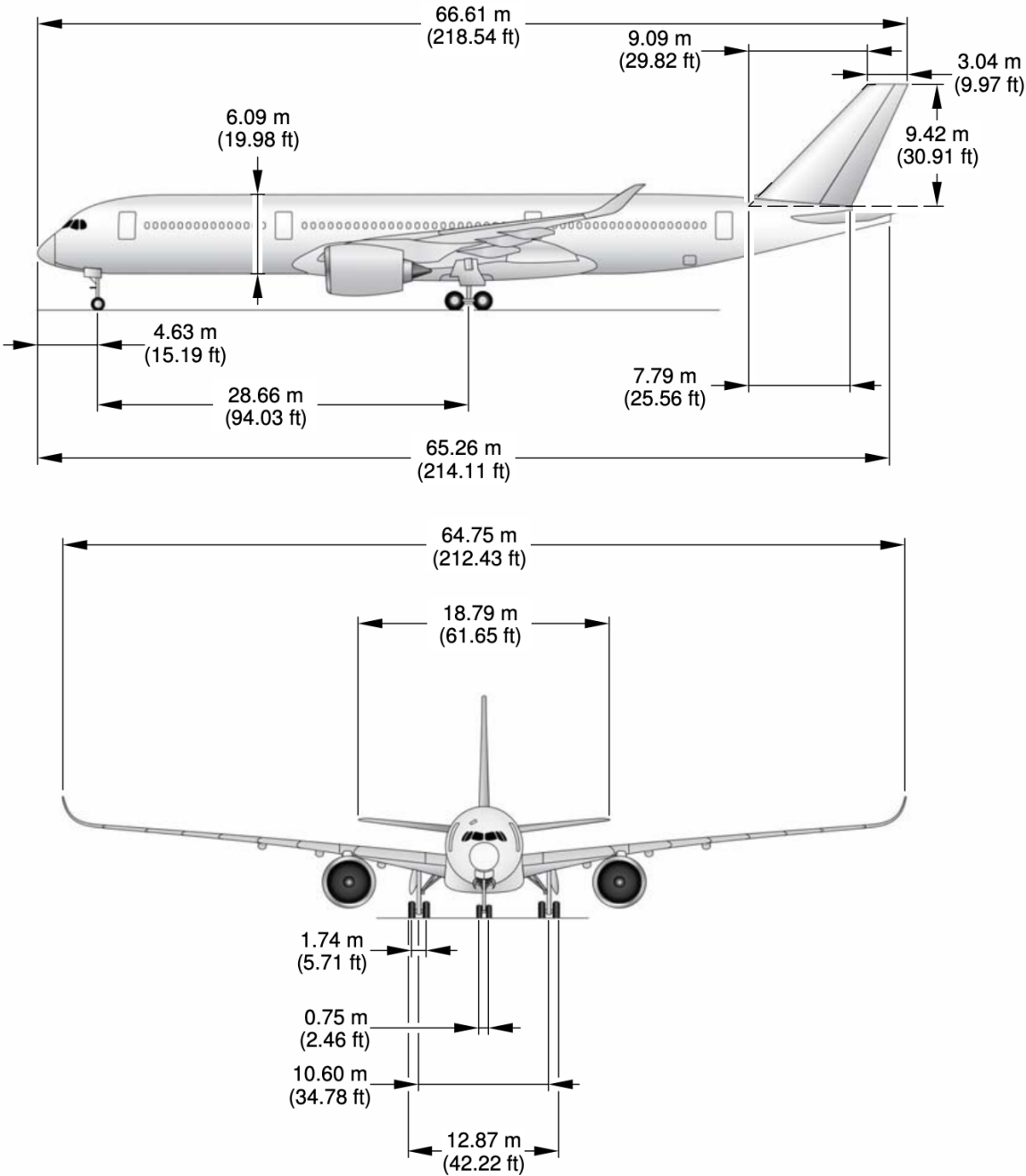
Figure C.2: Airbus A350-900 dimensions. Figure from Airbus [40].
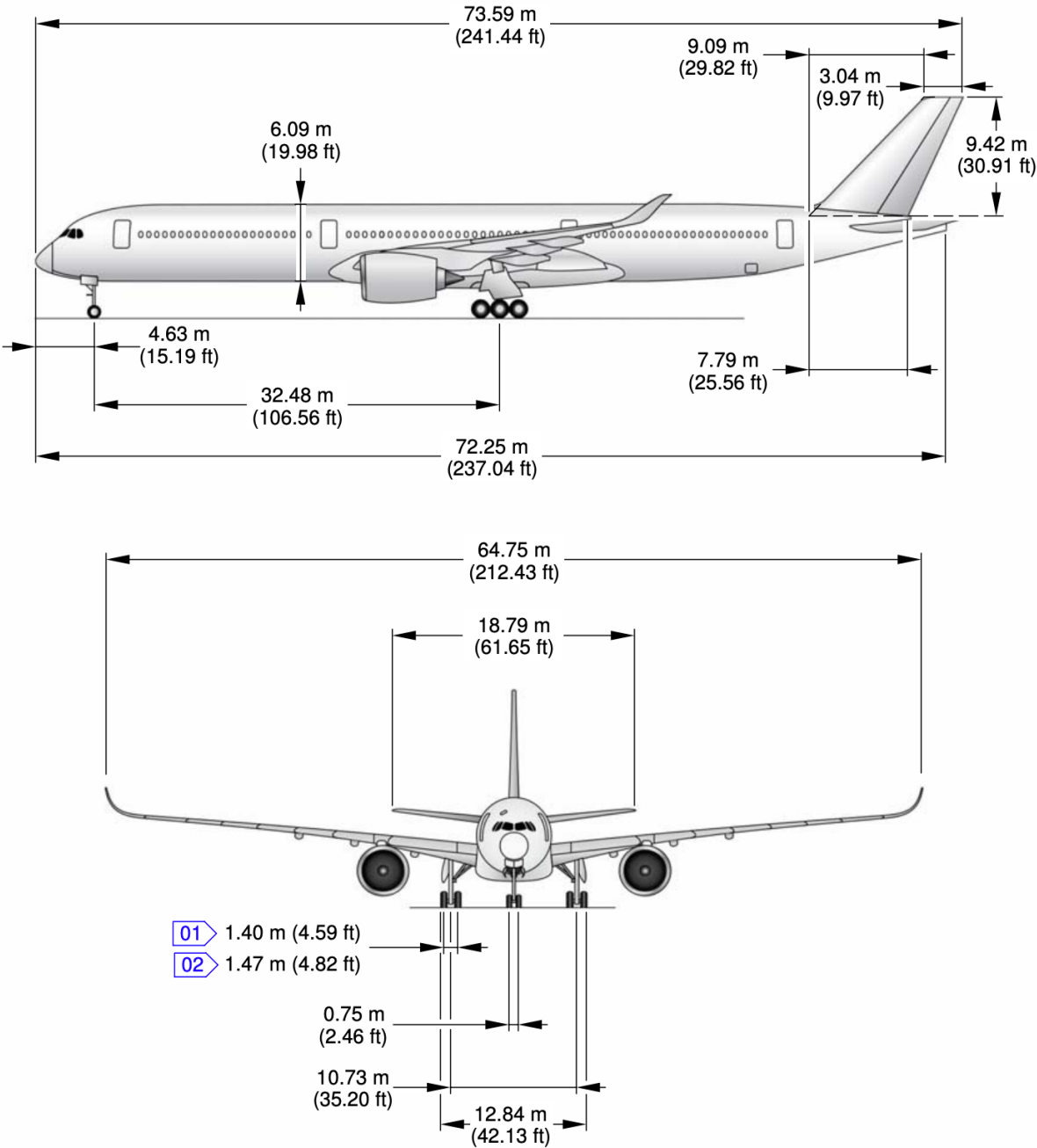
Figure C.3: Airbus A350-1000 dimensions. Figure from Airbus [40].

D

BARTEL-YOUNG THRUST LAPSE MODEL

D.1. THRUST SPECIFIC FUEL CONSUMPTION

The thrust specific fuel consumption is estimated using Equation 3.20. The value of exponent n is determined from Figure D.1, where the value on the horizontal axis is the cruise thrust of a single engine divided by the inlet area of the fan. For this research this it was estimated that $n \approx 0.42$.
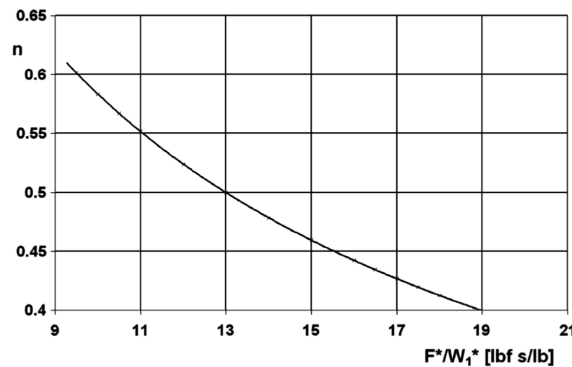
Figure D.1: Exponent n used to calculate TSFC. [63].

D.2. THRUST CALCULATIONS

The gas generator function value used in subsection 3.4.1 is determined from Figure D.2.
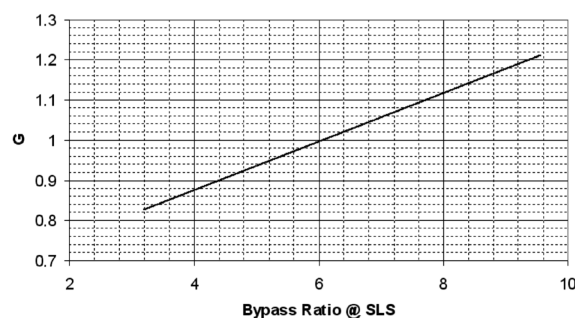
Figure D.2: Gas generator function at sea level G_0 as a function of the BPR at sea level [63].

In order to determine the maximum available thrust at a given altitude and Mach number, the fraction T_{CR}/T_{max} should be determined. This is done by estimating:

- $T_{max}/T_{max, climb}$

68

- $T_{\mathrm{max,climb}}/T_{\mathrm{CR}}$

Based on Figure D.3 it was estimated that $T_{\mathrm{CR}}/T_{\mathrm{max}} \approx 0.85$, which is in good agreement with the specifications of the maximum continuous and maximum available thrust fraction at sea level for the A350-900 and A350-1000 engines, the Trent XWB-84 and -97.
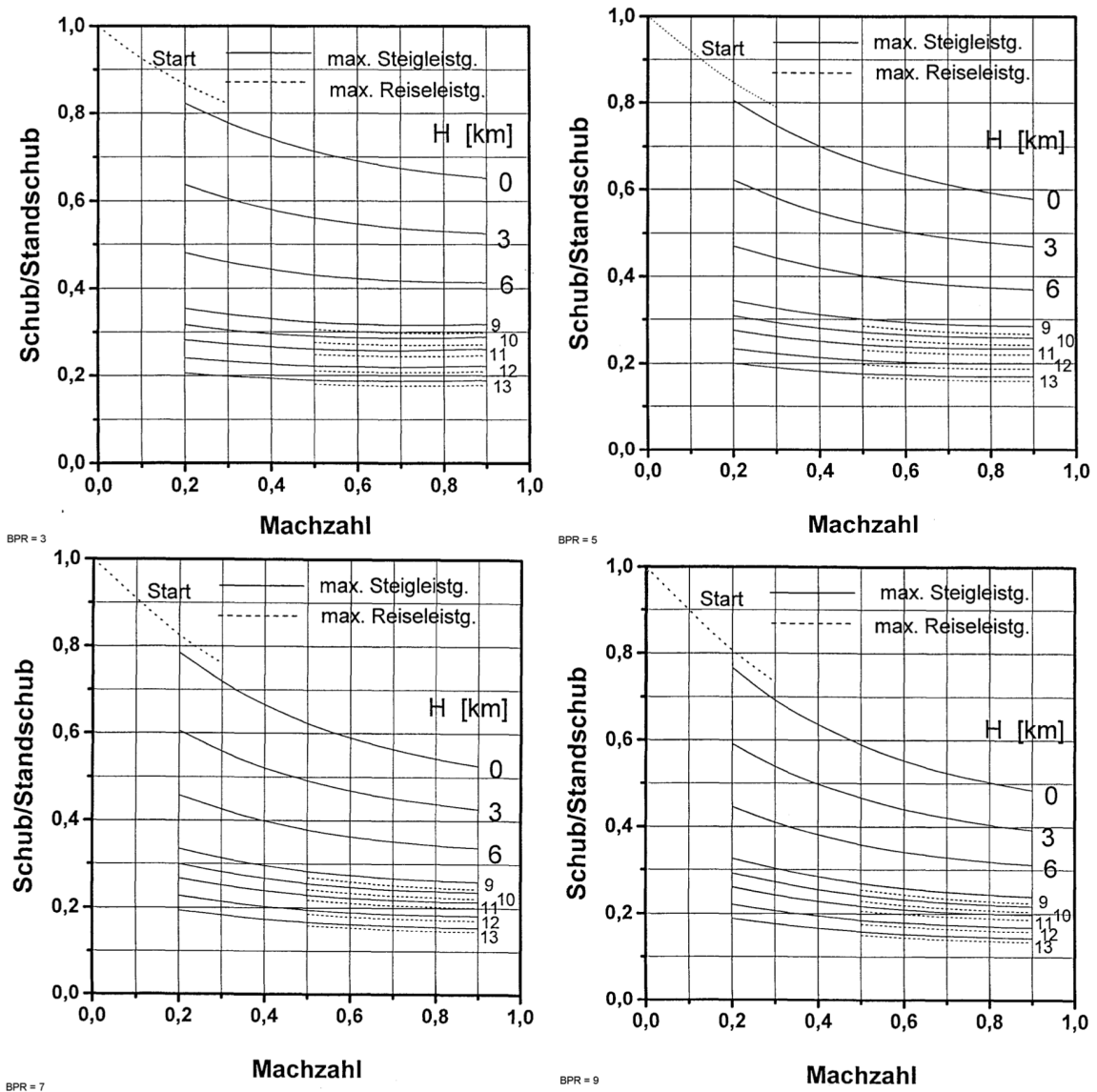
Figure D.3: Engine performance curves for different bypass ratios (indicated in bottom-left corner of each figure) at varying flight Mach numbers and altitudes. The solid curves show the maximum climb thrust, while the dashed curves show the maximum continuous thrust.

E

ODILILA VERIFICATION

Odilila is a Vortex Lattice Method developed and verified by Airbus. This verification has previously been shown by Claeys [36] and Cappuyns [37] and is repeated below. As Odilila is owned by Airbus, the values of the figure axes have been omitted.

Lift curve slope predictions for different aspect ratios and sweep angles made using Odilila have been shown to match well with theoretical curves presented by Raymer [59].

$$C_{L_\alpha} = \frac{2\pi AR}{2 + \sqrt{4 + AR^2(1 + \tan^2\Lambda)}} \tag{E.1}$$

In Equation E.1 C_{L_α} is the derivative of the lift curve slope with respect to the angle of attack α, $AR = b^2/S$ is the wing aspect ratio (where S is the wing reference area and b is the wing span), and Λ is the wing sweep angle.

Figure E.1 shows a comparison between lift curve slopes calculated by Odilila and the theoretical lift curve slopes calculated using Equation E.1. The figure is provided by K.Bender from Airbus. This comparison is made for a straight untapered wing for varying aspect ratio and sweep angle. It can be seen that similar lift curves are obtained, although Odilila predicts slightly more lift for increasing aspect ratio and decreasing sweep angle. In Figure E.2 Odilila lift curve predictions are compared to wind tunnel data [73, 74], where the red line indicates the Odilila predictions. For all aspect ratios the wind tunnel data matches the Odilila predictions well, while the lift curve slope variation with sweep angle matches satisfactorily.

(a) Influence of aspect ratio (b) Influence of sweep angle
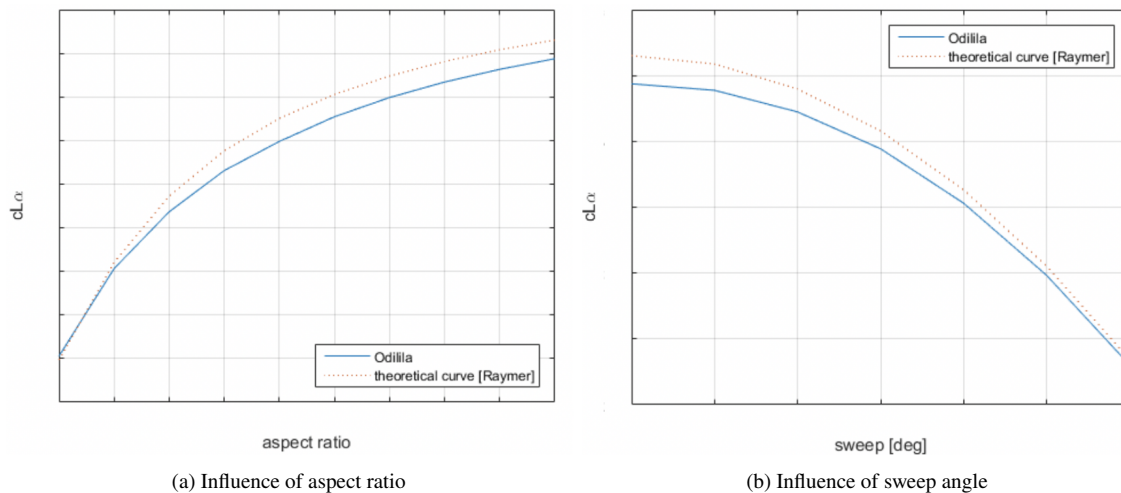
Figure E.1: Comparison of Odilila and theoretical lift curve slopes of a straight untapered wing for varying aspect ratio and sweep angle.

The effect of spanwise discretisation on the predicted induced drag and lift curve slope has been investigated by Claeys [36] using a wing with an aspect ratio of 10. It was found that the predicted induced drag is close to the
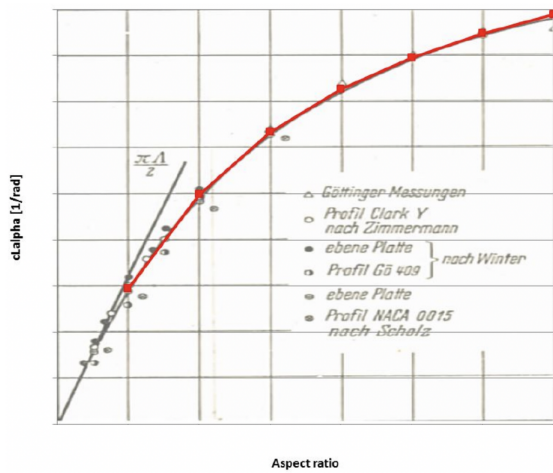
(a) Influence of aspect ratio
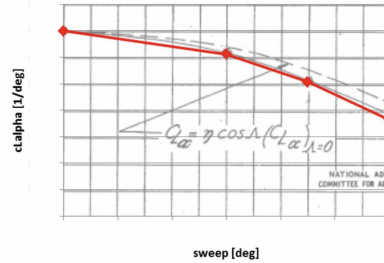
(b) Influence of sweep angle

Figure E.2: Comparison of Odilila and wind tunnel data of lift curve slopes for varying aspect ratio and sweep angle [73, 74].

theoretical induced drag of an elliptical lift distribution, as shown in Figure E.3. For a low number of panels, the predicted induced drag from Odilila is slightly smaller than the theoretical value and vice versa for a large number of panels. However, for the entire range of panels the induced drag stays within 1% of the theoretical value. The influence of chordwise and spanwise discretisation on the predicted lift curve slope has also been investigated and is shown in Figure E.4. Chordwise discretisation has no notable effect on the predicted lift curve slope. Larger number of panels in the spanwise direction cause the predicted lift curve slope to decrease, although the effect of discretisation remains limited.

Figure E.3: Influence of spanwise discretisation on Odilila induced drag prediction.
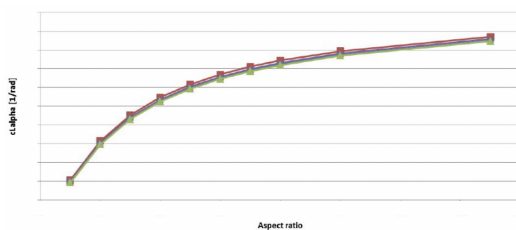
(a) Influence of chordwise discretisation
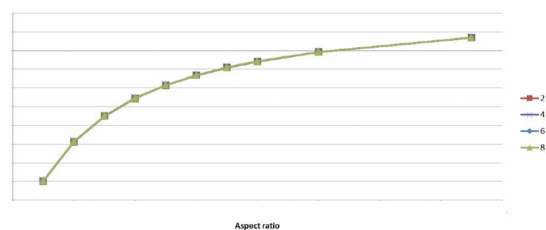
(b) Influence of spanwise descretisation

Figure E.4: Influence of chordwise and spanwise discretisation on the predicted lift curve slope by Odilila.